uOttawa

L'Université canadienne
Canada's university

FACULTÉ DES ÉTUDES SUPÉRIEURES ET POSTOCTORALES

uOttawa

L'Université canadienne
Canada's university

FACULTY OF GRADUATE AND POSDOCTORAL STUDIES

Mohammad Ali Akbari
AUTEUR DE LA THÈSE / AUTHOR OF THESIS

M.A.Sc. (Electrical and Computer Engineering)
GRADE / DEGREE

School of Information Technology and Engineering
FACULTÉ, ÉCOLE, DÉPARTEMENT / FACULTY, SCHOOL, DEPARTMENT

Waveguide Integrated Surface Plasmon Photodetector: Design, Fabrication, and Measurement

TITRE DE LA THÈSE / TITLE OF THESIS

Pierre Berini
DIRECTEUR (DIRECTRICE) DE LA THÈSE / THESIS SUPERVISOR

CO-DIRECTEUR (CO-DIRECTRICE) DE LA THÈSE / THESIS CO-SUPERVISOR

Karin Hinzer

Steven McGarvy

Gary W. Slater
Le Doyen de la Faculté des études supérieures et postdoctorales / Dean of the Faculty of Graduate and Postdoctoral Studies

Waveguide Integrated Surface Plasmon Photodetector: Design, Fabrication, and Measurement

by

Ali Akbari

A Thesis submitted to the Faculty of Graduate Studies and Postdoctoral Studies in partial fulfillment of the requirements for the degree of the requirements for the degree of

Master of Applied Science, Electrical Engineering

January 2010

Ottawa-Carleton Institute for Electrical and Computer Engineering

School of Information Technology and Engineering

University of Ottawa

Ottawa, Ontario, Canada

Your file Votre référence
ISBN: 978-0-494-65527-6
Our file Notre référence
ISBN: 978-0-494-65527-6

Abstract

The thesis investigates the design, fabrication, and experimental demonstration of a photodetector integrated into a thin metal stripe waveguide of finite width, operating at optical infrared wavelengths. The metallic stripe, which is clad by lightly doped silicon at the bottom and air on the top, supports the propagation of bound optical modes having very high loss (~ 1 dB/μm) and submicron field confinement in the axis perpendicular to the stripe width. The metal/silicon interface also has electrically rectifying characteristics, formally described as a Schottky diode. The theoretical model for the electrical performance of the photodiode is combined with a numerical study of the optical modes supported by the waveguide, and used to present theoretical performance predictions. A few designs are fabricated on a silicon wafer and tested experimentally, with successful demonstration of photodetection. The device has promise for applications in short-range optical interconnects, integrated optics, and silicon based photonic circuits.

Acknowledgments

I would like thank my family above all. Their daily presence and support provided me with the basis needed to enjoy the time and privilege of being involved in scientific research.

I would like to thank my supervisor Dr. Pierre Berini for the countless hours of technical discussions, encouragement and support through my master's studies.

This work is dedicated to Karim, Maryam, Mokhtar, Afreena, and dear Khaleh Jan. You mean so much to me and make it all worthwhile.

Contents

Chapter 1

Introduction

1.1 Background

Surface plasmon polaritons (SPPs) are electromagnetic surface modes propagating at the interface between two media having opposite sign of real part of permittivity [1]. At optical frequencies, many noble metals such as Au and Al are known to have negative real permittivity while dieletrics like air and silicon have positive permittivity [2], and thus their interface can support the propagation of bound SPP modes. The SPP arises through the coupling between oscillations in the metal's free conduction electrons and a TM polarized electromagnetic wave [3]. The SPP's dominant field is the electric field perpendicular to the planar interface and propagation direction, with its distribution decaying exponentially in both media. The SPP has many interesting properties, including sub-wavelength field confinement, high bulk and surface sensitivities, and high field intensity at the interface [4]. This unique set of properties and recent advances in nano-fabrication technology has stimulated intense research in SPPs over the past several years. SPPs have found many applications such as waveguiding, integrated optics, and sensing [3].

Studies on the waveguiding applications of SPPs have shown that a thin metal stripe of finite width surrounded by a dielectric cladding can support bound SPP modes which propagate with lower loss and confinement than the single interface SPP, and are thus termed long-range SPP (LRSPP) [5, 6]. A metal stripe with asymmetric cladding (different dielectric

above and below the stripe) can also support bound SPP modes, but which have higher loss and confinement than the aforementioned LRSPP [7, 8].

The interface between a metal and semiconductor is also well known to form a Schottky barrier which has rectifying electrical properties [9]. The interface thus behaves as a Schottky diode, which has been the subject of many investigations for its application as a photodetector [9].

A thin metal stripe clad at the top and bottom by air and silicon respectively, will support bound SPP modes and behave electrically as a Schottky diode at the metal/silicon interface. The focus of this thesis is on the design, fabrication, and testing of metal stripes (Au and Al) clad at the bottom by silicon, and their application as SPP photodetectors. The following sections of this chapter provide a brief review of the bound modes supported by a metal stripe with asymmetric claddings, and of Schottky barrier detectors.

1.2 Bound modes of asymmetrically cladded metal stripes

Figure 1-1 shows a cross-sectional view of the waveguide, consisting of a metal stripe having width w and thickness t, sitting on a substrate of refractive index $n_{substrate}$ and covered by a superstrate of refractive index $n_{superstrate}$. A theoretical analysis of the modes supported by a silver film having $\varepsilon_r = -19 - i0.53$, clad by materials having $n_{substrate} = 2$ and $n_{superstrate} = 1.5$ at a free space optical wavelength of $\lambda_0 = 633$ nm, revealed that many classes of SPP modes are supported by the structure [7]. The vertical component of the electric field is shown in Figure 1-2 for some of the modes supported by the structure. The horizontal symmetry of the waveguide about the vertical axis at the center of the stripe, allows support for modes that are horizontally symmetric or asymmetric. In addition, the modes also show either vertical symmetric-like or asymmetric-like behavior in terms of the sign of the field. Figure 1-3 demonstrate the evolution of the propagation constant of these modes with film thickness. The modes with vertical symmetric-like behavior, denoted in the figure as_b^0 and ss_b^0, are the ones which possess potentially long-ranging behavior, characterized by the low attenuation constant at a certain thickness range. The two letters in this mode annotation represent the symmetry or asymmetry of the fields in the vertical and horizontal axes respectively, while the subscript notes the bound nature of the mode, and the superscript indicates the mode

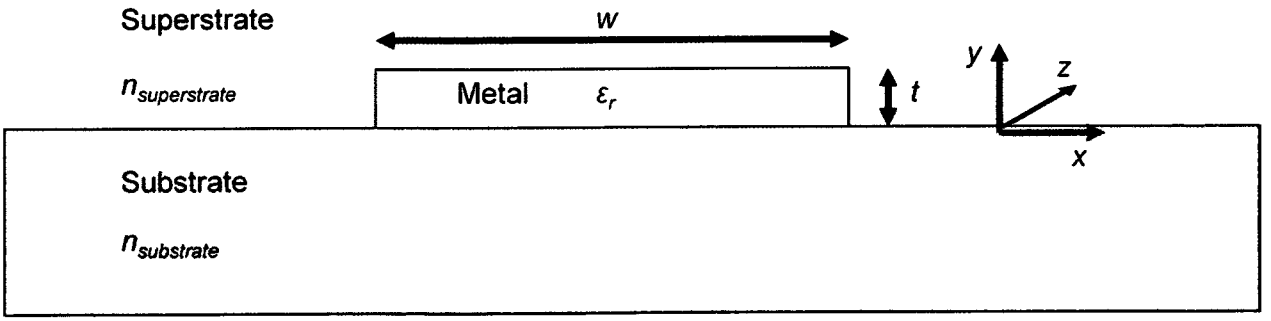

Figure 1-1: Cross sectional view of metal stripe SPP waveguide with asymmetric cladding.

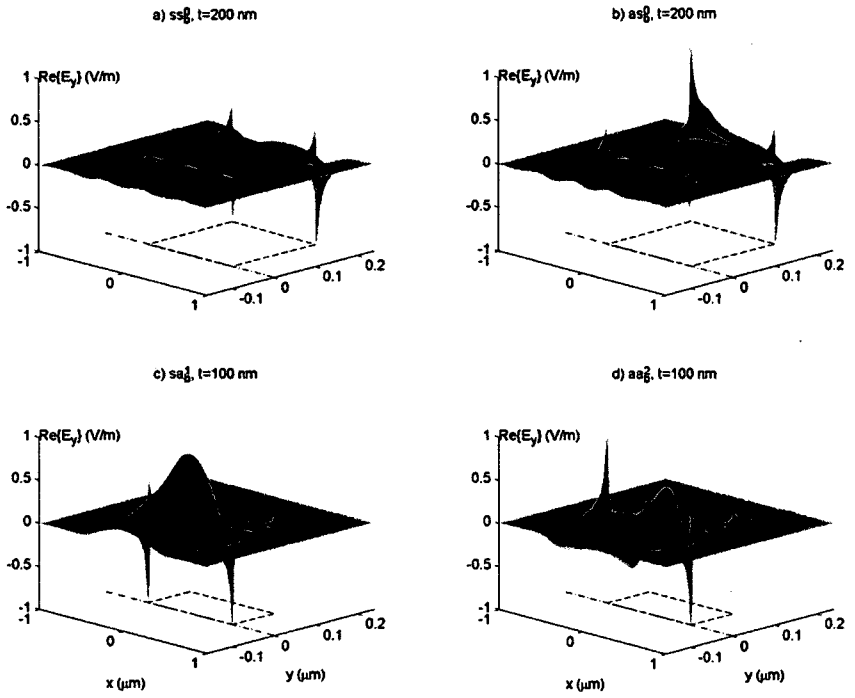

Figure 1-2: Field distribution of the real part of the E_y field component for a 1 μm wide Ag stripe. Field distributions are normalized so that $\max|\mathrm{Re}\{E_y\}| = 1$. Figure shown as published in [7].

order (also number of times the fields change sign in the horizontal direction in the metal). These modes are only supported for stripes having thicknesses greater than a certain cutoff value [7]. The cutoff thickness was found to increase with increasing difference between the refractive indices of the substrate and superstrate. The vertically asymmetric-like modes however are not cutoff at lower thicknesses and their fields extend mainly in the cladding of higher refractive index. For a waveguide with even greater asymmetry, this cutoff thickness is thus expected to be even higher.

The structures of focus in this thesis are Au or Al films having silicon and air as substrate and superstrate respectively. In the infrared wavelength range $\lambda_0 \sim 1550$ nm, the cladding optical parameters are $n_{substrate} = 3.48$ and $n_{superstrate} = 1$. The metal films were restricted to Au

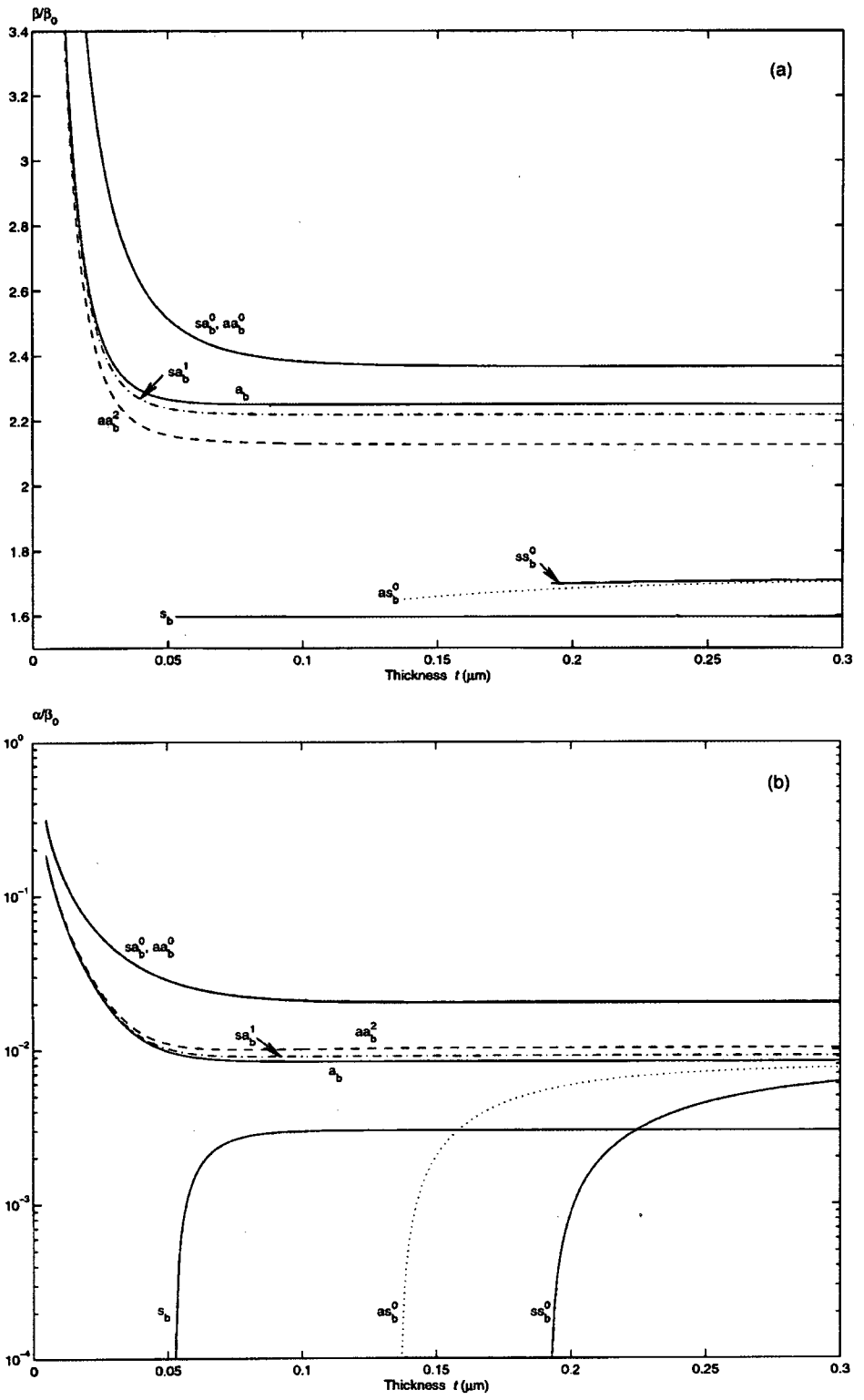

Figure 1-3: Evolution of phase constant with thickness of SPP modes supported by the Ag stripe 0.5 μm wide. α and β are the attenuation and propagation constants, respectively, of the guided SPP mode, while β_0 is the propagation constant of a plane wave travelling in free-space. Figure shown as published in [7].

and Al since their interfacial properties with silicon as well known, and the infrared wavelengths were studied to emphasize potential applications for telecommunication applications. As discussed in subsequent chapters, analysis of this structure using a finite element mode solver [10] has revealed that vertical symmetric-like modes are cutoff for Al and Au stripes having t between 5 and 110 nm, and w between 1.5 and 7 μm. The emphasis of this thesis will therefore be on modes with vertically asymmetric-like behavior, with field distribution similar to the aa_b^2 mode shown in Figure 1-2.

1.3 Conventional Schottky barrier detectors and SPP enhancement

Schottky barrier diodes have been used for many years for detector applications below the bandgap energy of the semiconductor [11]. The typical application, shown in Figure 1-4(a), consists of a semiconductor/metal interface, with radiation incident at a perpendicular angle, and absorption occurring typically in the metal. Photoconduction typically occurs through the internal emission process, described in the energy band diagram in Figure 1-4(b). The charge carriers in the metal gain energy through photon absorption, and acquire enough energy to cross over the Schottky potential barrier, where they can become swept by an applied voltage bias and become collected at another terminal as photocurrent. The Schottky barrier height is typically dependent on the metal's work function and the semiconductor's band gap and electron affinity; although in practice, a dependency on the fabrication process has been observed as well [9]. By treating the electron in the metal as a classical particle with kinetic energy equal to the photon energy, and assuming that it can only cross the barrier by having enough momentum in the direction normal to the interface for it to classically cross the barrier, it can be shown that the

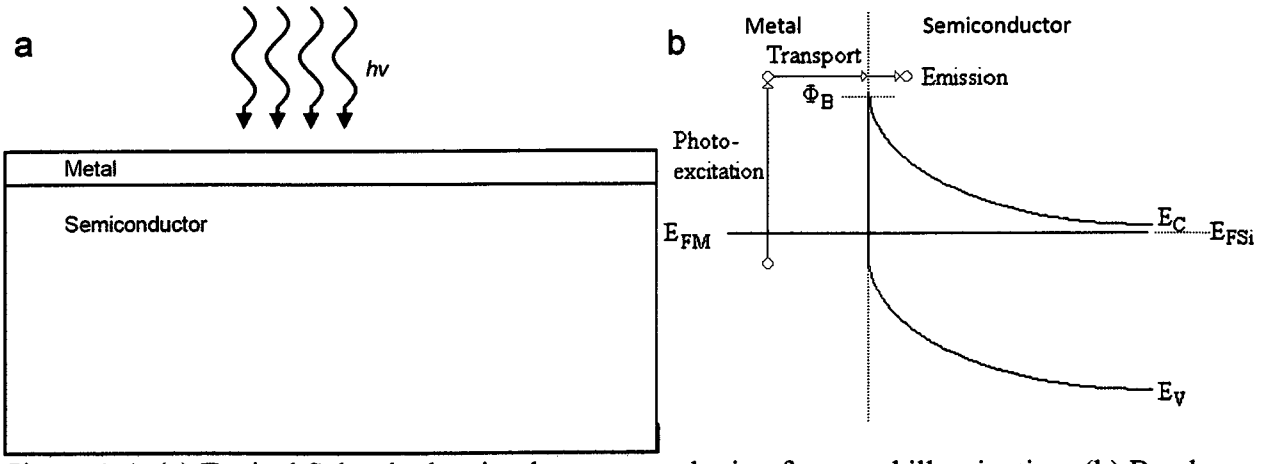

Figure 1-4: (a) Typical Schottky barrier detector employing front-end illumination; (b) Band diagram displaying internal photoemission process.

internal quantum efficiency η_i for a thick metal film is [12, 13]

$$\eta_i = \frac{1}{2}\left(1 - \sqrt{\frac{\Phi_B}{h\nu}}\right)^2$$

The external quantum efficiency η can then be expressed as $\eta = A\eta_i$, where A is the ratio of incident optical power which becomes absorbed in the metal. Since at most frequencies, metals are typically very reflective, the A ratio for the basic detector is not very high and thus the performance of the detector can be poor. Many schemes have been developed to increase this A factor, including enhancement through the use of a resonant cavity [14], as shown in Figure 1-5(a). The cavity allows re-reflection of any radiation initially reflected off the Schottky contact, thus allowing resonant enhancement of the absorbed power for a substrate

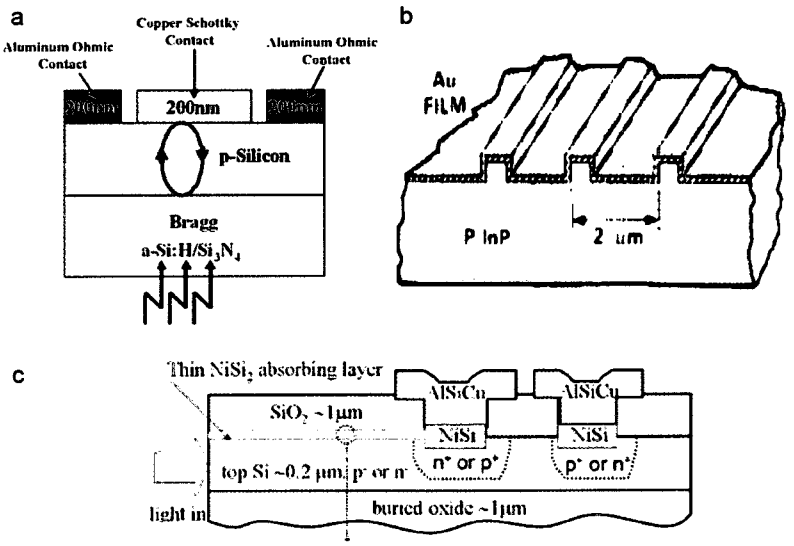

Figure 1-5: Enhancement schemes for Schottky barrier detectors: (a) resonant cavity enhancement (figure shown as published in [14]); (b) coupling to SPP waves through gratings (figure shown as published in [15]); (c) waveguide coupling (figure shown as published in [16]).

of thickness equal to half integer multiples of the wavelength. Another enhancement scheme is to couple incident radiation to SPP waves [15], with all of the coupled radiation becoming absorbed, shown in Figure 1-5(b). In this example, TM-polarized light is incident upon the metal film at an angle, with coupling to the SPP waves occurring through phase matching with the periodic gratings in the metal film. Finally, another popular enhancement method consists of coupling the incident light to a dielectric core waveguide, and introducing a thin Schottky contact that absorbs optical energy [16], with an example shown in Figure 1-5(c). In this setup, absorption can occur over a long waveguide length, however with the absorption rate being low due to the very thin metal, which must remain so in order not to distort the mode supported by the dielectric waveguide.

Scales and Berini have presented a Schottky detector whereby incident radiation is coupled into a symmetrically cladded SPP waveguide [13, 17]. The structure consists of a metal stripe buried in silicon, which is difficult to fabricate, but supports a long-ranging SPP (LRSPP), and thus simultaneously combines the benefits of waveguide coupling and coupling to LRSPP. The device benefits from possible coupling efficiencies approaching unity [18], due to the reduced confinement of the LRSPP mode, which however comes with the drawback of reduced mode power attenuation of 15 dB/mm [13]. This would require a longer waveguide for total absorption of coupled power, which in turn increases the size of the device as well as the dark current.

A similar device, having instead asymmetric cladding, would instead display increased attenuation and field confinement of the SPP mode. This device would benefit from a reduction in both size and dark current, while also suffering from the drawback of a significant reduction in

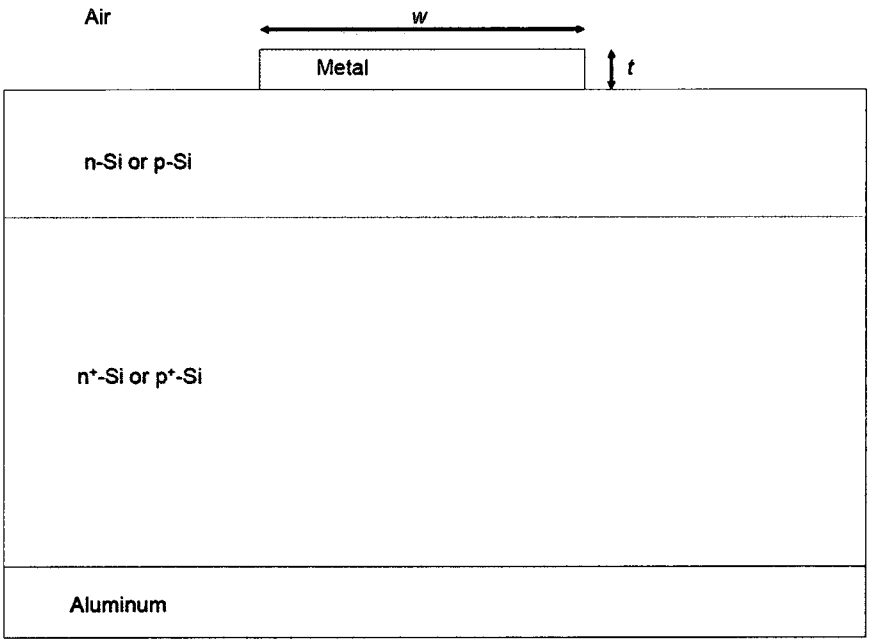

Figure 1-6: Cross sectional view of asymmetrically cladded SPP waveguide photodetector.

coupling efficiency into the SPP mode. A cross sectional view of this device, implemented using Au or Al stripes on Si, is shown in Figure 1-6. The focus of this thesis is towards the design, fabrication, and experimental testing of this proposed device. The photodetector's advantages include low complexity of fabrication as well as small feature size, which consequently reduce the cost of fabricating the detector. This device holds promise for applications in low-cost and short-range optical interconnects, integrated optics, and silicon based photonics.

1.4 Thesis Outline

The thesis is assembled as a collection of articles which are either published or submitted for publication.

Chapter 2 describes the theoretical modeling of the asymmetric cladding SPP photodetector. A theoretical model for the photoelectric properties of the thin metal stripe is described. The Au/Si system is investigated theoretically at a wavelength of 1310 nm and theoretical predictions of its performance as a photodetector are made. The paper "as published" in Applied Physics Letters is incorporated into the thesis. Two additional sections are also included in this chapter: one describing convergence and accuracy of the numerical method used to investigate the device's waveguiding and photodetection; and another providing a more in depth description of the theoretical model describing the photoconduction model for thin metal films.

Chapter 3 describes the theoretical modeling and design of the SPP photodetector for Au and Al stripes on Si, at wavelengths of 1310 and 1550 nm. The multiple supported bound SPP modes are investigated for a larger stripe width and thickness design space, and optimal designs are suggested for each mode, metal, and wavelength combination. The chapter consists of a paper submitted to Journal of Applied Physics.

Chapter 4 describes the fabrication and experimental testing of the SPP photodetectors for Au and Al stripes on n-Si, across a 1280-1620 nm wavelength range. A single width and thickness combination is characterized both electrically and optically. Comparisons are made between the measured performance and theoretical predictions made by the model. The chapter consists of a paper submitted to Optics Express, an additional section providing a

more detailed overview of the fabrication process, and another section providing additional figures related to the measurements of the photodetector.

Appendix A gives a summary of measurements and characterization performed on long-ranging SPP waveguides. Appendix B gives a summary of all the fabricated devices.

Additional references in each section are collected at the end of the respective chapter.

1.5 References

[1] W. L. Barnes, A. Dereux, and T. W. Ebbesen, "Surface Plasmon subwavelength optics," *Nature*, vol. 424, no. 6950, pp. 824-830, 2003.

[2] E. Palik, *Handbook of Optical Constants of Solids*, New York: Academic Press, 1985.

[3] S. A. Maier, *Plasmonics: Fundamentals and Applications*, New York: Springer, 2007.

[4] P. Berini, "Bulk and surface sensitivities of surface plasmon waveguides," *P. New J. Phys.*, vol. 10, pp. 105010, 2008.

[5] P. Berini, "Plasmon-polariton waves guided by thin lossy metal films of finite width: Bound modes of symmetric structures," *Phys. Rev. B*, vol. 61, pp. 10484-10503, 2000.

[6] T. Nikolajsen, K. Leosson, I. Salakhutdinov, S. I. Bozhevolnyi, "Polymer-based surface-plasmon-polariton stripe waveguides at telecommunication wavelengths," *Appl. Phys. Lett.*, vol. 82, pp. 668-670, 2003.

[7] P. Berini, "Plasmon-polariton waves guided by thin lossy metal films of finite width: Bound modes of asymmetric structures," *Phys. Rev. B*, vol. 63, no. #, pp. 125417, 2001.

[8] R. Zia, M. D. Selker, M. L. Brongersma, "Leaky and bound modes of surface plasmon waveguides," *Phys. Rev. B*, vol. 71, no. #, pp. 165431, 2005.

[9] S. M. Sze, K. K. Ng, *Physics of Semiconductor Devices*, New York, Wiley, 2006.

[10] Comsol Multiphysic, Finite Element Mode Solver (www.comsol.com).

[11] B. L. Sharma (ed.), *Metal-Semiconductor Schottky Barrier Junctions and Their Applications*, New York, Plenum, 1984.

[12] R. H. Fowler, "The Analysis of Photoelectric Sensitivity Curves for Clean Metals at Various Temperatures," *Phys Rev.*, vol. 38, pp.45-56, 1931.

[13] C. Scales, "Finite Width Plasmon Polariton Waveguide Schottky Barrier Photodetector," *Spectalis Internal Report*, March 2003.

[14] M. Casalino, L. Sirleto, L. Moretti, M. Gioffre, G. Coppola, and I. Rendina, "Silicon resonant cavity enhanced photodetector based on the internal photoemission effect at 1.55 μm: Fabrication and characterization," *Appl. Phys. Lett.*, vol. 92, pp. 251104, 2008.

[15] S. R. J. Brueck, V. Diadiuk, T. Jones, and W. Lenth, "Enhanced quantum efficiency internal photoemission detectors by grating coupling to surface plasma waves," *Appl. Phys. Lett.*, vol. 46, pp. 915-917, 1985.

[16] S. Zhu, M. B. Yu, G. Q. Lo, and D. L. Kwong, "Near-infrared waveguide-based nickel silicide Schottky-barrier photodetector for optical communications," *Appl. Phys. Lett.*, vol. 92, pp. 081103, 2008.

[17] C. Scales and P. Berini, "Schottky Barrier Photodetectors," *U.S. Patent No. 7,026,701* (filed 2004).

[18] R. Charbonneau, C. Scales, I. Breukelaar, S. Fafard, N. Lahoud, G. Mattiussi, and P. Berini, "Passive Integrated Optics Elements Based on Long-Range Surface Plasmon Polaritons," *Jour. Lightwave Tech.*, vol. 24, pp. 477-494, 2006.

Chapter 2

Schottky contact surface-plasmon detector integrated with an asymmetric metal stripe waveguide

2.1 Paper published in Applied Physics Letters

My contribution: The paper included in this chapter was published in Applied Physics Letters and introduces the theoretical model for the performance of the asymmetrically cladded SPP photodetector. The model describing the photoelectric properties of the thin metal stripe contacted on the bottom to silicon is adapted from the model described by Scales and Berini, cited as reference 14 in the paper. The simulation of the structure's waveguiding properties and theoretical performance predictions were made by myself. I prepared all the figures shown in the paper and wrote the initial draft with Dr. Berini providing comments and edits.

Preamble: A Schottky contact photodetector integrated into a finite width metal stripe cladded by air and silicon on top and bottom respectively, which supports short-range surface plasmon polariton modes is presented. The lossy bound mode allows total absorption of the coupled portion of incident optical energy. Performance of an Au stripe on n and p doped Si at an optical wavelength of 1310 nm is described through theoretical prediction of responsivity, dark current, and minimum detectable power.

Schottky contact surface-plasmon detector integrated with an asymmetric metal stripe waveguide

Ali Akbari[1] and Pierre Berini[1,2,a)]
[1]School of Information Technology and Engineering, University of Ottawa, 161 Louis Pasteur St., Ottawa, Ontario K1N 6N5, Canada
[2]School of Information Technology and Engineering, University of Ottawa, 161 Louis Pasteur St., Ottawa, Ontario K1N 6N5, Canada; Department of Physics, University of Ottawa, Ottawa, Canada; and Spectalis Corporation, Ottawa, Ontario K2K 2P4, Canada

(Received 18 May 2009; accepted 16 June 2009; published online 13 July 2009)

A silicon-based Schottky contact photodetector integrated into a finite width asymmetric metal stripe supporting short-range surface plasmon polaritons is presented. Input optical energy is coupled into a bound mode supported by the stripe, leading to total absorption of in-coupled energy. The absorbed energy excites carriers in the metal stripe, some of which cross the Schottky barrier (internal photoemission) leading to a photocurrent under reverse bias. Significant enhancement in the quantum efficiency is observed for a thin metal stripe due to multiple internal reflections of excited carriers. The device holds promise for short-reach high-speed optical interconnects and silicon-based photonic circuitry. © *2009 American Institute of Physics*. [DOI: 10.1063/1.3171937]

Surface plasmon polaritons (SPPs) are TM-polarized surface waves propagating typically along a metal-dielectric interface at optical wavelengths.[1] The SPP is a coupled excitation involving electron oscillations in the metal and an electromagnetic wave. The SPP is localized at the metal-dielectric interface and its fields decay evanescently into both media. The SPP has been the subject of intensive research over the past decade.[2] Thin metal stripes of finite width cladded symmetrically with dielectric have been shown to guide bound SPP modes with lower loss (and lower confinement) relative to the single interface SPP.[3,4] In the case of asymmetric claddings (different claddings above and below the stripe) the bound modes have higher confinement and higher loss.[5–7]

If a lightly doped semiconductor is selected as the dielectric material, a Schottky barrier possessing a rectifying electrical characteristic is formed at the metal-dielectric interface.[8] Such structures have been demonstrated as Schottky photodetectors,[9] enhanced through various schemes such as a resonant cavity[10,11] or through the excitation of SPPs.[12,13] Scales and Berini[14] described a Schottky diode photodetector integrated into a symmetric metal stripe operating in the long-range SPP, and predicted responsivities of 0.1 A/W, dark currents of 21 nA, and minimum detectable powers of −35 dBm at infrared wavelengths (below the bandgap of Si).

In this paper, we present a Schottky diode photodetector integrated into an asymmetric metal stripe propagating short-range SPPs at optical wavelengths. The cross-section of the device, shown in Fig. 1(a), consists of a metal stripe of width w and thickness t, cladded at the bottom by a layer of lightly doped Si (5 Ω cm) on a highly doped Si substrate (0.005 Ω cm) covered by air. This asymmetric structure supports highly confined and highly attenuated SPP modes,[5–7] as opposed to the structure of Scales and Berini[14] which operates in the long-range SPP (LRSPP). The high attenuation of the SPP modes in the asymmetric structure allows for a shorter device compared to that operating in the LRSPP mode. This allows miniaturization of the photodetector and so a reduced device cost due to the larger number of devices per wafer. In addition, the proposed device does not require a silicon upper cladding, which adds cost and may be complex to integrate into the fabrication process of the device. These advantages make the proposed photodetector appealing for low-cost silicon-based photonics.

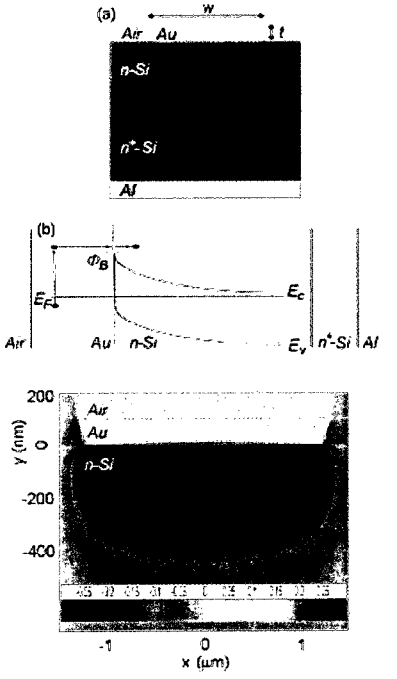

FIG. 1. (Color online) (a) Front view of the photodetector structure on n-Si. The Au/n-Si interface serves simultaneously as part of the waveguide and as a Schottky barrier diode. The highly doped n^+-Si substrate allows efficient conduction of photoelectrons through to the bottom Al Ohmic contact. (b) Energy band diagram showing the internal photoemission process. (c) Perpendicular electric field distribution of the as_y^0 mode. Strong confinement of the field to the Au/Si interface is achieved due to the vertical asymmetry of the waveguide.

a)Electronic mail: berini@site.uottawa.ca.

The diode's photocurrent generation mechanism is internal photoemission, sketched in Fig. 1(b), whereby conduction electrons in the metal absorb photons of sufficiently high energy ($>\Phi_B$, the Schottky barrier height) from the guided SPP mode, gaining enough energy to cross over the Schottky barrier into the semiconductor, where they are swept across the depletion region and collected as photocurrent under reverse bias. The internal quantum efficiency of the device is then dependant on the probability of emission of a hot carrier at the metal-semiconductor interface. For a thin metal stripe, the internal quantum efficiency can experience significant enhancement due to multiple reflections of hot carriers across the thickness of the metal. Following Refs. 11 and 14, the internal quantum efficiency η_i for a thin metal film is given by

$$\eta_i = \frac{1}{h\nu}\int_{\Phi_B}^{h\nu} P(E)dE, \tag{1}$$

where h is Plank's constant, υ is the optical frequency, and Φ_B is the Schottky barrier height (0.34 and 0.80 eV for Au on p-Si and n-Si, respectively[8]). $P(E)$ is the total probability of internal photoemission of a hot carrier, which can be modeled as a carrier traveling back and forth across the thickness of the metal and having a finite probability of emission each time it reaches the metal-semiconductor Schottky barrier. The probability of internal photoemission of a hot carrier having traveled across the metal thickness m times can be expressed as[14]

$$P_m(E) = \frac{1}{2}\left(1 - \sqrt{\frac{\Phi_B}{h\nu e^{-2mt/L}}}\right), \tag{2}$$

where L is the attenuation length of a hot carrier in the metal (55 and 74 nm for holes and electrons in Au, respectively[15]).

This expression arises from the assumption that the carrier's total energy is mostly kinetic and thus, classically, the vector component of its momentum in the direction perpendicular to the barrier must be sufficiently large for internal photoemission to occur. The expression is not valid for cases where the carrier's energy is below the Schottky barrier height, under which classical emission is forbidden and thus the emission probability becomes zero. It is also assumed that photoemission does not occur at the metal-air interface since the energy of hot carriers is less than the work function of the metal at infrared operating wavelengths. A carrier that is not emitted over the Schottky barrier is reflected toward the metal where it eventually reaches the barrier again and thus has another chance of emission. The total probability of photoemission is therefore the sum of the probabilities of carriers that have reflected off the barrier 0 to m times:

$$P(E) = \sum_{m=0}^{\infty} P_m(E)\prod_{k=0}^{m-1}[1 - P_k(E)]. \tag{3}$$

The responsivity R of the photodetector is related to η_i via[14]

$$R = (1 - e^{-\alpha l})\gamma_c \frac{\eta_i}{h\nu}, \tag{4}$$

where α is the mode power attenuation coefficient of the SPP mode, l is the length of the waveguide, and γ_c is the coupling efficiency of the optical source into the SPP mode. The dark current I_{dark} of a Schottky diode is[8]

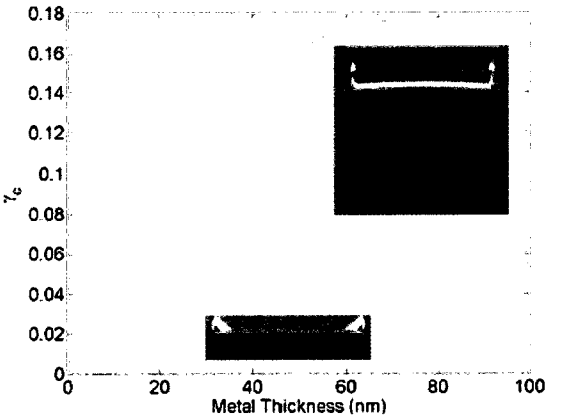

FIG. 2. (Color online) Coupling efficiency into the as_b^0 mode vs metal stripe thickness for a Au/Si Schottky photodetector at λ_0=1310 nm. The coupling efficiency increases with t as the field distribution of the mode evolves from being localized to the metal corners to having a smooth single-lobed distribution along the Au/Si interface (shown as insets for t=15 and 100 nm, respectively).

$$I_{\text{dark}} = C_{\text{area}}A^{**}T^2 e^{-q\Phi_B/kT}, \tag{5}$$

where C_{area} is the contact area, A^{**} is the effective Richardson constant (32 and 112 $\text{Acm}^{-2}\,\text{K}^{-2}$ for holes and electrons, respectively[16]), and T is the absolute temperature. Finally, the photodiode's minimum detectable power is taken as the ratio of the dark current to the responsivity $S_{\min}=I_{\text{dark}}/R$.

The performance of the asymmetric metal stripe was assessed at λ_0=1310 nm assuming Au (ε_r=−86.08−i8.32) (Ref. 17) and Si (ε_r=3.5029[2]) (Ref. 17) as the materials. The field distribution and effective index of the bound SPP modes were computed numerically using a finite element method mode solver.[18] Figure 1(c) shows the typical field distribution of the mode of interest. Note that the mode is symmetric along the width of the stripe exhibiting a single local maximum, and is asymmetric along its thickness; the mode is termed[3] as_b^0. Since the field is highly confined, a tapered PM optical fiber (Panda) having a 2.5 μm spot size[19] was assumed as the means to excite this mode via end-fire coupling. Overlap integrals between the mode field and the input fiber field positioned at the bottom center of the stripe were computed to deduce the coupling efficiency.[20] The computations revealed that the largest coupling efficiency is achieved for w=2.5 μm (stripe width equal to fiber mode diameter). Figure 2 plots the coupling efficiency γ_c as a function of t revealing that it increases with t up to a maximum value of ~18% at t=100 nm. This moderate coupling efficiency is due to strong field confinement and localization of the SPP mode along the bottom interface. The increase in γ_c with t follows the mode evolution, from being strongly confined to the corners of the stripe, to having a main lobe along the stripe width with a lateral Gaussian-like field distribution, as shown as insets at t=15 and 100 nm, respectively. Although the stripe supports many higher order bound modes, coupling efficiencies for these modes are negligible compared to the as_b^0 mode for thick (t~100 nm) stripes.

Tight mode confinement comes with high loss, so waveguide lengths as short as 40 μm absorb more than 99% of the coupled optical energy (α=1276 dB/mm). This short length minimizes the area of the photodetector and enables a

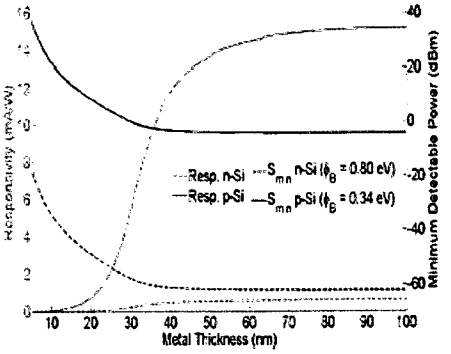

FIG. 3. (Color online) Responsivity and minimum detectable power at λ_0=1310 nm and 300 K vs metal stripe thickness for a Au/Si Schottky photodetector having a stripe area of 2.5×40 μm^2. The best performance is observed for larger t due increased coupling efficiency.

low dark current (5.59 μA for Au on p-Si and 0.36 pA for Au on n-Si for a 2.5×40 μm^2 contact area at 300 K) as well as significant miniaturization of the device. Performance parameters of the photodetector are shown in Fig. 3. A responsivity and minimum detectable power of 15.2 mA/W (0.61 mA/W) and −4.32 dBm (−62.2 dBm), respectively, are achievable at room temperature for a t=100 nm thick Au stripe on p-Si (n-Si). The diode on p-Si has a much better responsivity but it also has a high minimum detectable power. This is not surprising because a low barrier height yields higher quantum efficiencies while allowing higher dark currents through the barrier (however, due to the strong temperature dependence of the dark current, the minimum detectable power in this case can be significantly reduced to −180 dBm if the device is cooled to a temperature of 77 K). An improvement in performance is noticed for large t, due mainly to the improvement in coupling efficiency. The enhancement in the quantum efficiency and responsivity at small t is not noticeable due to the low coupling efficiencies in this case.

Coupling light into the detector from a similar waveguide having a similar field distribution can yield coupling efficiencies of ~100%. Thus it is worth examining the performance of the photodetector assuming perfect coupling efficiency (γ_c=1), as plotted in Fig. 4. The same trade-off between the Schottky barrier height and the performance parameters of the device is noticed; however, significant enhancement in the responsivity at small t due to multiple reflections of hot carriers is seen for a thin metal stripe on p-Si. Not much enhancement is seen for the device on n-Si since the energy range over which the hot electrons can experience multiple reflections is very small because of the larger Schottky barrier height. A responsivity and minimum detectable power of 188.6 mA/W (3.57 mA/W) and −15.3 dBm (−69.9 dBm), respectively, are achievable at room temperature for a t=5 nm thick Au stripe on p-Si (n-Si) (the mode fields in this case are similar to that shown as the lower inset in Fig. 2—highly localized near the corners).

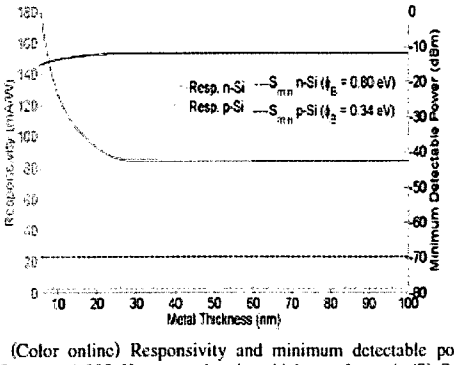

FIG. 4. (Color online) Responsivity and minimum detectable power at λ_0=1310 nm and 300 K vs metal stripe thickness for a Au/Si Schottky photodetector having a stripe area of 2.5×40 μm^2 assuming 100% coupling efficiency. The best performance is observed at smaller t due to the increase in internal quantum efficiency from multiple reflections of hot carriers across the metal.

In summary, a SPP photodetector integrated into an asymmetric metal stripe waveguide has been presented. End-fire excitation by a tapered fiber can yield coupling efficiencies of 18% for which the best responsivity, dark current and minimum detectable power are 15.2 mA/W (0.61 mA/W), 5.59 μA (0.36 pA) and −4.32 dBm (−62.2 dBm), respectively, at room temperature for an Au stripe on p-Si (n-Si). Very low noise amplification would be necessary in order to benefit from the low dark current of the n-Si photodetector. Significant performance enhancement can be achieved when the thickness is reduced to a length comparable to the mean free path of the hot carrier in the metal if 100% coupling efficiency can be obtained. Also, using other metals for the Schottky barrier may provide improved performance. The photodetector performance levels reported are worse than what is achievable using the symmetric metal stripe operating in the long-range SPP,[14] but the asymmetric structure is easier to fabricate. The photodetector could find applications in short-reach high-speed optical interconnects, integrated optics, and in Si-based photonics.

[1]S. A. Maier, *Plasmonics: Fundamentals and Applications* (Springer, New York, 2007).
[2]W. L. Barnes, A. Dereux, and T. W. Ebbesen, Nature (London) **424**, 824 (2003).
[3]P. Berini, Phys. Rev. B **61**, 10484 (2000).
[4]T. Nikolajsen, K. Leosson, I. Salakhutdinov, and S. I. Bozhevolnyi, Appl. Phys. Lett. **82**, 668 (2003).
[5]P. Berini, Phys. Rev. B **63**, 125417 (2001).
[6]R. Zia, M. D. Selker, and M. L. Brongersma, Phys. Rev. B **71**, 165431 (2005).
[7]J.-C. Weeber, J. R. Krenn, A. Dereux, B. Lamprecht, Y. Lacroute, and J. P. Goudonnet, Phys. Rev. B **64**, 045411 (2001).
[8]S. M. Sze and K. K. Ng, *Physics of Semiconductor Devices* (Wiley, New York, 2006).
[9]*Metal-Semiconductor Schottky Barrier Junctions and Their Applications*, edited by B. L. Sharma (Plenum, New York, 1984).
[10]M. Casalino, L. Sirleto, L. Moretti, M. Gioffrè, G. Coppola, and I. Rendina, Appl. Phys. Lett. **92**, 251104 (2008).
[11]H. Elabd and W. F. Kosonocky, RCA Rev. **43**, 569 (1982).
[12]J. A. Shackleford, R. Grote, M. Currie, J. E. Spanier, and B. Nabet, Appl. Phys. Lett. **94**, 083501 (2009).
[13]A. Sellai and P. Dawson, Solid-State Electron. **46**, 29 (2002).
[14]C. Scales and P. Berini, "Schottky Barrier Photodetectors," U.S. Patent No. 7,026,701 (filed 2004).
[15]R. N. Stuart, F. Wooten, and W. E. Spicer, Phys. Rev. Lett. **10**, 7 (1963).
[16]P. Kramer and L. J. van Ruyven, Appl. Phys. Lett. **20**, 420 (1972).
[17]*Handbook of Optical Constants of Solids*, edited by E. D. Palik (Academic, Florida, 1985).
[18]Comsol Multiphysics, Finite Element Mode Solver (www.comsol.com).
[19]Oz Optics, Tapered PM Optical Fiber (TPMJ-X-1550-8/125-0.4-10-2.5-14-1) (www.ozoptics.com).
[20]A. B. Buckman, *Guided-Wave Photonics* (Harcourt Brace Jovanovich, New York, 1992).

2.2 On the convergence and accuracy of the numerical simulations

The Schottky photodetector presented in the previous section of this chapter was simulated through the use of numerical methods. The SPP modes supported by the structure were solved through the use of a finite element method (FEM) mode solver [1]. A meshing algorithm was devised in order to produce the most efficient mesh for the FEM solver in order to balance the trade-off between solution accuracy and required computational power. The algorithm consisted of creating an initial program-generated triangular mesh, with the minimum side length h_{min} equal to the thickness of the metal stripe; with h_{min} to be further reduced in size afterwards, to ensure adequate convergence of the numerical solution. The mesh was dense near the metal dielectric interfaces, and gradually reduced in density as it moved towards the computational boundary. The computational boundary was chosen to be much larger than the SPP field, and perfect electric conductor boundaries were placed at the edges of these to force the solved field intensities to 0, which is characteristic of the bound SPP modes which are confined mainly near the metal stripe. Another function built-in to the finite element mode solver was then used to refine the mesh in a designated rectangular area, whereby each triangular element would get subdivided into two smaller elements. This refining function was first applied twice to a region surpassing the metal's width by 20% and the covering 40 times the metal's thickness from top to bottom. The mesh was then refined in a section covering the bottom and top metal/dielectric interfaces. Finally the mesh was subsequently refined 6 more times in smaller and smaller regions covering the top and bottom corners of the metal stripe. This algorithm produced a mesh which allowed both for the SPP mode's fields to be resolved accurately, since it allowed the fields to peak at the metal-dieletric interface, as well producing a mesh with element size many orders of

magnitude below free-space optical wavelength. Also, this algorithm allowed the mesh size relative to the stripe's width w and thickness t to remain the same, which resulted in a more constant level of accuracy for the solutions obtained across the entire simulation space. In addition, the horizontal symmetry present in the structure about the stripe center allowed to use a perfect magnetic or perfect electric boundary across this axis, in order to solve for the SPP modes which were horizontally symmetric or asymmetric, respectively. This reduced the total number of elements required for the solution by a factor of 2, and allowed more computational power to be used for the solution. Figure 2-1 shows the obtained mesh density for a metal stripe having t = 100 nm and w = 1.5 μm.

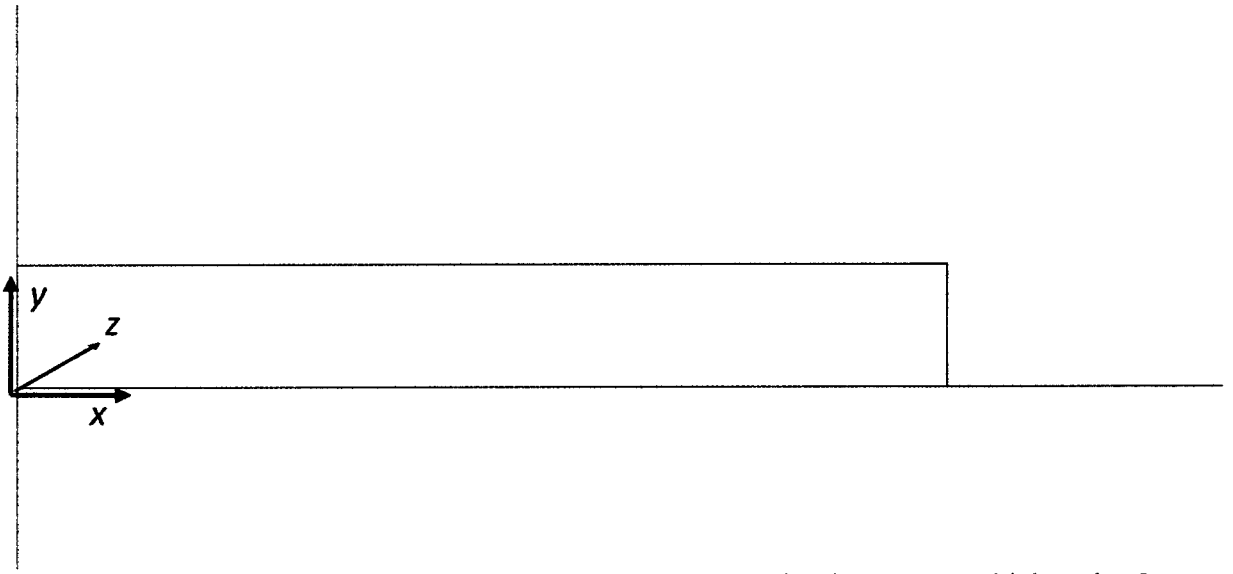

Figure 2-1: Mesh distribution used for FEM solution to a metal stripe 100 nm thick and 1.5 μm wide.

In order to verify that the meshing algorithm allowed sufficient convergence of the FEM solution, the metal stripe's first two symmetric modes (termed as_b^0 and as_b^1) were solved for as a function of h_{min}. Figure 2-2 shows plots of the real part of the effective index n_{eff} obtained by the FEM solution against h_{min}. Parts (a)-(d) show the solution for a Au stripe

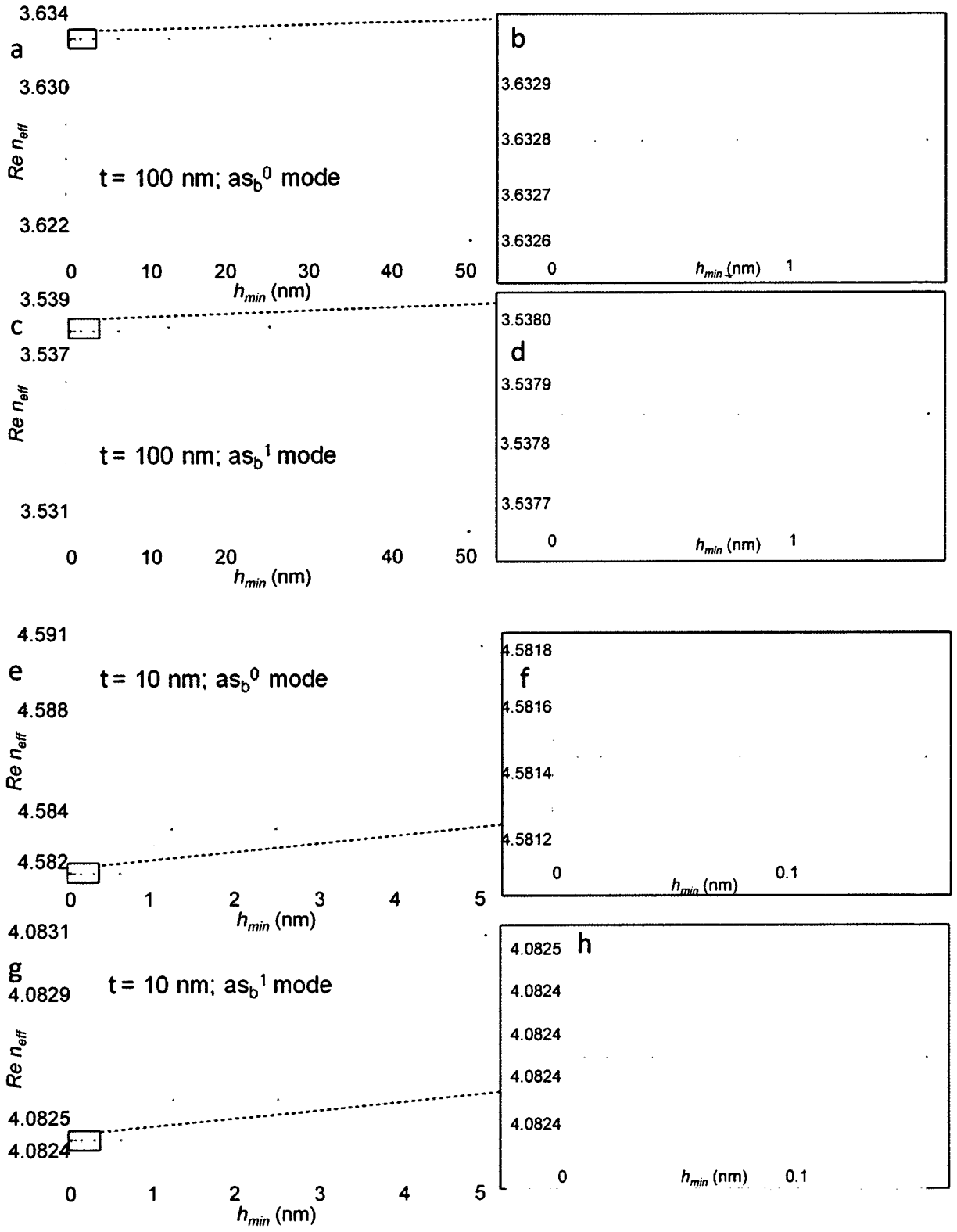

Figure 2-2: Real part of n_{eff} versus h_{min} for an Au stripe of $w = 2.5$ μm, at $\lambda_0 = 1550$ nm. (a)-(d) show results for $t = 100$ nm with (b) and (d) showing results for small h_{min}; (e)-(h) show results for $t = 10$ nm with (f) and (h) showing results for small h_{min}.

with t = 100 nm, w = 2.5 μm, and λ_0 = 1550 nm. Parts (e)-(h) show the solution for a metal with the same w and t = 10 nm. As can be seen, the FEM solution has reached convergence for both t and both modes, since the real part of n_{eff} maintains at least 5 digits of accuracy for the last 6 meshing steps.

To compute the coupling efficiency γ_c of a tapered fiber's output field end-fire coupled into the SPP mode, the overlap integral between the vertical electric field for each is calculated numerically. The tapered fiber having a spot radius of 1.25 μm at a free-space optical wavelength λ_0 = 1550 nm (rated to be 10 % smaller at λ_0 = 1310 nm) [2] is assumed to be TM aligned and placed incident to the bottom center of the metal stripe. The coupling efficiency γ_c is then defined by the normalized total overlap integral between the fiber and SPP's vertical component of electric field [3]

$$\gamma_c = \left| \frac{\iint_{-\infty}^{\infty} E_{y1} E_{y2}^* dA}{\sqrt{\left(\iint_{-\infty}^{\infty} E_{y1} E_{y1}^* dA\right)\left(\iint_{-\infty}^{\infty} E_{y2} E_{y2}^* dA\right)}} \right|^2 \qquad \text{(A.1)}$$

where E_{y1} is the y-directed component of the fiber's electric field, and E_{y2} is the y-directed component of the SPP's electric field. The term in the numerator is the overlap integral between the two fields, while the denominator term is a normalization factor used to obtain a γ_c value between 0 and 1. The two-dimensional integrals are computed numerically across the entire FEM solution area. A rectangular meshing algorithm is used to create an uneven grid mesh in order to split the integral into smaller areas and the integral over each area was computed using a 3x3 point Legendre-Gauss quadrature [4]. The meshing algorithm also

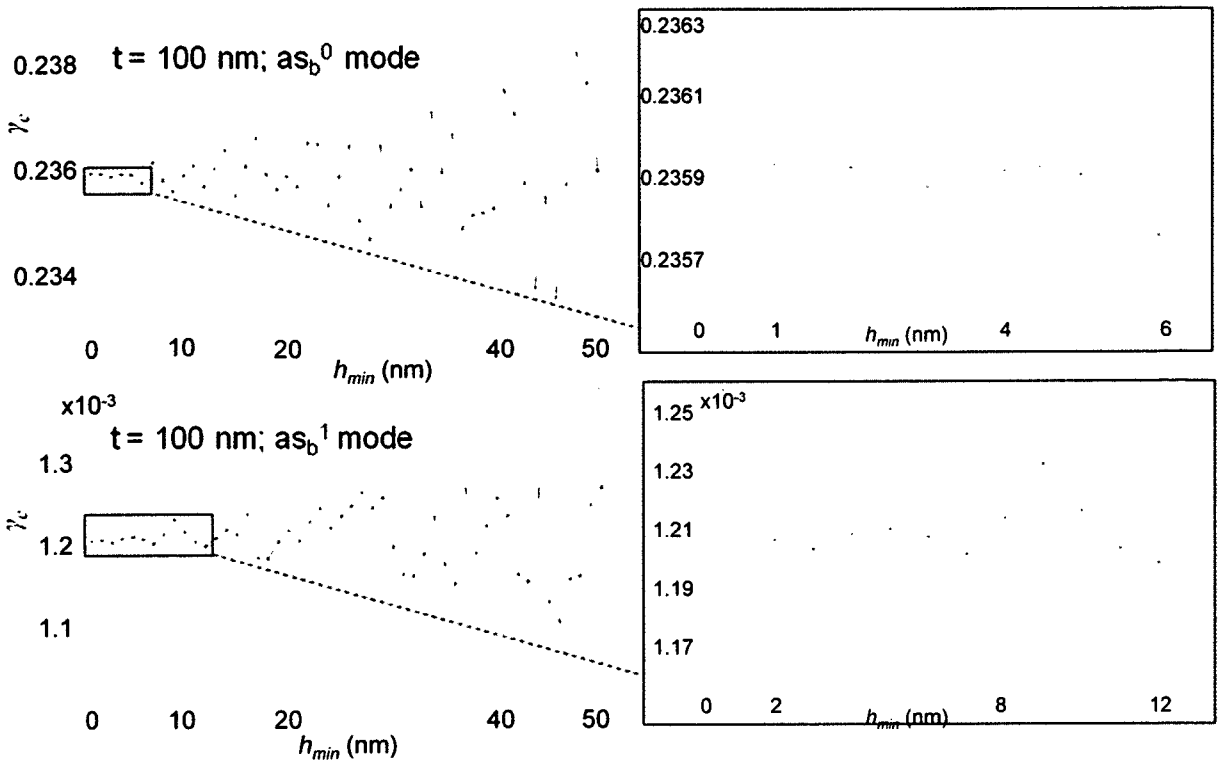

Figure 2-3: γ_c versus h_{min} for an Au stripe of t = 100 nm and w = 2.5 μm, at λ_0 = 1550 nm. (a) and (c) show results for as_b^0 and as_b^1 modes respectively with (b) and (d) showing results for small h_{min}.

generates the areas in sizes proportional to the metal stripe's w and t. The region surrounding the metal stripe is split into rectangles of width $w/50$ and $t/10$, while the region outside of this one but which remains within the tapered fiber's spot diameter is split into squares having 25 nm sides, and the region outside the latter is split into 1 μm squares. The smallest feature of these areas was defined to be h_{min}, and the integral's convergence was verified by computing γ_c as a function of h_{min}, which was adjusted by scaling the mesh size by a constant factor. The results are shown in Figure 2-3, which were computed for both the as_b^0 and as_b^1 modes for an Au stripe of t = 100 nm and w = 2.5 μm, at λ_0 = 1550 nm. Convergence is achieved within 4 digits of accuracy for the as_b^0 mode and 3 digits of accuracy for the as_b^1 mode. It should be noted that convergence is achieved with good confidence for the entire design space since at

for waveguide w and t shown, the field is very tightly confined for the as_b^1 mode and more loosely confined for the as_b^0 mode.

Finally, the accuracy of the implemented numerical method was verified by comparing the FEM and integral algorithm with results for a LRSPP modeled theoretically by the method of lines (MoL) [5]. An Au stripe of t = 24.4 nm and w = 4 μm, which is clad symmetrically by SiO_2 was modeled theoretically by Charbonneau et al., with theoretical γ_c through end-fire coupling at the metal stripe center point using a TM-polarized SMF-28 optical fiber verified experimentally as well [6]. The comparison with the theoretical $\sqrt{\gamma_c}$ values published by Charbonneau et al. in Table 2-1 shows that the numerical modeling is performed with good accuracy. The maximum error of 0.6 % is a good sign that the numerical simulation performed in this thesis is accurate and reliable.

λ_0 (nm)	$\sqrt{\gamma_c}$ (Akbari)	$\sqrt{\gamma_c}$ (Charbonneau)	% Error
1525	0.9567	0.9625	0.603
1550	0.9576	0.9597	0.219
1588	0.9495	0.9529	0.357
1620	0.9401	0.9449	0.508

Table 2-1: Comparison of $\sqrt{\gamma_c}$ values obtained through numerical modeling technique and results published by Charbonneau et al. [6]. The results are for an Au stripe of t = 24.4 nm and w = 4 μm, cladded symmetrically by SiO_2 and end-fire coupled at the stripe center point with a TM-polarized SMF-28 optical fiber.

2.3 Theoretical model of quantum efficiency enhancement of the Schottky photodetector having a thin metal film

This section provides a more thorough description of the theoretical model used to model the quantum efficiency of the detector [7, 8]. The internal photoemission process is modeled as classical emission of a hot charge carrier over the Schottky potential energy barrier formed at the metal/semiconductor interface. Assuming that prior to photon absorption, the electron has energy equal to or below the Fermi level energy (which is true at a temperature of 0 K), the electron's energy will increase by *hv* after absorption. With all this gained energy becoming kinetic energy, the electron can then classically cross over the barrier if its velocity component in the direction normal to the interface contributes to kinetic energy greater than the barrier height. Assuming that the electron has uniform probability of having velocity in all directions and that the density of states in the metal is uniform near the Fermi level, the probability of the electron crossing over the Schottky barrier than becomes the ratio of those velocities which have normal component greater than the barrier, as shown in Figure 2-4. The probability can then be expressed as the ratio of the surface area of a cone to that of the sphere seen in Figure 2-4 [8]

$$P(E) = \frac{1}{2}\left(1 - \sqrt{\frac{\Phi_B}{E}}\right) \qquad (2.1)$$

If the electron does not cross over the barrier, it can travel across the thickness of the film, and provided the metal is thin enough, it can reach back to the metal/semiconductor interface, where it will again have a finite probability of crossing over the barrier if it has

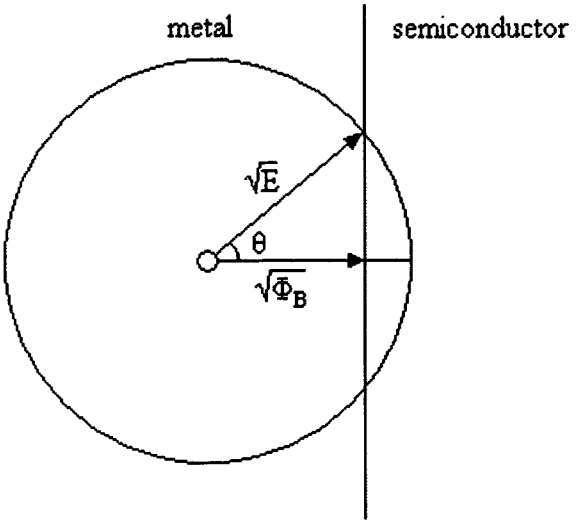

Figure 2-4: Uniform distribution of electron momentum in entire momentum space. Proportion with component in direction normal to interface result in property of barrier crossing (figure shown as published in [8]).

energy greater than the barrier height. If it is assumed that electron energy has a probability of 0 of crossing the metal/air interface barrier (valid if the electron energy is lower than the metal work function), the total probability of a hot electron crossing the Schottky barrier can be expressed as the total probability of all events including an electron reflecting of the interface *m* times. These events are shown in Figure 2-5, where the energy of an electron having travel across the thickness of the metal n times, will have decayed exponentially by a factor proportional to L, the hot carrier attenuation length, where the electron loses energy by a factor of e^{-1} after travelling a distance L. The probability of a hot carrier crossing over the Schottky barrier for a thin metal then becomes expressed as [8]

$$P(E) = \sum_{m=0}^{\infty} P_m(E) \prod_{k=0}^{m-1} [1 - P_k(E)] \qquad (2.2)$$

Where $P_m(E) = \frac{1}{2}\left(1 - \sqrt{\frac{\Phi_B}{\hbar v e^{-2mt/L}}}\right)$ is the probability of emission of an electron having ravelled across the metal *m* times. As shown in the article earlier in this chapter, the internal

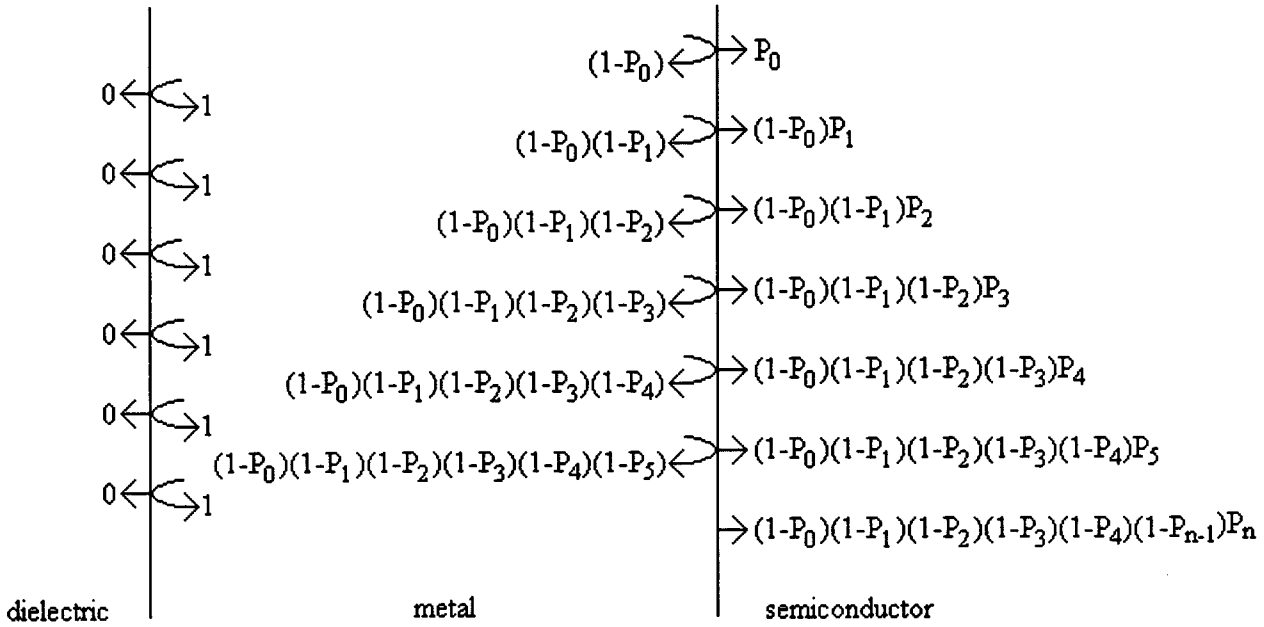

Figure 2-5: Summary of total probability of all events where an electron may travel across the thickness of the barrier *n* times, and become emitted as photocurrent.

quantum efficiency can then be expressed as

$$\eta_i = \frac{1}{h\nu}\int_{\Phi_B}^{h\nu} P(E)dE \qquad (2.3)$$

For the case of a thick film where multiple electron reflections don't have an effect, the expression for η_i becomes reduced to

$$\eta_i = \frac{1}{2}\left(1 - \sqrt{\frac{\Phi_B}{h\nu}}\right)^2 \qquad (2.4)$$

This expression can be further simplified using a Taylor expansion by assuming that the photon energy is close to the barrier energy:

$$\eta_i = \frac{1}{2}\left(1 - \sqrt{\frac{\Phi_B}{h\nu}}\right)^2 = \frac{1}{2}\left(1 - \sqrt{1 + \frac{\Phi_B - h\nu}{h\nu}}\right)^2 = \frac{1}{2}\left(1 - \left[1 + \frac{1}{2}\frac{\Phi_B - h\nu}{h\nu}\right]\right)^2$$

$$\eta_i = \frac{1}{8}\frac{(\Phi_B - h\nu)^2}{(h\nu)^2} = \frac{1}{8}\frac{(h\nu - \Phi_B)^2}{(h\nu)^2} \qquad (2.5)$$

This expression is similar in form to the well known Fowler equation [9, 10]

$$\eta_i = C_1'\frac{(\Phi_B - h\nu)^2}{h\nu} \qquad (2.6)$$

Cohen et al. also modeled the Schottky photodetector and have suggested that the C_1' term can be expressed as $C_1' = {}^1/_{8\Phi_B}$ [9, 11], where in the case where the photon energy and Schottky barrier height are similar, reduces to the exact expression shown in equation (2.5). This close similarity in expressions further supports the validity of the model proposed by Scales and Berini [7, 8], which is used to model the performance of the photodetectors studied in this thesis. In addition, the model was used to characterize the performance of resonant cavity Schottky photodetectors initially measured by Elabd et al. [8, 12].

2.4 References

[1] Comsol Multiphysics, Finite Element Mode Solver (www.comsol.com).

[2] Oz Optics, Tapered PM Optical Fiver (TPMJ-X-1550-8/125-0.4-10-2.5-14-1) (www.ozoptics.com).

[3] A. B. Buckman, *Guided-Wave Photonics*, New York, Harcourt Brace Jovanovich, 1992.

[4] F. B. Hildebrand, *Introduction to Numerical Analysis* (2nd ed.), New York, Dover, 1987.

[5] R. Pregla, W. Pascher, "The method of lines," in *Numerical Techniques for Microwave and Millimeter-Wave Passive Structure,* Ed. By T. Itoh, Wiley, New York, 1989.

[6] R. Charbonneau, C. Scales, I. Breukelaar, S. Fafard, N. Lahoud, G. Mattiussi, P. Berini, "Passive Integrated Optics Elements Based on Long-Range Surface Plasmon Polaritons," *J. Lightwave Technol.*, vol. 24, no. 1, pp. 477-494, 2006.

[7] C. Scales and P. Berini, "Schottky Barrier Photodetectors," *U.S. Patent No. 7,026,701* (filed 2004).

[8] C. Scales, "Finite Width Plasmon Polariton Waveguide Schottky Barrier Photodetector," *Spectalis Internal Report*, March 2003.

[9] R. H. Fowler, "The analysis of photoelectric sensitivity curves for clean metals at various temperatures," *Phys. Rev.*, vol. 38, pp. 45-56, 1931.

[10] B. L. Sharma (ed.), *Metal-Semiconductor Schottky Barrier Junctions and Their Applications*, New York, Plenum, 1984.

[11] W. F. Kosonocky and D. Sarnoff, "Review of Schottky-Barrier Imager Technology," *S.P.I.E.*, vol. 1308, 1990.

[12] H. Elabd and W. F. Kosonocky, "Theory and Measurements of Photoresponse for Thin Film Pd_2Si and PtSi Infrared Schottky-Barrier Detectors With Optical Cavity," *RCA Review*, vol. 43, pp. 569-589, 1982.

Chapter 3

Modeling Schottky contact surface-plasmon detectors based on an asymmetric metal stripe waveguide

My contribution: The paper included in this chapter was submitted for publication to Journal of Applied Physics, and presents further investigation of the theoretical performance of the asymmetrically cladded SPP waveguide photodetector. A detailed study of the SPP modes supported by the metal stripe across a design space of stripe thickness between 5 and 110 nm, and width between 1.5 and 7 μm, is presented. The evolution of the first 3 lower order bound modes, for Au and Al, at wavelengths of 1310 and 1550 nm is discussed. Theoretical calculations of the coupling efficiency from a tapered PM optical fiber are made across the entire waveguide design space. Theoretical predictions of responsivity, dark current, and minimum detectable power are made for all designs considered, with bottom cladding of n-Si and p-Si both considered as well. The simulation of the structure's waveguiding properties and theoretical performance predictions were made by myself. I prepared all the figures shown in the paper and wrote the initial draft with Dr. Berini providing comments and edits.

Preamble: A Schottky contact photodetector integrated into a finite width metal stripe cladded by air and silicon on top and bottom respectively, which supports short-range

surface plasmon polariton modes is presented. The lossy bound mode allows total absorption of the coupled portion of incident optical energy. The carriers in the metal stripe are excited by the absorbed energy and gain enough energy to potentially cross the Schottky barrier and become collected as photocurrent. A hot carrier can reflect many times across a thin metal stripe, and significant enhancement of the quantum efficiency can be observed. Performance of an Au stripe on n and p doped Si at an optical wavelength of 1310 nm is described through theoretical prediction of responsivity, dark current, and minimum detectable power.

Modeling Schottky contact surface-plasmon detectors based on an asymmetric metal stripe waveguide

Ali Akbari[1] and Pierre Berini[1,2,3,*]

[1]School of Information Technology and Engineering, University of Ottawa, 161 Louis Pasteur St., Ottawa, K1N 6N5, Canada

[2]Department of Physics, University of Ottawa, 150 Louis Pasteur St., Ottawa, K1N 6N5, Canada

[3]Spectalis Corporation, P.O. Box 72029, Kanata North RPO, Ottawa, K2K 2P4, Canada

[*]Corresponding Author: berini@site.uottawa.ca

Abstract

Silicon-based surface-plasmon detectors integrated into an asymmetric metal stripe are investigated for different metals, modes, and wavelengths of operation. Low order bound modes supported by Al and Au stripes cladded below by silicon and covered by air are studied at the infrared wavelengths of 1310 and 1550 nm. Input optical power is coupled into the modes supported by the stripe, resulting in total absorption of coupled power over a short device length. The absorbed power creates excited carriers in the metal throughout the modal absorption length, which can cross the Schottky barrier (internal photoemission) and become collected as photocurrent under reverse bias. The device has promise for applications in short-reach high-speed optical interconnects and silicon-based nanophotonics.

Keywords: Surface, Plasmon, Polariton, Photodetector, Silicon, Schottky

I. Introduction

Surface-plasmon polaritons (SPPs) are transverse-magnetic (TM) polarised optical surface waves travelling along the interface between media of negative and positive permittivity, such as a metal-dielectric interface[1]. The SPP arises through a coupling between electron oscillations in the metal and an electromagnetic wave, whose fields decay evanescently from the interface into both media. The SPP has many unique properties, and its ability to provide sub-wavelength field confinement and its high surface sensitivity, have made it the subject of intensive research efforts over the past decade[2]. There have also been many investigations of its potential for waveguiding[3-5] and integrated optics[6,7]. A thin metal stripe of finite width cladded symmetrically by dieletric[4] has been shown to support bound SPP modes having lower loss and confinement than the single-interface SPP[4,8]. In the case of asymmetric claddings, where different dielectrics are used above and below the stripe, the bound SPP modes have higher loss and confinement[9-12].

The interface between a metal and lightly doped semiconductor can also form an electrically rectifying Schottky barrier[13]. This property has been exploited in Schottky photodetectors[14], some integrated with a resonant cavity[15,16] and others exploiting SPP excitation[17-19]. A Schottky photodetector integrated into an SPP waveguide with symmetric[20] and asymmetric[21,22] claddings have also been suggested. The higher attenuation of the SPP mode in the asymmetric structure allows for significant reduction in device length compared to that operating in the long-range SPP in symmetric claddings but this comes at the expense of reduced responsivity[20,21]. The asymmetric structure offers reduced complexity in the fabrication process and its smaller length consumes less wafer area, which are appealing characteristics for low-cost silicon-based photonics.

This paper presents a detailed study of the multiple modes supported by the asymmetric metal stripe on Si, at free-space optical wavelengths of λ_0 = 1310 and 1550 nm, assuming two metals, Au and Al. Schottky contact photodetector performance calculations are also presented assuming end-fire excitation from a tapered optical fibre.

II. Photodetector concept and model

As shown in Fig. 1, the metal stripe of width w and thickness t is cladded at the bottom by a lightly doped Si (5 Ω·cm) layer on a highly doped Si substrate (0.005 Ω·cm), and covered by air. Photons absorbed in the metal create hot charge carriers of sufficient energy to cross over the Schottky barrier and be swept by a voltage bias to be collected at the bottom ohmic Al contact as photocurrent. This process is termed internal photoemission and dominates the photoresponse of the detector at photon energies below the bandgap energy of the semiconductor. The thin lightly doped Si layer is needed to create a sufficiently wide Schottky barrier, while the heavily doped substrate allows more efficient conduction of photocurrent. The structure is assumed end-fire excited via a tapered optical fibre (as discussed further below).

The internal quantum efficiency of the detector η_i can be enhanced through multiple reflections of (non-emitted) hot carriers within the thin metal[16,20,21]. The number of reflections which can occur is limited to the total length a hot carrier can travel before its energy is reduced below the Schottky barrier height; this effect can be modeled via the hot carrier attenuation length L, which is the length that the carrier will travel before its energy decays by a factor of e^{-1} due to scattering processes in the metal. Reflections from the metal-dielectric interfaces are taken as elastic and diffuse. L is taken as 55 and 74 nm for holes and

electrons in Au respectively[23], while 100 nm was found for electrons in Al[24] (in the absence of data the same value is assumed for holes in Al).

The responsivity of a photodetector with given η_i can be expressed as[20]

$$R = (1 - e^{-\alpha l})\gamma_c \frac{\eta_i}{h\nu} \qquad (1)$$

where α is the SPP mode power attenuation (in m^{-1}), l is the waveguide length, γ_c is the coupling efficiency of the optical source into the SPP mode, h is Plank's constant, and ν is the optical frequency. Under reverse bias, the dark current of the device becomes the Schottky diode leakage current and can be expressed as[13]

$$I_{dark} = C_{area} A^{**} T^2 e^{-q\Phi_B/kT} \qquad (2)$$

where C_{area} is the contact area, A^{**} is the effective Richardson coefficient (32 and 112 $Acm^{-2}K^{-2}$ for holes and electrons respectively[25]), T is the absolute temperature and assumed to be 300 K, q is the electron charge, Φ_B is the Schottky barrier height (0.34, 0.8, 0.58, and 0.72 eV for Au/p-Si, Au/n-Si, Al/p-Si, and Al/n-Si respectively[13]), and k is Boltzmann's constant. The device's minimum detectable power is $S_{min} = I_{dark}/R$ assuming that the minimum photocurrent equals the leakage current. With the device's parameters well defined, its performance becomes dependant on careful selection of materials, wavelength, and waveguide geometry.

III. Modes of the asymmetric metal stripe on silicon

A. Modal characteristics

The metal stripe with asymmetric claddings can support many SPP modes with different field distribution and propagation characteristics[9]. The first three bound modes are studied over a wide range of w and t using a commercial finite element mode solver[26]. Cubic spline interpolation of the refractive index data of the adopted materials[27] is used to obtain the required optical parameters at the wavelengths of interest. The interpolated relative permittivities are ε_r = -86.06 - 8.32i and ε_r = -131.9475 - 12.6500i for Au, and ε_r = -174.1717 - 32.6625i and ε_r = -253.9264 - 46.0800i for Al, at λ_0 = 1310 and 1550 nm respectively. Si has negligible absorption at these wavelengths and is thus characterized by its refractive index n = 3.5029 and 3.4764 at λ_0 = 1310 and 1550 nm respectively.

The E_y field distribution for three bound modes supported by the waveguide are shown in Figs. 2(a) and 2(b) for Al and Au respectively, at λ_0 = 1310 nm, for stripe dimensions of w = 4.5 μm and t = 10, 20 and 100 nm. These modes are of interest because they are the first three that exhibit field localization along the metal-Si interface (*i.e.*, overlapping strongly with the Schottky barrier over which internal photoemission is to be maximized). Any other modes supported by the waveguide are not considered in this study.

Following the mode nomenclature of Ref. 9, the as_b^0 and as_b^1 modes have E_y field distributions that are horizontally symmetric about the center of the stripe, while the aa_b^0 mode's field distribution is horizontally asymmetric. All three modes have E_y field distributions that are vertically asymmetric (-like) which is consistent with localization along

the high-index cladding (Si in this case)[9]. The mode fields change appreciably in character as t is varied, as noted from Fig. 2. The as_b^0 and aa_b^0 modes develop strong lobes along the bottom of the stripe as t increases, whereas the as_b^1 mode's field distribution is split between two lobes located at the corners and a central lobe, with the latter's size having a strong dependence on t.

The evolution of the modes with t can also be understood by examining the real part of the modal effective index $\mathrm{Re}\{n_{eff}\}$ and the mode power attenuation α shown in Figs. 3 and 4, respectively, (plotted here in dB/μm). The $\mathrm{Re}\{n_{eff}\}$ and α increase dramatically with decreasing t for all modes and metals as the mode fields overlap more strongly with the metal with decreasing t (following a general trend for modes that are vertically asymmetric-like[4,8]). This effect is due to increased coupling of the top and bottom interfaces through the metal as t decreases. At large t (see zooms in inset), it is noted that $\mathrm{Re}\{n_{eff}\}$ decreases and α increases with increasing mode order, as expected[8], It is also noted that increasing w increases $\mathrm{Re}\{n_{eff}\}$ but decreases α. This is due to the facts that confinement increases with increasing w (thus increasing $\mathrm{Re}\{n_{eff}\}$), and the mode fields interact (overlap) less strongly with the stripe corners which are known to increase loss[4,9] (thus decreasing α).

Comparing Au and Al, it can be seen that $\mathrm{Re}\{n_{eff}\}$ and α are larger for Au despite the fact that Au has a smaller absolute real and imaginary ε_r. Although Al has a greater absolute imaginary ε_r, its greater absolute real part of ε_r reduces the field penetration into the metal which reduces $\mathrm{Re}\{n_{eff}\}$ and α. These observations also hold at $\lambda_0 = 1550$ nm, where additionally $\mathrm{Re}\{n_{eff}\}$ and α are lower than at $\lambda_0 = 1310$ nm because of larger absolute real

part of ε_r, the larger λ_0, and the smaller n for Si, which all contribute to reduce modal confinement.

B. End-fire coupling efficiency

With the waveguide's mode evolution with stripe dimensions (w and t) understood, good designs can then be selected to optimize a photodetector parameter, such as its responsivity R, its dark current I_{dark} or its minimum detectable power S_{min}. R and S_{min} are strongly dependant on γ_c and η_i, with the latter known to be mainly a function of t and Φ_B[20,21]. γ_c however, is directly dependant on the waveguide's dimensions (w and t) because for end-fire coupling, it is determined by the overlap between the excited SPP mode and incident source field distribution[28]

$$\gamma_C = \left| \frac{\iint_{-\infty}^{\infty} E_{y_1} E_{y_2}^{*} dA}{\sqrt{\left(\iint_{-\infty}^{\infty} E_{y_1} E_{y_1}^{*} dA\right)\left(\iint_{-\infty}^{\infty} E_{y_2} E_{y_2}^{*} dA\right)}} \right|^2 \qquad (3)$$

The incident optical source is assumed to be a tapered polarisation-maintaining (PM) optical fibre having a 2.5 μm spot size at λ_0 = 1550 nm (rated to be 10% smaller at λ_0 = 1310 nm)[29]. The fibre is assumed to be TM oriented and aligned to the bottom center of the metal stripe along the facet normal, and the emerging field is assumed to have a Gaussian field distribution characterized by its spot size. The coupling efficiency (γ_c) into each SPP mode is then determined over the w and t range of interest. The results for the as_b^0 and as_b^1 modes are plotted in Fig. 6. The coupling efficiency into the aa_b^0 mode is zero for all w and t because its field distribution is horizontally asymmetric about the center of the stripe, so any positive

field overlap on the right side of the stripe is cancelled out exactly by a negative overlap on the left side for the assumed fibre alignment.

As noted from Fig. 6, the as_b^0 mode is optimally excited at large t (> 80 nm) and for w between 2.5 and 3.5 μm. This is due to the fact that (i) the mode develops a lobe and is less vertically confined at large t (see Fig. 2), and (ii) $w \sim 2.5$ μm corresponds to the spot size of the incident field distribution. The coupling efficiency for the Al stripe is greater than for the Au stripe, because $\mathrm{Re}\{n_{eff}\}$ is smaller for Al (Fig. 3) and consequently the mode fields extend over a larger area (see Fig. 2). The coupling efficiency achievable for the as_b^1 mode is considerably smaller than for the as_b^0 mode because the E_y field of the former is split into central and side lobes of opposite sign. The optimum combination w and t therefore occurs when the central lobe of the E_y field is dominant over the side lobes, and its overlap is optimized with the fiber. These conditions arise at a larger w (~ 5 μm) over a considerably narrower range of t, since the side lobes become larger as t increases (see Fig. 2). In addition, the coupling efficiency is generally larger at $\lambda_0 = 1550$ nm than at $\lambda_0 = 1310$ nm, because the $\mathrm{Re}\{n_{eff}\}$ is lower and the mode fields extend more into the Si cladding.

IV. Photodetector performance characteristics

Having computed the coupling efficiency (γ_c) for the design space of interest, the photodetector's responsivity R is computed using Eq. (1) and η_i computed following Ref. 21. The waveguide length l must first be selected to maximise the absorbed power while minimising I_{dark}; since the lowest α is 0.552 dB/μm, a length $l = 40$ μm is selected to ensure at least 22 dB of absorption.

Fig. 7 shows the computed values of R. Fig. 7(a) shows the contour levels and demonstrates that the w and t dependency of R is essentially the same as that of γ_c. This is principally due to the fact that γ_c is relatively low for these asymmetric SPP waveguides, and R becomes mainly limited by the portion of power coupled into the photodetector. The remaining plots in Fig. 7 show the evolution of R with t, at several w (performance of the Au/n-Si detector is not considered at $\lambda_0 = 1550$ nm because this wavelength is on the edge of cut-off). The corresponding S_{min} for each photodetector is shown in the plots in Fig. 8. The photodetectors generally have better performance at larger t, where the as_b^0 mode is optimally excited. It can also be seen that at large t and $w \sim 2.5$ μm, only the as_b^0 mode is efficiently excited, which is potentially desirable for experimental characterization of the device. A comparable R can also be achieved at lower t, although over a very narrow t range, where the as_b^1 mode is primarily excited. The effect of smaller γ_c for this mode is somewhat offset by the enhancement resulting from multiple hot carrier reflections within the thin metal.

The performance of good w and t designs for each photodetector is summarized in Table 1. The best $R = 15.18$ mA/W can be achieved at $t = 104$ nm and $w = 2.5$ μm with the Au/p-Si device and the as_b^0 mode at $\lambda_0 = 1310$ nm, due to the lowest $\Phi_B = 0.34$ eV and a reasonable $\gamma_c = 17.95$ %; the low Φ_B however results in large $I_{dark} = 5.59$ μA and $S_{min} = -4.34$ dBm. On the other hand, the best $S_{min} = -62.24$ dBm and $I_{dark} = 0.367$ pA are achieved at the same t and w with the Au/n-Si device and the as_b^0 mode at $\lambda_0 = 1310$ nm, due to the highest $\Phi_B = 0.8$ eV; the high Φ_B consequently results in the lowest $R = 0.61$ mA/W. The devices with Al metal stripes have Φ_B between these extrema, and consequently result in photodetectors with a more balanced trade off between R and S_{min}. The Al/p-Si photodetector

can achieve R = 6.59 mA/W and S_{min} = -40.86 dBm at t = 107 nm, w = 2.6 μm, with the as_b^0 mode and λ_0 = 1310 nm, while the Al/n-Si device has R = 2.28 mA/W and S_{min} = -54.34 dBm at the same t, w, λ_0, and with the same mode.

V. Concluding remarks

In conclusion, the SPP metal stripe waveguide with asymmetric claddings was investigated for potential application as an integrated Schottky photodetector. The lower order bound modes supported by the Au and Al stripe cladded by air and silicon on top and bottom respectively, were studied at λ_0 = 1310 and 1550 nm. The lower order bound symmetric as_b^0 (as_b^1) mode can be excited with a reasonable coupling efficiency of γ_c = 24.68 (15.18) and 32.92 (16.23) % for Au and Al stripes respectively, by a PM tapered optical fibre at λ_0 = 1550. The best performance with responsivity, dark current, and minimum detectable power of 15.18 (0.61) mA/W, 5.59 (3.67×10^{-7}) μA, and -4.34 (-62.24) dBm are achieved for a Au/p-Si (Au/n-Si) metal stripe waveguide exciting the as_b^0 mode with w = 2.5 μm, t = 104 nm, and λ_0 = 1310 nm. A better trade off between responsivity, dark current, and minimum detectable power 6.59 (2.28) mA/W, 5.41×10^{-4} (8.42×10^{-6}) μA, and -40.86 (-54.34) dBm is achieved for the Al/p-Si (Al/n-Si) stripe using the as_b^0 mode with w = 2.6 μm, t = 107 nm, and λ_0 = 1310 nm Other metals may provide better performance with more desirable Φ_B and better γ_c. The performance of the investigated photodetector is lower than that of the symmetrically cladded metal stripe which can be coupled more efficiently to the long-range SPP mode[20]. However, the asymmetrically cladded metal stripe is easier and less costly to fabricate. The detector may find applications in integrated optics, short-reach high-speed optical interconnects, and Si-based photonics.

Tables:

Table 1. Performance of various designs of SPP Schottky detectors.

λ_0 (nm)	Metal	Si Type	Mode	γ_c (%)	R (mA/W)	S_{min} (dBm)	I_{dark} (μA)	w (μm)	t (nm)
1310	Au	p-Si	as_b^0	17.95	15.18	-4.34	5.59	2.5	104
			as_b^1	13.22	11.21	-0.28	10.52	4.7	32
		n-Si	as_b^0	17.95	0.61	-62.24	3.67×10^{-7}	2.5	104
			as_b^1	13.22	0.45	-58.19	6.59×10^{-7}	4.7	32
	Al	p-Si	as_b^0	26.68	6.59	-40.86	5.41×10^{-4}	2.6	107
			as_b^1	14.87	4.41	-36.93	8.94×10^{-4}	4.3	14
		n-Si	as_b^0	26.68	2.28	-54.34	8.42×10^{-6}	2.6	107
			as_b^1	14.87	1.28	-49.65	1.40×10^{-5}	4.3	14
1550	Au	p-Si	as_b^0	24.68	17.63	-4.49	6.26	2.8	101
			as_b^1	15.18	11.48	0.22	12.08	5.4	23
	Al	p-Si	as_b^0	32.92	4.18	-38.57	5.82×10^{-4}	2.8	101
			as_b^1	16.23	2.47	-34.02	9.77×10^{-4}	4.7	11
		n-Si	as_b^0	32.92	0.50	-47.41	9.06×10^{-6}	2.8	101
			as_b^1	16.23	0.27	-42.44	1.52×10^{-5}	4.7	11

Figure Captions:

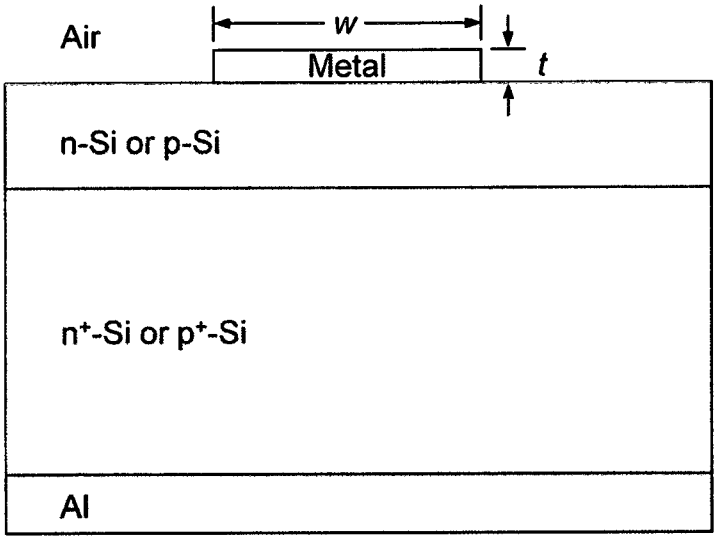

Fig. 1. Front cross-sectional view of the photodetector structure on n-Si. The metal/n-Si interface acts as a Schottky barrier diode, with the cladded stripe supporting bound SPP modes. The highly doped n^+-Si substrate provides low resistivity conduction of photoelectrons through to the bottom Al Ohmic contact.

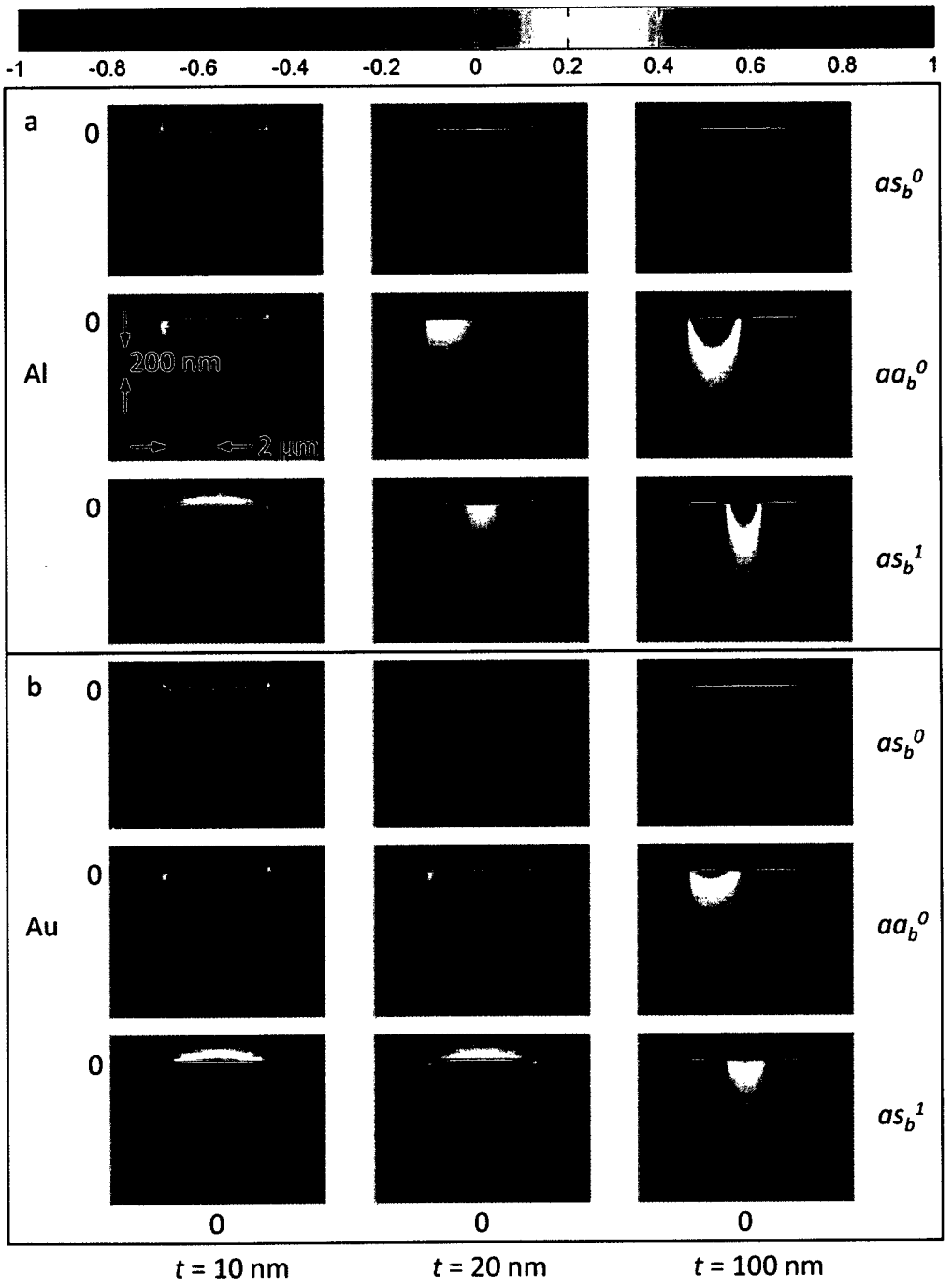

Fig. 2. Field distribution (normalised Re$\{E_y\}$) of the first 3 lower order bound SPP modes supported by an asymmetric metal stripe at $\lambda_0 = 1310$ nm for a stripe width of $w = 4.5$ μm and three thicknesses t; (a) Al stripe; (b) Au stripe.

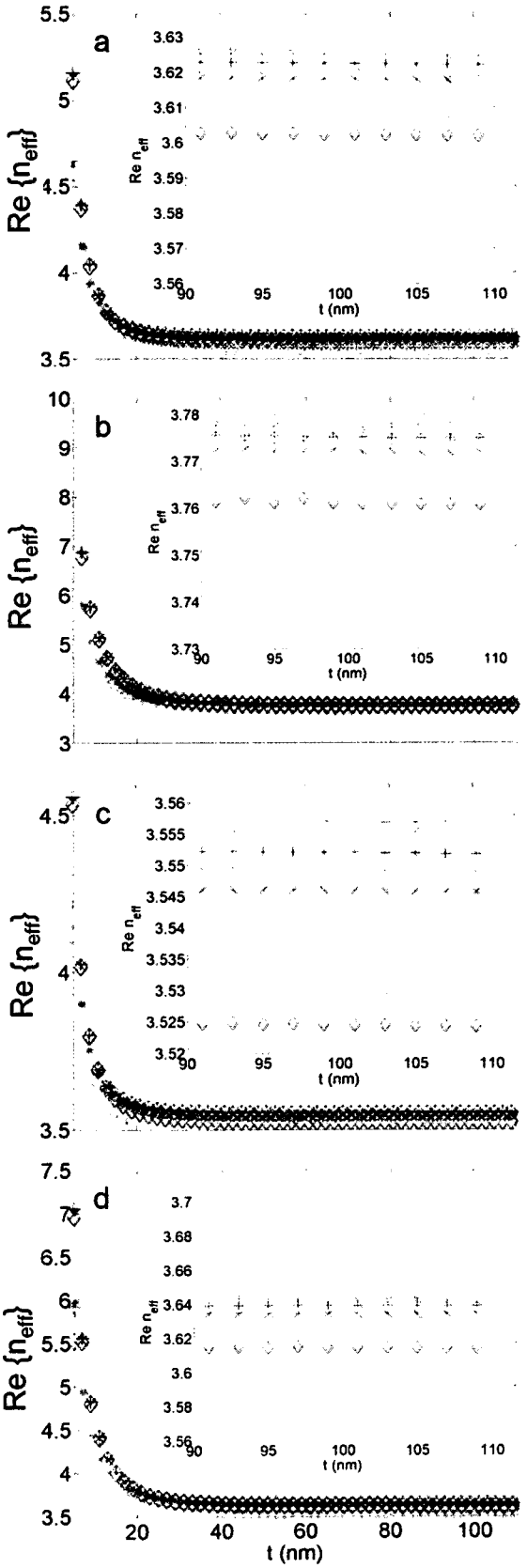
a
b
c
d
Re {n_eff}
Re n_eff
t (nm)

Fig. 3. Real part of effective index n_{eff} versus stripe thickness t for the as_b^0 (◊,×,+), aa_b^0 (◊,×,+), and as_b^1(◊,×,+) modes, and stripe widths w = 2.5 μm (◊), 4.5 μm (×), and 6.5 μm (+); (a) Al at λ_0 = 1310 nm; (b) Au at λ_0 = 1310 nm; (c) Al at λ_0 = 1550 nm; (d) Au at λ_0 = 1550 nm. A zoom-in on the region $90 \leq t \leq 110$ nm is shown in inset for each case.

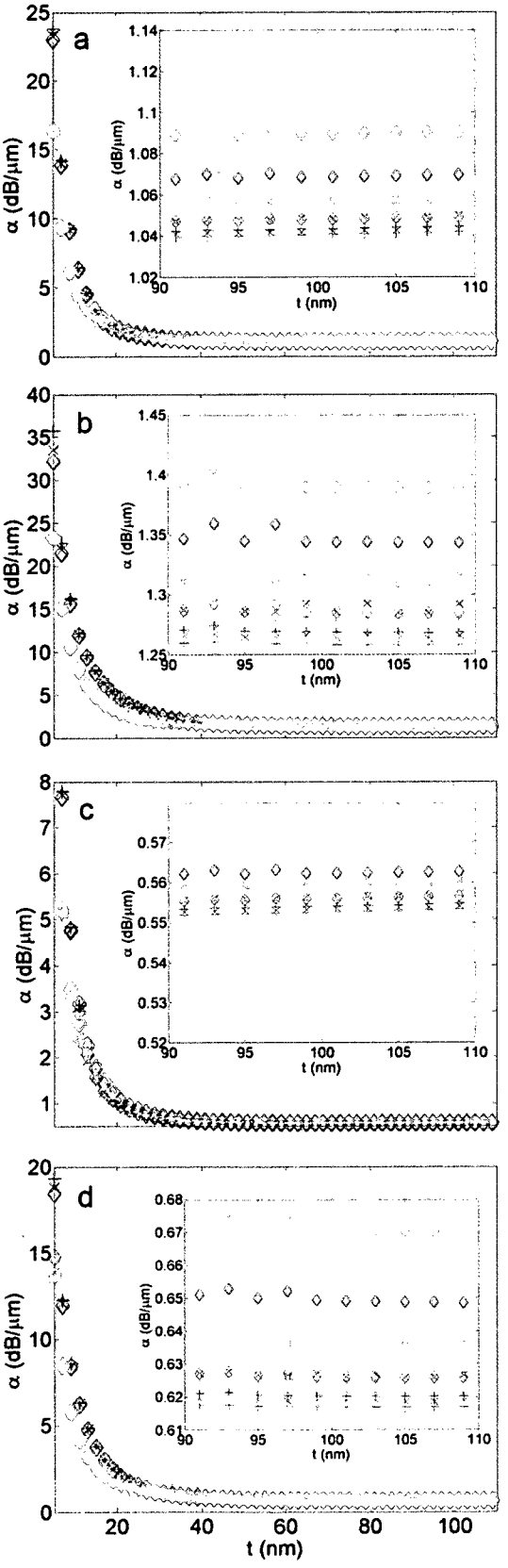
a
b
c
d
α (dB/μm)
t (nm)

Fig. 4. Mode power attenuation α versus stripe thickness t for the as_b^0 (◊,×,+), aa_b^0 (◊,×,+), and as_b^1(◊,×,+) modes, and stripe widths w = 2.5 μm (◊), 4.5 μm (×), and 6.5 μm (+); (a) Al at λ_0 = 1310 nm; (b) Au at λ_0 = 1310 nm; (c) Al at λ_0 = 1550 nm; (d) Au at λ_0 = 1550 nm. A zoom-in on the region $90 \leq t \leq 110$ nm is shown in inset for each case.

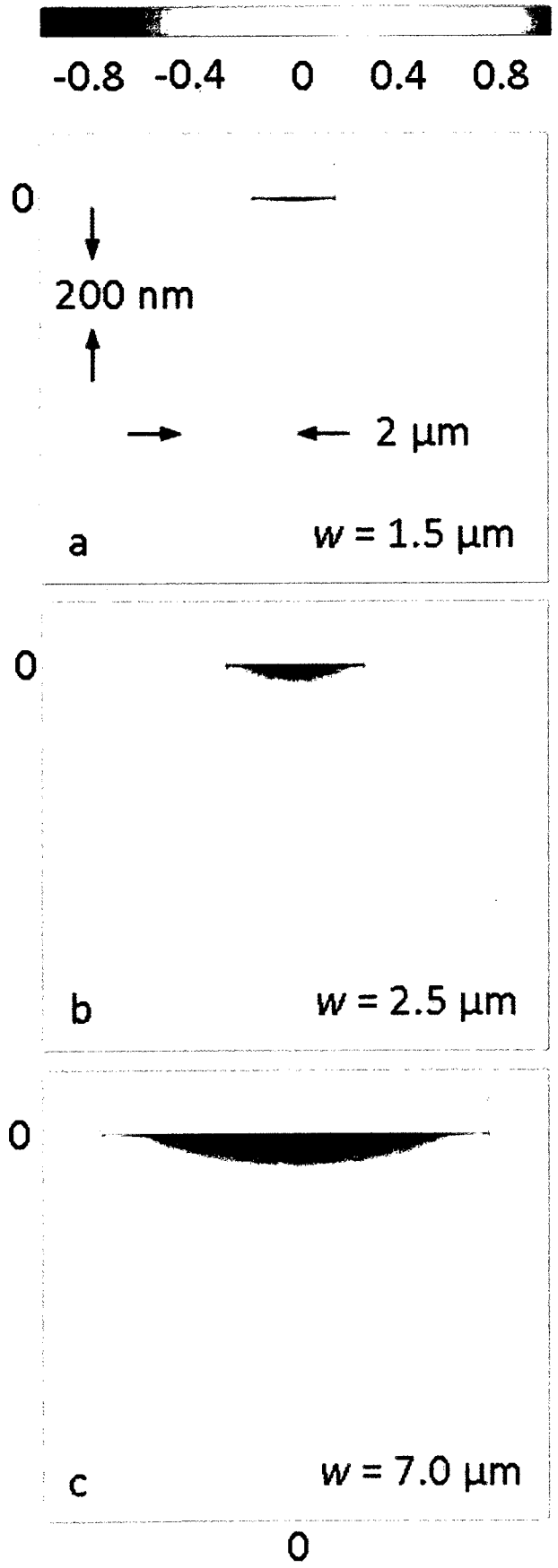
-0.8 -0.4 0 0.4 0.8
0
200 nm
2 µm
a
w = 1.5 µm
0
b
w = 2.5 µm
0
c
w = 7.0 µm
0

Fig. 5. Field distribution (normalised Re$\{E_y\}$) of the as_b^0 mode at λ_0 = 1310 nm, for Au stripes of thickness t = 110 nm and various widths w; (a) w = 1.5 μm; (b) w = 2.5 μm; (c) w = 7.0 μm.

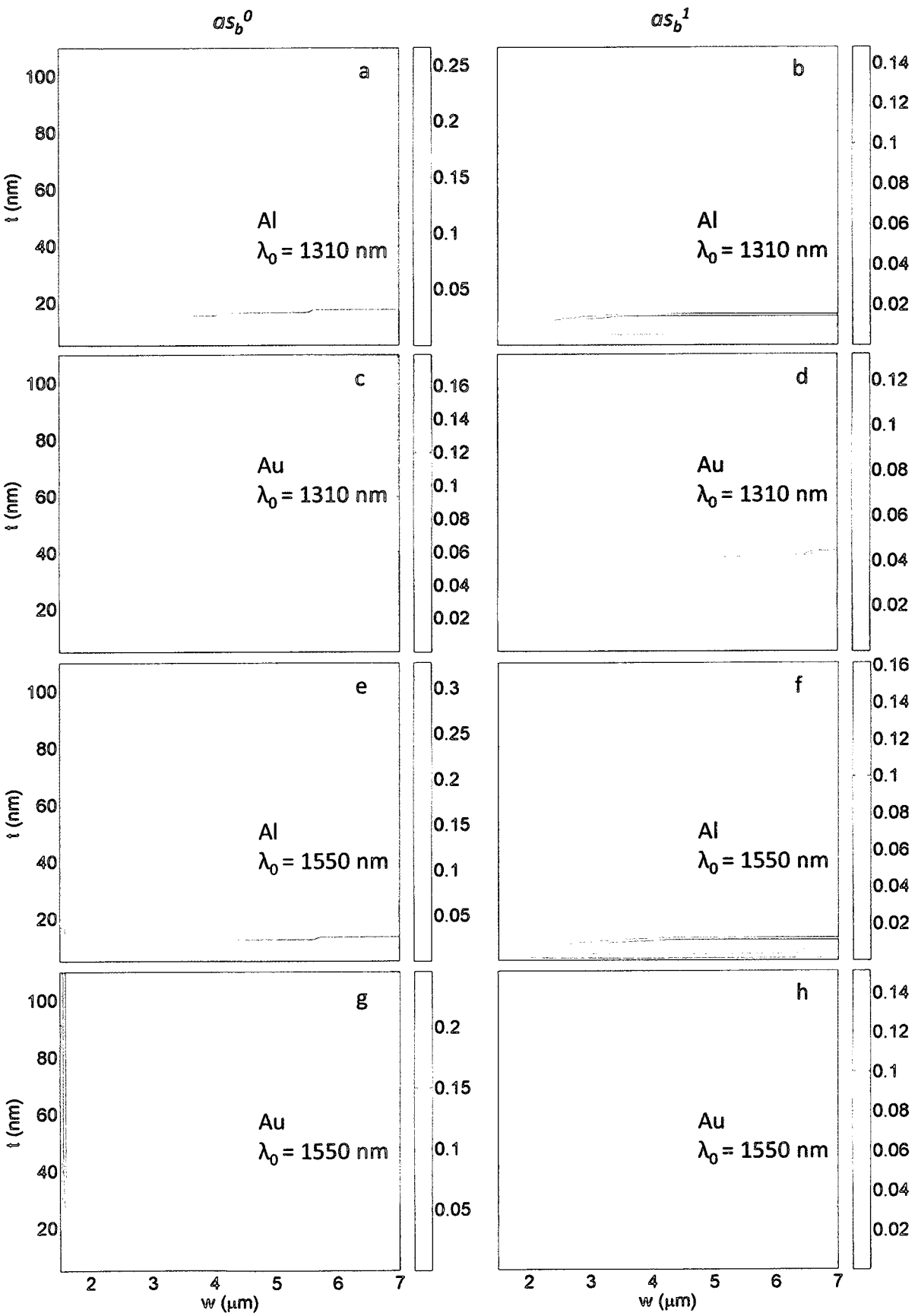
as_b^0
as_b^1
a
b
c
d
e
f
g
h
Al
λ_0 = 1310 nm
Au
λ_0 = 1310 nm
Al
λ_0 = 1550 nm
Au
λ_0 = 1550 nm
t (nm)
w (μm)

Fig. 6. End-fire coupling efficiency γ_c to a tapered optical fibre into the SPP modes as a function of metal stripe width w and thickness t, for all metals and λ_0 considered; (a) as_b^0 mode, Al stripe, $\lambda_0 = 1310$ nm; (b) as_b^1 mode, Al stripe, $\lambda_0 = 1310$ nm; (c) as_b^0 mode, Au stripe, $\lambda_0 = 1310$ nm; (d) as_b^1 mode, Au stripe, $\lambda_0 = 1310$ nm; (e) as_b^0 mode, Al stripe, $\lambda_0 = 1550$ nm; (f) as_b^1 mode, Al stripe, $\lambda_0 = 1550$ nm; (g) as_b^0 mode, Au stripe, $\lambda_0 = 1550$ nm; (h) as_b^1 mode, Au stripe, $\lambda_0 = 1550$ nm.

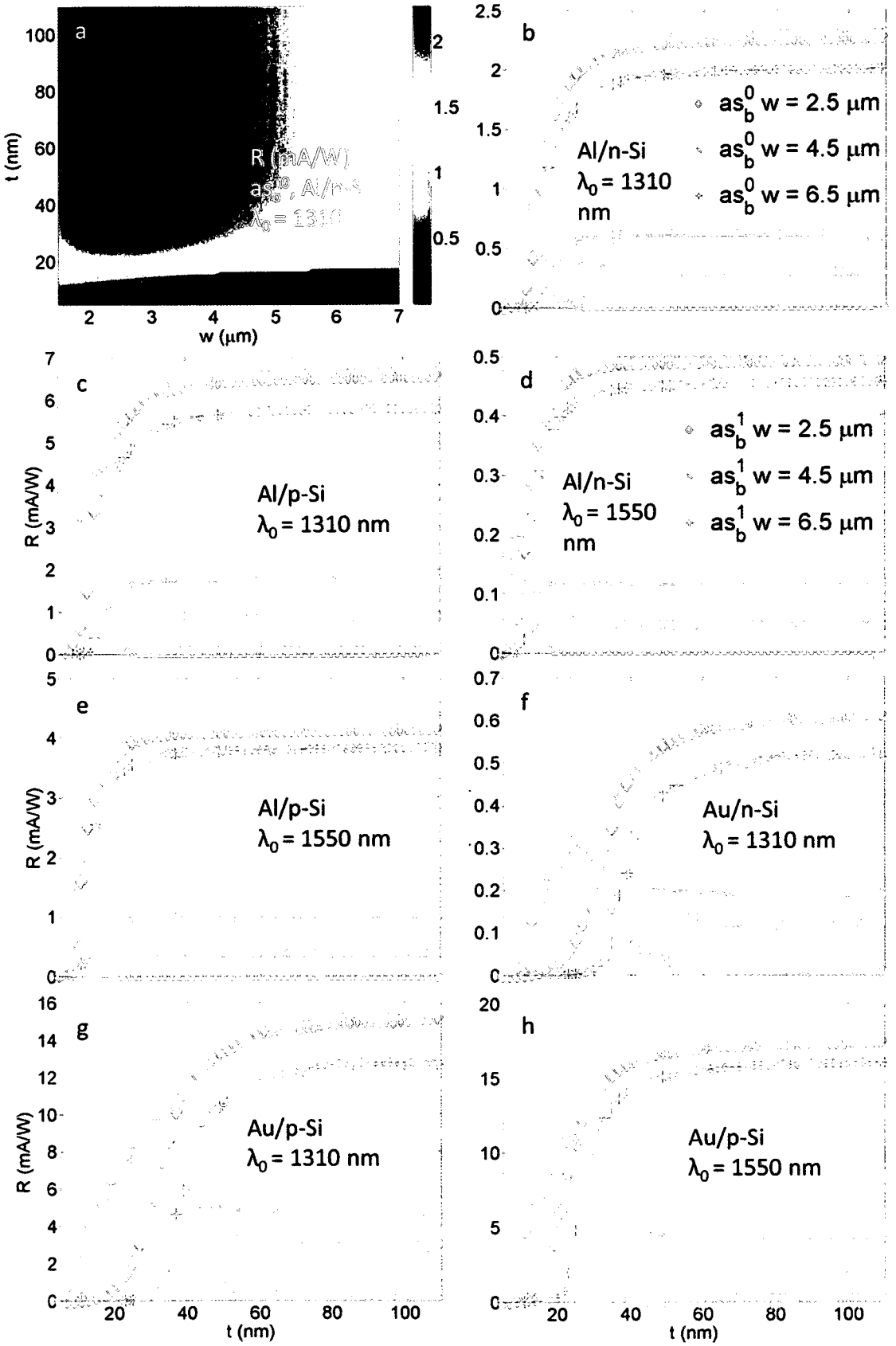
a
t (nm)
w (μm)
b
Al/n-Si
λ0 = 1310 nm
as0b w = 2.5 μm
as0b w = 4.5 μm
as0b w = 6.5 μm
c
R (mA/W)
Al/p-Si
λ0 = 1310 nm
d
Al/n-Si
λ0 = 1550 nm
as1b w = 2.5 μm
as1b w = 4.5 μm
as1b w = 6.5 μm
e
Al/p-Si
λ0 = 1550 nm
f
Au/n-Si
λ0 = 1310 nm
g
Au/p-Si
λ0 = 1310 nm
h
Au/p-Si
λ0 = 1550 nm
t (nm)

Fig. 7. Responsivity R of SPP photodetectors as a function of metal stripe thickness t, for multiples widths w = 2.5 μm (◊), 4.5 μm (×), and 6.5 μm (+), the as_b^0 (◊,×,+) and as_b^1(◊,×,+) modes, two metal-semiconductor combinations, and the two λ_0 considered; (a) contours of R (mA/W), Al/n-Si, as_b^0 mode, λ_0 = 1310 nm; (b) Al/n-Si, λ_0 = 1310 nm; (c) Al/p-Si, λ_0 = 1310 nm; (d) Al/n-Si, λ_0 = 1550 nm; (e) Al/p-Si, λ_0 = 1550 nm; (f) Au/n-Si, λ_0 = 1310 nm; (g) Au/p-Si, λ_0 = 1310 nm; (h) Au/p-Si, λ_0 = 1550 nm.

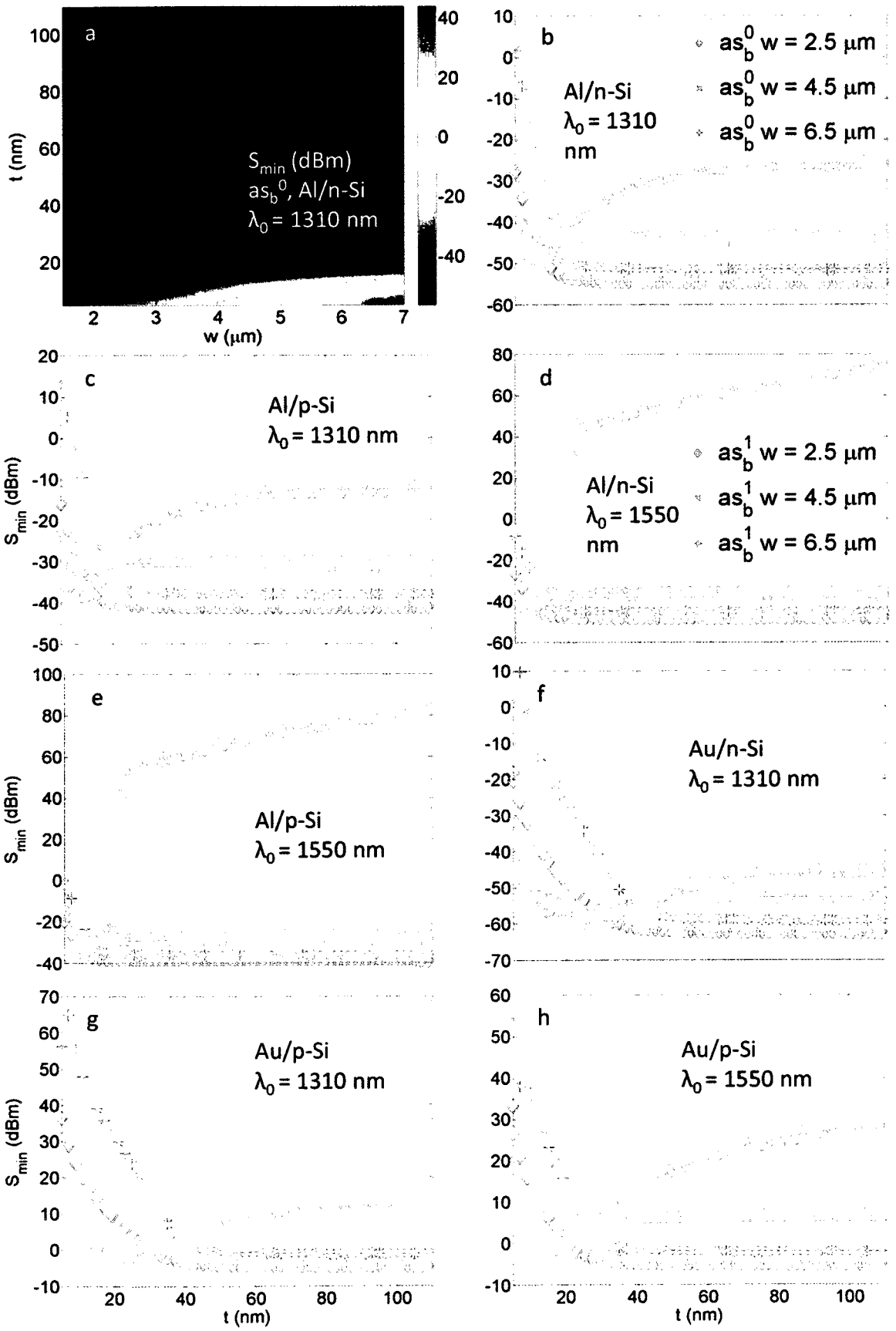
a
S_{min} (dBm)
as_b^0, Al/n-Si
λ_0 = 1310 nm
t (nm)
w (μm)
b
as_b^0 w = 2.5 μm
as_b^0 w = 4.5 μm
as_b^0 w = 6.5 μm
Al/n-Si
λ_0 = 1310 nm
c
Al/p-Si
λ_0 = 1310 nm
S_{min} (dBm)
d
as_b^1 w = 2.5 μm
as_b^1 w = 4.5 μm
as_b^1 w = 6.5 μm
Al/n-Si
λ_0 = 1550 nm
e
Al/p-Si
λ_0 = 1550 nm
f
Au/n-Si
λ_0 = 1310 nm
g
Au/p-Si
λ_0 = 1310 nm
h
Au/p-Si
λ_0 = 1550 nm
t (nm)

Fig. 8. Minimum detectable power S_{min} of SPP photodetectors as a function of metal stripe thickness t, for multiples widths w = 2.5 μm (◊), 4.5 μm (×), and 6.5 μm (+), the as_b^0(◊,×,+) and as_b^1(◊,×,+) modes, two metal-semiconductor combinations, and the two λ_0 considered; (a) contours of S_{min} (dBm), Al/n-Si, as_b^0 mode, λ_0 = 1310 nm; (b) Al/n-Si, λ_0 = 1310 nm; (c) Al/p-Si, λ_0 = 1310 nm; (d) Al/n-Si, λ_0 = 1550 nm; (e) Al/p-Si, λ_0 = 1550 nm; (f) Au/n-Si, λ_0 = 1310 nm; (g) Au/p-Si, λ_0 = 1310 nm; (h) Au/p-Si, λ_0 = 1550 nm.

References

[1]S. A. Maier, *Plasmonics: Fundamentals and Applications* (Springer, New York, 2007).

[2]W. L. Barnes, A. Dereux, and T. W. Ebbesen, Nature (London) **424**, 824 (2003).

[3]A. Hohenau, J. R. Krenn, A. L. Stephanov, A. Drezet, H. Ditlbacher, B. Steinberger, A. Leitner, and F. R. Aussenegg, Opt. Lett. **30**, 893 (2005).

[4]P. Berini, Phys. Rev. B **61**, 10484 (2000).

[5]T. Nikolajsen, K. Leosson, I. Salakhutdinov, and S. I. Bozhevolnyi, Appl. Phys. Lett. **82**, 668 (2003).

[6]R. Charbonneau, C. Scales, I. Breukelaar, S. Fafard, N. Lahoud, G. Mattiussi, and P. Berini, J. Lightwave Technol. **24**, 477 (2006).

[7]A. Boltasseva, T. Nikolajsen, K. Leosson, K. Kjaer, M. S. Larsen, and S. I. Bozhevolnyi, J. Lightwave Technol. **23**, 413 (2005).

[8]P. Berini, Adv. Opt. Phot. **1**, 484 (2009).

[9]P. Berini, Phys. Rev. B **63**, 125417 (2001).

[10]R. Zia, M. D. Selker, and M. L. Brongersma, Phys. Rev. B **71**, 165431 (2005).

[11]J.-C. Weeber, J. R. Krenn, A. Dereux, B. Lamprecht, Y. Lacroute, and J. P. Goudonnet, Phys. Rev. B **64**, 045411 (2007).

[12]E. Verhagen, A. Polman, and L. Kuipers, Optics Express **16**, 45 (2008).

[13]S. M. Sze and K. K. Ng, *Physics of Semiconductor Devices* (Wiley, New York, 2006).

[14]*Metal-Semiconductor Schottky Barrier Junctions and Their Applications*, edited by B. L. Sharma (Plenum, New York, 1984).

[15]M. Casalino, L. Sirleto, L. Moretti, M. Gioffrè, G. Coppola, and I. Rendina, Appl. Phys. Lett. **92**, 251104 (2008).

[16]H. Elabd and W. F. Kosonocky, RCA Rev. **43**, 569 (1982).

[17]S. R. J. Brueck, V. Diadiuk, T. Jones, and W. Lenth, Appl. Phys. Lett. **46**, 915 (1985).

[18]K. M. Torosian, A. S. Karakashian, and Y. Y. Teng, Appl. Opt. **26**, 2650 (1987).

[19]C. Daboo, M. J. Baird, H. P. Hughes, N. Apsley, and M. T. Emeny, Thin Solid Films **201**, 9 (1991).

[20]C. Scales and P. Berini, "Schottky Barrier Photodetectors," U.S. Patent No. 7,026,701 (filed 2005).

[21]A. Akbari and P. Berini, Appl. Phys. Lett. **95**, 021104 (2009).

[22]A. Akbari, R. N. Tait, and P. Berini, *Surface plasmon waveguide Schottky detector*, submitted.

[23]R. N. Stuart, F. Wooten, W. E. Spicer, Phys. Rev. Lett. **10**, 7 (1963).

[24]J. J. Quinn, Phys. Rev. **126**, 1453 (1962).

[25]P. Kramer and L. J. van Ruyven, Appl. Phys. Lett. **20**, 420 (1972).

[26]Comsol Multiphysics, (www.comsol.com).

[27]*Handbook of Optical Constants of Solids*, edited by E. D. Palik, Academic, Florida, 1985.

[28]A. B. Buckman, *Guided-Wave Photonics* (Harcourt Brace Jovanovich, New York, 1992).

[29]Oz Optics, Tapered PM Optical Fiber (TPMJ-X-1550-8/125-0.4-10-2.5-14-1) (www.ozoptics.com).

Chapter 4

Surface Plasmon waveguide Schottky detector

4.1 Paper submitted to Optics Express

My contribution: The paper included in this chapter was submitted for publication to Optics Express and reports experimental measurements made on the fabricated SPP photodetector. The fabrication process and experimental setup is described in detail. Current versus voltage measurements are used to characterize the device's electrical characteristics. Photocurrent is measured against incident optical power and wavelength to compare the photodetector's performance to theory and estimate the coupling efficiency. Responsivity and dark current measurements characterize the performance of the device. The lithography mask design and fabrication process was implemented by myself under the guidance and advice of Dr. Tait, Dr. Berini, and the technical staff at Carleton University's clean room facility. Cleaving, device preparation, experimental setup, and measurements were also done by me under guidance and advice of Dr. Berini. Ewa Lisicka-Skrzek provided technical advice for design the layout for the fabrication mask, as well as for preparing the experimental setup. I prepared all the figures shown in the paper and wrote the initial draft with Dr. Berini providing comments and edits.

Preamble: Fabrication and experimental measurement of a surface plasmon Schottky photodetector are described. Au and Al metal stripe waveguides having width $w = 2.5$ μm and thickness $t \sim 135$ nm, cladded on the bottom and top by n-Si and air respectively, are

excited using a TM beam incident from a tapered PM optical fiber. Electrical measurements reveal Schottky barrier height $\Phi_B \sim 0.75$ and 0.46 eV for Au/n-Si and Al/n-Si devices respectively. Optical measurements of photocurrent against incident optical power reveal responsivities ranging from $R = 0.0087$ (0.8960) mA/W at a wavelength of 1620 nm, to $R =$ 0.3848 (1.0401) mA/W at a wavelength of 1280 nm, for the Au/n-Si (Al/n-Si) device. The dark current of the device is 10 nA (6 μA), which can be significantly reduced by reducing the Schottky contact area. Measurements of photocurrent against incident optical power and comparison to theoretically modelled performance allow estimating the coupling efficiencies into the SPP waveguide to be 4.32 and 3.27 % respectively. The low coupling efficiencies measured are due mainly to strict alignment requirements which could not be perfectly met with the implemented experimental setup. However, comparably null measurements of the photocurrent under excitation with a TE polarized beam present strong evidence for the successful demonstration of SPP detection.

Surface plasmon waveguide Schottky detector

Ali Akbari,[1] R. Niall Tait,[2] and Pierre Berini[1,3,4,*]

[1]*School of Information Technology and Engineering, University of Ottawa, 161 Louis Pasteur St., Ottawa, K1N 6N5, Canada*
[2]*Department of Electronics, Carleton University, 1125 Colonel By Drive, Ottawa, K1S 5B6, Canada*
[3]*Department of Physics, University of Ottawa, 150 Louis Pasteur St., Ottawa, K1N 6N5, Canada*
[4]*Spectalis Corporation, P.O. Box 72029, Kanata North RPO, Ottawa, K2K 2P4, Canada*

Abstract: A surface plasmon polariton detector is demonstrated at infra-red wavelengths. The device consists of a metal stripe on silicon forming a Schottky contact thereon and supporting surface a plasmon polariton mode that is strongly confined and localised to the metal – semiconductor interface. Detection of optical radiation below the bandgap of silicon (at infrared wavelengths) occurs through internal photoemission. Responsivities of 0.38 and 1.04 mA/W were measured via end-fire coupling to a tapered optical fibre, at room temperature and at a wavelength of 1280 nm, for gold and aluminium stripes on n-type silicon, respectively. The device can be integrated with other structures used in nano-plasmonics, nano-photonics or silicon-based photonics, and it holds promise for short-reach optical interconnects and power monitoring applications.

OCIS codes: (240.6680) Surface plasmons; (250.0040) Detectors.

References and links

1. W. L. Barnes, A. Dereux, T. W. Ebbesen "Surface plasmon subwavelength optics," Nature **424**, 824-830 (2003).
2. S. A. Maier, *Plasmonics: Fundamentals and Applications* (Springer, New York, USA, 2007).
3. P. Berini, "Bulk and surface sensitivities of surface plasmon waveguides," New J. Phys. **10**, 105010 (2008).
4. P. Berini, "Plasmon-polariton waves guided by thin lossy metal films of finite width: Bound modes of symmetric structures," Phys. Rev. B **61**, 10484-10503 (2000).
5. P. Berini, "Plasmon-polariton waves guided by thin lossy metal films of finite width: Bound modes of asymmetric structures," Phys. Rev. B **63**, 125417 (2001).
6. B. Lamprecht, J. R. Krenn, G. Schider, H. Ditlbacher, M. Salerno, N. Felidj, A. Leitner, F. R. Aussenegg, "Surface plasmon propagation in microscale metal stripes," Appl. Phys. Lett. **79**, 51-53 (2001).
7. J.-C. Weeber, J. R. Krenn, A. Dereux, B. Lamprecht, Y. Lacroute, J. P. Goudonnet, "Near-field observation of surface plasmon polariton propagation on thin metal stripes," Phys. Rev. B **64**, 045411 (2001).
8. T. Nikolajsen, K. Leosson, I. Salakhutdinov, S. I. Bozhevolnyi, "Polymer-based surface-plasmon-polariton stripe waveguides at telecommunication wavelengths," Appl. Phys. Lett. **82**, 668-670 (2003).
9. R. Zia, M. D. Selker, M. L. Brongersma, "Leaky and bound modes of surface plasmon waveguides," Phys. Rev. B **71**, 165431 (2005).
10. E. Verhagen, A. Polman, L. Kuipers, "Nanofocusing in laterally tapered plasmonic waveguides," Opt. Express **16**, 45-57 (2008).
11. R. Charbonneau, C. Scales, I. Breukelaar, S. Fafard, N. Lahoud, G. Mattiussi, P. Berini, "Passive integrated optics elements based on long-ranging surface plasmon polaritons," J. Lightwave Technol. **24**, 477-494 (2006).
12. B. Steinberger, A. Hohenau, H. Ditlbacher, F. R. Aussenegg, A. Leitner, J. R. Krenn, "Dielectric stripes on gold as surface plasmon waveguides: Bends and directional couplers," Appl. Phys. Lett. **91**, 081111 (2007).
13. T. Holmgaard, Z. Chen, S. I. Bozhevolnyi, L. Markey, A. Dereux, A. V. Krasavin, A. V. Zayats, "Bend- and splitting loss of dielectric-loaded surface plasmon-polariton waveguides," Opt. Express **16**, 13585-13592 (2008).
14. T. W. Ebbesen, C. Genet, S. I. Bozhevolnyi, "Surface plasmon circuitry", Physics Today **61**, 44-50 (2008).
15. J. Homola, S. S. Yee, G. Gauglitz, "Surface plasmon resonance sensors: review," Sens. Act. B **54**, 3-15 (1999).
16. P. Berini, "Long-range surface plasmon-polaritons," Adv. Opt. Phot. **1**, 484-588 (2009).
17. S. M. Sze, K. K. Ng, *Physics of Semiconductor Devices* (Wiley, New York, USA, 2006).
18. M. Casalino, L. Sirleto, L. Moretti, M. Gioffrè, G. Coppola, I. Rendina, "Silicon resonant cavity enhanced photodetector based on the internal photoemission effect at 1.55 μm: Fabrication and characterization," Appl. Phys. Lett. **92**, 251104 (2008).
19. H. Elabd, W. F. Kosonocky, "Theory and measurements of photoresponse for thin film Pd_2Si and PtSi infrared Schottky-barrier detectors with optical cavity," RCA Review **43**, 569-589 (1982).
20. S. R. J. Brueck, V. Diadiuk, T. Jones, W. Lenth, "Enhanced quantum efficiency internal photoemission detectors by grating coupling to surface plasma waves," Appl. Phys. Lett. **46**, 915-917 (1985).
21. K. M. Torosian, A. S. Karakashian, Y. Y. Teng, "Surface plasma-enhanced internal photoemission in gallium arsenide Schottky diodes," Appl. Opt. **26**, 2650-2652 (1987).
22. C. Daboo, M. J. Baird, H. P. Hughes, N. Apsley, M. T. Emeny, "Improved surface plasmon enhanced photodetection at an Au-GaAs Schottky junction using a novel molecular beam epitaxy grown Otto coupling structure," Thin Solid Films **201**, 9-27 (1991).

23. S. Zhu, M. B. Yu, G. Q. Lo, D. L. Kwong, "Near-infrared waveguide-based nickel silicide Schottky-barrier photodetector for optical communications," Appl. Phys. Lett. **92**, 081103 (2008).
24. C. Scales, I. Breukelaar, P. Berini, "Surface-plasmon Schottky contact detector based on a symmetric metal stripe in silicon," Opt. Lett. **35**, 529-531 (2009).
25. A. Akbari, P. Berini, "Schottky contact surface-plasmon detector integrated with an asymmetric metal stripe waveguide," Appl. Phys. Lett. **95**, 021104 (2009).
26. Oz Optics, Tapered PM Optical Fiber (TPMJ-X-1550-8/125-0.4-10-2.5-14-1) (www.ozoptics.com)
27. A. B. Buckman, *Guided-Wave Photonics* (Harcourt Brace Jovanovich, New York, USA, 1992).
28. E. D. Palik, Ed. *Handbook of Optical Constants of Solids* (Academic, Orlando, USA, 1985).
29. P. Kramer, L. J. van Ruyven, "Position of the band edges of silicon under uniaxial stress," Appl. Phys. Lett. **20**, 420-422 (1972).
30. P. Berini, N. Lahoud, R. Charbonneau, "Fabrication of surface plasmon waveguides and integrated components on ultrathin freestanding membranes," J. Vac. Sci. Technol. A **26**, 1383-1391 (2008).
31. V. Aubry, F. Meyer, "Schottky diodes with high series resistance: Limitations of forward I-V methods," J. Appl. Phys. **76**, 7973-7984 (1994).
32. C.-D. Lien, F. C. T. So, M.-A. Nicolet, "An improved forward I-V method for nonideal Schottky diodes with high series resistance," IEEE Trans. Electron Devices **31**, 1502-1503 (1984).
33. J. H. Werner, "Schottky barrier and pn-junctionI/V plots - Small signal evaluation," Appl. Phys. A **47**, 291-300 (1988).
34. J. M. Mooney, "The dependence of the Schottky emission coefficient on reverse bias," J. Appl. Phys. **65**, 2869-2871 (1989).

1. Introduction

Over recent years, the field of plasmonics has undergone intensive research efforts [1]. Plasmonics consists of the study of the properties and applications of surface plasmon polaritons (SPPs), which are optical surface waves propagating along the interface between a metal and a dielectric. The SPP is a coupled excitation propagating as a charge density wave in the metal coupled to electromagnetic fields, with its fields decaying evanescently in both the metal and the dielectric [2]. The SPP has many interesting properties, including field confinement on a sub-wavelength scale [1] and very high surface and bulk sensitivities [3]. These properties have resulted in many applications of SPPs in waveguiding [4-10], integrated optics [11-14], and sensing [15], to name a few. Developments on waveguiding of SPPs have shown, for instance, that a thin metal stripe of finite width embedded in a homogeneous dielectric cladding (symmetric structure) can support a long-range SPP (LRSPP), which propagates with lower loss and confinement than the single interface SPP [4, 16]. A metal stripe with different dielectric claddings above and below the stripe (asymmetric structure) will also support bound SPP modes, but with higher confinement and loss than the LRSPP [5-7, 9, 10].

Selecting a lightly doped semiconductor as (one of) the dielectric cladding(s) of the metal stripe allows the formation of a Schottky contact at the material interface [17], conferring additional functionality to the structure. The Schottky diode structure has been widely investigated as an infra-red detector, for photon energies below the bandgap of the semiconductor [17]. Numerous enhancements to the basic structure have been proposed, through resonant cavity enhancement [18, 19], by SPP excitation [20-22], and by merging with a dielectric waveguide [23]. Integration of a Schottky barrier detector with a metal stripe waveguide supporting SPPs has been investigated theoretically for symmetric [24] and asymmetric [25] silicon claddings. In this paper we demonstrate the operation of the asymmetric structure, and we present and discuss experimental results quantifying its performance as a SPP detector at photon energies below the bandgap of Si.

2. Device structure and operation

Fig. 1(a) shows an isometric sketch of the device, with the metal stripe of width w, length l and thickness t acting simultaneously as a SPP waveguide and a Schottky contact to the underlying n-type Si (n-Si). The detection mechanism is internal photoemission: Absorption of SPPs by the metal stripe results in conduction electrons therein becoming excited (hot electrons), and if the energy $h\nu$ (h - Planck's constant, ν - optical frequency) of the SPP is sufficiently large, the electrons can gain sufficient energy to cross the Schottky barrier Φ_B, and be emitted into the semiconductor where they are collected as photocurrent [24, 25]. Thus detection occurs for photon energies below the bandgap of the semiconductor but larger than the Schottky barrier height. (If the energy is greater than the bandgap, then electron-hole pair creation in the semiconductor dominates the photoresponse.)

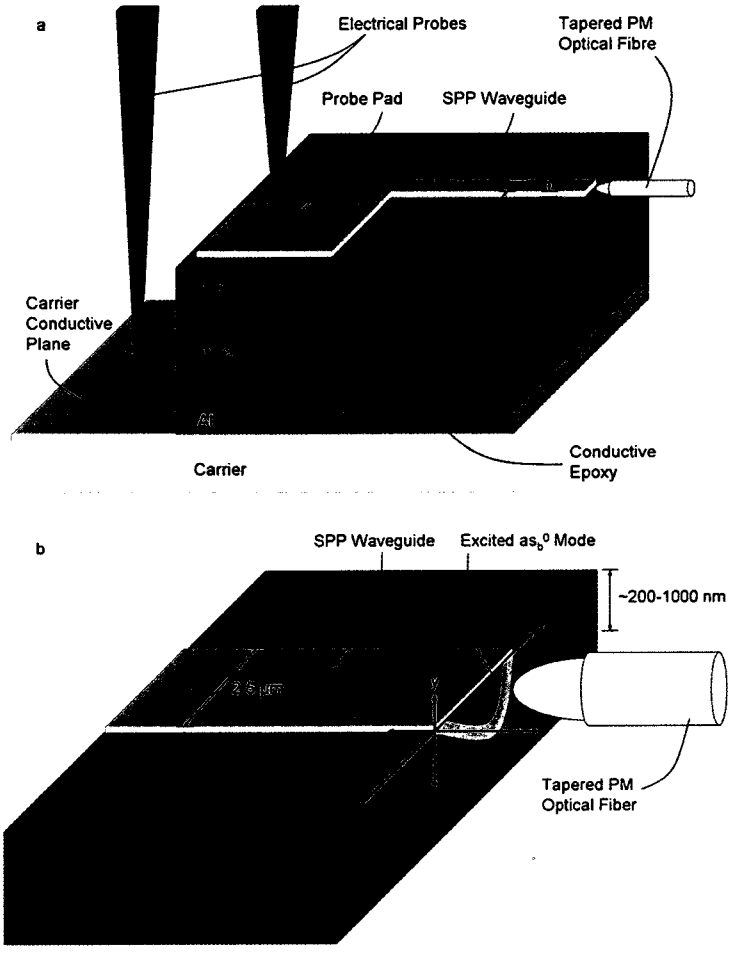

Fig. 1. Sketches of the SPP photodetector. (a) Three dimensional view of the device and experimental setup used to optically and electrically test the device. (b) Close-up view of the alignment of the tapered optical fiber with the SPP waveguide.

The structure is designed to operate in the as_b^0 mode [5, 25], sketched on the face of the structure in Fig. 1(b). This mode is tightly confined and strongly localised to the metal-semiconductor interface. As it propagates, it produces hot electrons in the metal right along the interface, thus enhancing the emission probability over the Schottky barrier.

As sketched in Fig. 1(b), the as_b^0 mode is excited by end-fire coupling with a PM (Polarization-Maintaining) tapered optical fibre. The fibre selected for the experiments has a ~2.5 μm spot size at a free-space optical wavelength of λ_0 = 1550 nm [26]. The coupling efficiency γ_c of this arrangement is estimated by calculating the overlap integral between the fields [27]

$$\gamma_c = \left| \frac{\iint_\infty E_{y1} E_{y2}^* dA}{\sqrt{\iint_\infty E_{y1} E_{y1}^* dA \cdot \iint_\infty E_{y2} E_{y2}^* dA}} \right|^2 \quad (1)$$

where E_{y1} and E_{y2} are the dominant electric field components of the as_b^0 mode and the tapered fibre output beam respectively (the Cartesian coordinate system is sketched on Fig. 1(b)), and ∞ denotes integration over the entire computational domain. The field distribution of the as_b^0 mode is obtained using a commercially available finite element mode solver.

Adopting Au and Al as the metals for the stripe, the as_b^0 mode fields were computed over the wavelength range from 1280 to 1620 nm, interpolating (cubic spline) the optical parameters from refractive index data available at several wavelengths [28]. Fig. 2(a) shows the E_y field distribution of the as_b^0 mode for Au and Al

stripes of $t \sim 135$ nm and $w = 2.5$ μm; these dimensions should produce reasonable coupling efficiencies to the tapered fibre selected. The electric field is dominant in the vertical direction, so the mode is quasi-TM (Transverse Magnetic) in nature, as expected [5]. For both metals, the fields are confined within the first micron below the stripe, with the confinement decreasing with increasing λ_0.

The tapered fibre's spot size also increases with wavelength, being ~10 % larger at $\lambda_0 = 1550$ nm than at 1310 nm [26]. Interpolating the spot size (linearly), we compute the coupling efficiency to the as_b^0 mode over the λ_0 range of interest assuming that the fibre is aligned with the bottom center of the metal stripe. As shown in Fig. 2(b), the coupling efficiency increases with wavelength due to the fields extending over a larger area and providing better overlap with the tapered fibre mode. Although the structure supports many higher order SPP modes [5] only the fundamental as_b^0 mode was found to be excited with relatively high coupling efficiency (up to ~35% for Al at $\lambda_0 = 1620$ nm).

The computed mode power attenuation α of the as_b^0 mode ranges from $\alpha = 1.362$ to 0.505 dB/μm, and $\alpha = 1.204$ to 0.490 dB/μm, as λ_0 goes from 1280 to 1620 nm, for Au and Al respectively. The high attenuation is due to the strong confinement of the mode, and ensures that a short waveguide will absorb essentially all of the in-coupled optical power.

The photodetector responsivity $R = I_{ph}/P_{inc}$ in A/W is expressed by [24, 25]

$$R = \left(1 - e^{-\alpha l}\right)\gamma_c \frac{\eta_i}{h\nu} \tag{2}$$

where I_{ph} is the photocurrent, P_{inc} is the incident optical power, $h\nu$ is in eV, l is the length of the detector, α is the mode power attenuation (in m^{-1}) and η_i is the internal quantum efficiency. For a thick metal stripe ($t >>$ hot electron attenuation length), η_i can be expressed (approximately) as [24]:

$$\eta_i = \frac{1}{2}\left(1 - \sqrt{\frac{\Phi_B}{h\nu}}\right)^2 \tag{3}$$

Using the above, the responsivity can be written in the modified Fowler form (*eg*, [19]):

$$R = \frac{\gamma_c\left(1 - e^{-\alpha l}\right)}{8\Phi_B}\frac{\left(h\nu - \Phi_B\right)^2}{\left(h\nu\right)^2} \tag{4}$$

where, again, $h\nu$ is in eV. The above can be re-written as:

$$\sqrt{R}h\nu = \sqrt{\frac{\gamma_c\left(1 - e^{-\alpha l}\right)}{8\Phi_B}}\left(h\nu - \Phi_B\right) \tag{5}$$

If γ_c is independent of ν, and $\alpha l >> 1$ over ν, then a plot of the left hand side of Eq. (5) versus $h\nu$ is linear with an x-axis intercept of Φ_B and a slope from which γ_c can be deduced. The condition $\alpha l >> 1$ corresponds to the case where essentially all of the optical power coupled into the detector is absorbed.

The reverse bias leakage current (dark current) of the diode is [17]

$$I_{dark} = C_{area}A^{**}T^2 e^{-q\Phi_B/(kT)} \tag{6}$$

where k is Boltzmann's constant, q is the electron charge, T is the absolute temperature, A^{**} is the effective Richardson constant (32 and 112 $Acm^{-2}K^{-2}$ for holes and electrons, respectively [29]), and C_{area} is the Schottky contact area.

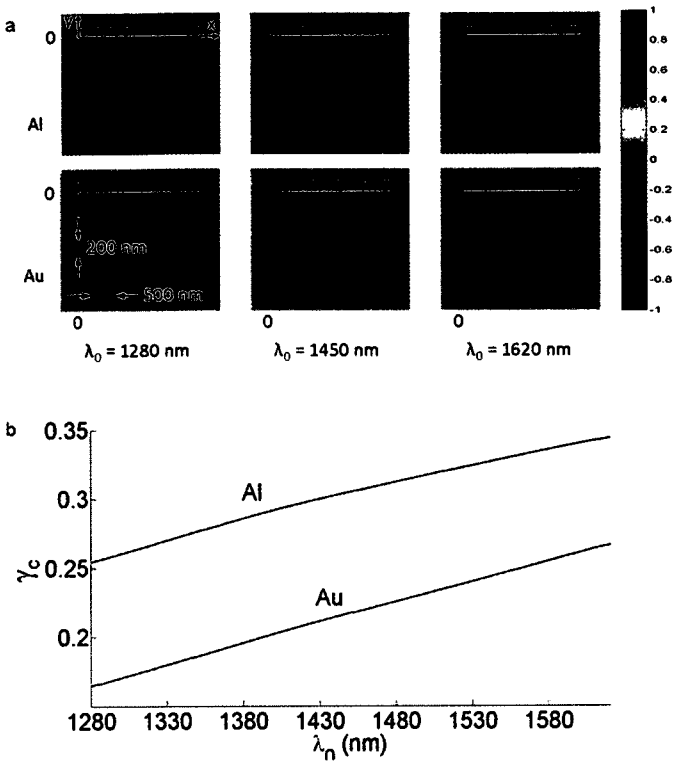

Fig. 2. Theoretical modelling of the SPP waveguide. (a) Re$\{E_y\}$ distribution of the as_b^0 mode for Au and Al metal stripes of w = 2.5 μm and t = 135 nm, at several free-space optical wavelengths. In each case the field is normalised such that $|\mathrm{Re}\{E_y(w/2,0)\}| = 1$. (b) Theoretical coupling efficiencies η_c of the tapered PM optical fibre to the as_b^0 mode for Au and Al stripes on n-Si over the wavelength range of interest.

3. Fabrication and experimental set-up

The photodetectors were fabricated on a Si wafer consisting of a thin (15 μm) lightly n-doped layer (15 Ω-cm) epitaxially grown on a heavily n-doped wafer (0.01 Ω-cm). To create a bottom ohmic contact, a ~0.7 μm thick layer of Al was deposited on the backside, followed by a high temperature anneal. The metal stripes and features were then defined on the wafer's topside using a UV bi-layer liftoff lithography technique [30]. A mask aligner was used to expose the desired pattern on the wafer covered with layers of liftoff resist and photoresist. Immediately prior to top metal deposition, the wafers were placed in a buffered hydrofluoric acid solution to remove any native SiO_2 layer and allow intimate contact between the metal and semiconductor. A thin metal film of $t \sim 135$ nm was deposited in an e-beam evaporation chamber under high vacuum ($< 10^{-6}$ torr). The wafer was singulated into individual dies through careful cleaving. Fig. 3(a) shows a SEM (scanning electron microscope) image of a die with an Al stripe, revealing a flat and smooth end facet suitable for optical coupling. An AFM (atomic force microscope) scan of an Al stripe, shown in Fig. 3(b), verified that the stripe had nearly uniform dimensions t = 135 nm and w = 2.5 μm; its roughness was measured as ~1.5 nm (root-mean-squared). The AFM results for an Au stripe were similar, except that the roughness was larger. Before testing the devices, the dies were cleaned in acetone and isopropyl alcohol, dried with nitrogen, and attached to a conductive carrier plane with conductive epoxy (Fig. 1(a)).

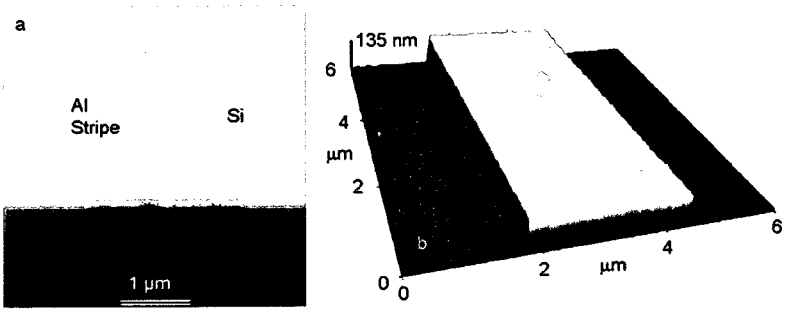

Fig. 3. High resolution microscopy images of the fabricated SPP photodetector. (a) SEM image of the Al on n-Si waveguide showing the Al stripe and a high-quality cleaved end facet. (b) AFM scan of the Al stripe revealing its thickness and width, as well as its high uniformity.

Testing was conducted by placing the die under microscope and using tungsten probes attached to micropositioners to make electrical contact to the device. The bias voltage is applied by probing a large probe pad on top of the device and the ohmic contact on its bottom surface (Fig. 1(a)). Another micropositioner was then used to align the tapered PM fibre (polarisation-aligned to launch TM light) to the waveguide, as per the arrangement shown in Fig. 1. The tapered fibre output field behaves as a focused Gaussian beam, reaching its narrowest spot size at the focal point which is about 14 μm away from the tip. The fibre was aligned to the waveguide by placing the device under reverse bias and maximising the measured photocurrent. As additional evidence of the excitation of the as_b^0 mode, it was observed that nearly no photocurrent was generated when the fibre was rotated to emit TE-polarised (Transverse-Electric) light.

Once the best possible alignment was achieved, a computer-automated routine controlling ancillary instrumentation was run to rapidly execute test routines and gather measurement data. The ancillary instrumentation consisted of two linearly polarised lasers operating near 1310 and 1550 nm each tunable over ~100 nm, a 2×2 fibre coupler with a 50:50 splitting ratio at λ_0 = 1550 nm, an optical power meter, and a multimeter. The two lasers were connected to the coupler's input ports while the output ports were connected to the tapered fibre and the power meter. With the coupler's splitting ratio characterised across the entire λ_0 range, the power meter was used to maintain a constant optical power incident onto the photodetector end facet (P_{inc}) as each laser wavelength was scanned. The multimeter served the dual purpose of applying a voltage bias and measuring the current. All measurements were obtained at room temperature.

4. Experimental results

The electrical performance of several fabricated detectors was determined by measuring the diode current (I) as a function of the applied voltage (V); Fig. 4 shows typical measurements. The detectors show the expected rectifying behaviour, with the slope in the forward bias region limited by the detectors' series resistance (this resistance can be lowered by *eg*, placing ohmic ground contacts along the top surface near the Schottky contact instead of along the bottom). The turn-on voltage for the Au detector is about 0.3 V whereas that of the Al is near 0 V.

The inset of Fig. 4 reveals dark currents of 10 nA and 6 μA, for Au and Al, respectively. These dark currents are rather large because conduction occurs over the entire Schottky contact area, which includes the large probe pad along the top surface (Fig. 1(a)). The contact areas (including the pad) are $C_{area} = 2.71\times10^{-5}$ and 1.0085×10^{-4} cm^2 for the Au and Al detectors, respectively. Isolation of the pads from the Si surface can be achieved by adding a thin intervening dielectric, which would result in a large reduction of the dark current because the pad occupies over 90% of the total contact area.

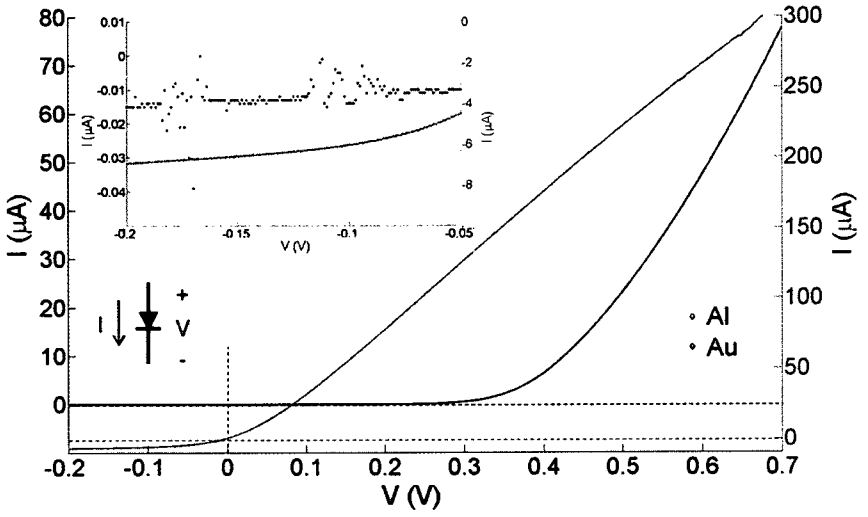

Fig. 4. Measured diode current (I) versus applied voltage (V) of the Al and Au on n-Si SPP detectors. Inset shows a close-up view of the reverse bias region.

Solving Eq. (6) to obtain Φ_B is not very accurate because the experimental setup and the detectors have a high resistance. There are several techniques for extrapolating the barrier height of high resistance diodes, based on forward bias measurements [31]. The methods proposed by Lien et al. [32], and Werner [33] have been shown to yield accurate results. Following the Lien et al. [32] method yields Φ_B = 0.7573 and 0.4447 eV for the Au and Al detectors, respectively, whereas the Werner method yields Φ_B = 0.7444 and 0.4809 eV, respectively. The ideality factors [17] were found to be 1.33 and 1.08, respectively. These Φ_B's differ from the expected values (0.8 and 0.72 for Au and Al respectively [17]); however Φ_B is known to be very sensitive to the method and conditions of contact formation [17]. Given that $h\nu > \Phi_B$ must be satisfied in order for the SPP to be detected, the long-wavelength cut-off of the detectors are $\lambda_0 \sim$ 1650 and 2700 nm, respectively.

The detectors were then characterised optically, first by measuring the diode current I versus P_{inc} under reverse bias at several λ_0. Fig. 5 shows the measurements obtained at a bias of V = -100 mV for the same detectors used in Fig. 4. We emphasise that nearly no photocurrent was generated when the PM tapered fibre was rotated to emit TE-polarised light, so we attribute the photocurrent to the absorption of the SPP mode (as_b^0) as it propagates along the waveguide.

From Fig. 5, it is noted that $-I$ is linear with P_{inc}. Recall that under a weak reverse bias, $-I \cong I_{dark} + I_{ph} = I_{dark} + RP_{inc}$, so the slope of these curves yields the responsivity; they are summarised in Table 1 (under Exp.). In the case of the Au detector, $I_{ph} >> I_{dark} \sim$ 10 nA over most of the measurement range, and R is observed to decrease with increasing wavelength. The longest wavelength tested (λ_0 = 1620 nm) is just above cut-off. In the case of the Al detector, I_{ph} remains only slightly above $I_{dark} \sim$ 6 μA over most of the measurement range (due to power limitations in the lasers used in the set-up and the large dark current of this detector), and R is observed to depend less strongly on wavelength. The responsivity and dark current of the Al detector are larger than those of the Au detector because the Schottky barrier of the former is lower.

Maximum responsivities of 0.38 and 1.04 mA/W are measured for the Au and Al detectors, respectively, at the shortest wavelength, λ_0 = 1280 nm (Table 1). These values are comparable to those reported in Ref. [23] for a $NiSi_2$ on p-Si Schottky barrier detector integrated into a Si on insulator waveguide (4.6 mA/W at $\lambda_0 \sim$ 1550 nm).

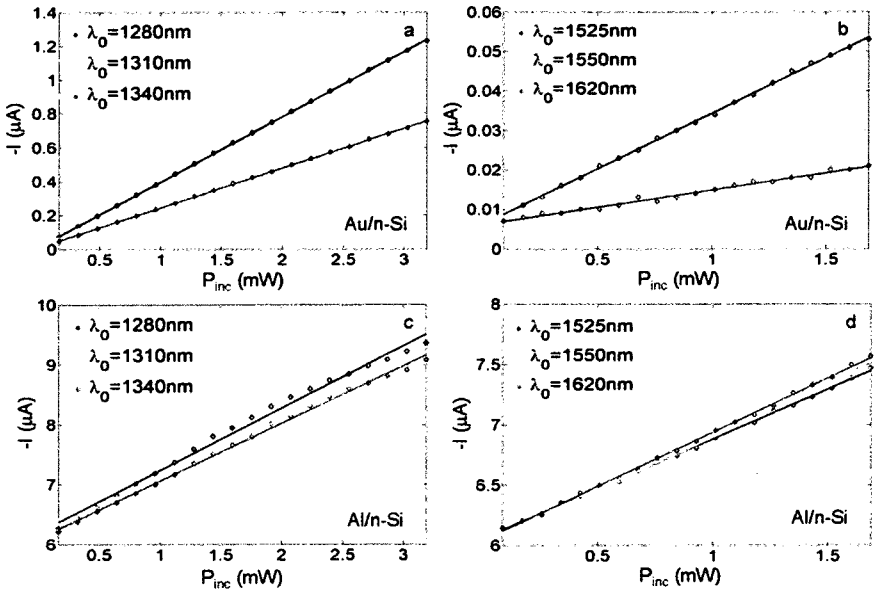

Fig. 5. Measured diode current ($-I$) of SPP detectors as a function of incident optical power (P_{inc}) at several λ_0's at a bias of V = -100 mV; (a, b) Au on n-Si, (c, d) Al on n-Si.

The wavelength response of the detectors was then measured at a constant P_{inc} = 2 mW and at a bias of V = -100 mV; Figs. 6(a) and 6(c) give the measurements. (The wavelength ranges investigated are dictated by the tunable lasers available.) The measurements of the Al detector (Fig. 6(c)) for $\lambda_0 \sim 1550$ nm are noisier (and less reliable) than those of the Au detector (Fig. 6(a)), again because I_{dark} is larger for the former.

Figs. 6(b) and 6(d) plot the corresponding $R^{1/2}h\nu$ versus $h\nu$ (such plots are termed Fowler plots - *eg* [34]). The measurements approximately follow linear models (the best fitting ones are shown), except for the Al detector at $\lambda_0 \sim 1550$ nm (Fig. 6(d)) because I_{dark} is large. As pointed out following Eq. (5), if γ_c is independent of ν, and $\alpha l >> 1$ over the range of ν considered, then the plot is linear with an x-axis intercept of Φ_B and a slope from which γ_c can be deduced. The condition $\alpha l >> 1$ is essentially satisfied for the detectors characterised given their length (l = 80 and 35 μm for Au and Al) and attenuation (see Section 2); $\alpha l > 4$ over the wavelength range of interest for both. However, γ_c depends on ν as shown by the computations of Fig. 2(b), explaining the observed slight deviation from linearity (especially in the better quality measurements of Fig. 6(b)).

The x-axis intercepts of the linear models on the Fowler plots yield Φ_B = 0.765 and 0.494 eV for the Au and Al detectors, respectively; these values are in good agreement with those obtained from I-V measurements. From the slope of the linear models, we find γ_c = 3.85% and 2.01% for the Au and Al detectors, respectively. These coupling efficiencies are lower than those estimated theoretically (Fig. 2(b)). Part of the discrepancy is attributable to alignment difficulties (the as_b^0 mode fields extend to <1 μm vertically - Fig. 2(a)), and part is attributable to a simplified theory (the coupling calculations neglect possible beam curvature at the detector end facet, and the expression for η_i, Eq. (3), neglects the attenuation length of hot carriers).

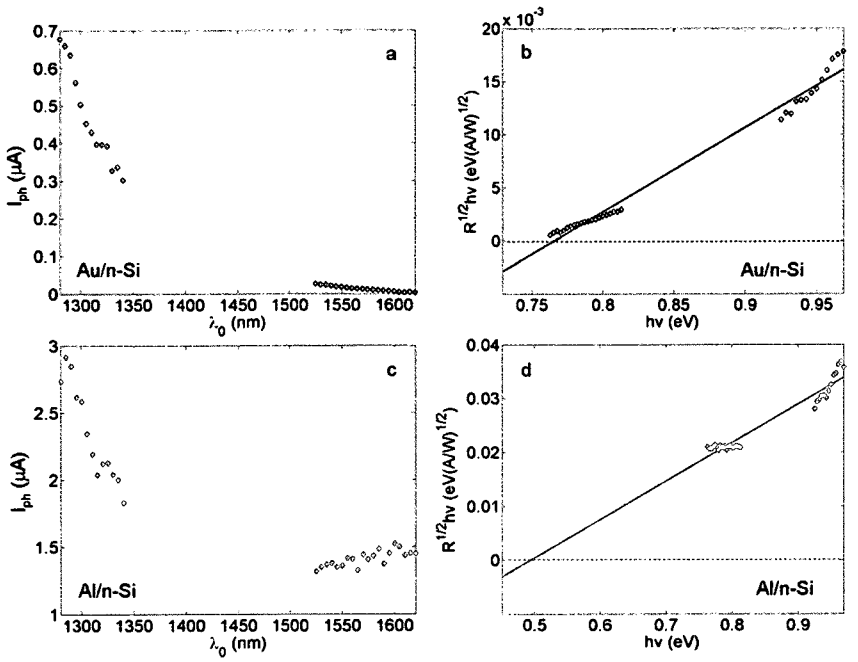

Fig. 6. (a) Measured photocurrent (I_{ph}) of a Au on n-Si SPP detector as a function of λ_0 for P_{inc} = 2 mW and a bias of V = -100 mV; (c) corresponding measurement for the Al on n-Si detector. (b, d) Corresponding Fowler plots.

Finally, the measured responsivities are compared with theoretical ones computed via Eqs. (2) and (3) using experimental values for γ_c and Φ_B, and the computed values for α given in Section 2. The theoretical results are summarized in Table 1 (under Theo.). Considering that several values were obtained for Φ_B, and that γ_c was estimated from the slope of the Fowler plot, these parameters were adjusted slightly to provide the best agreement between the experimental and theoretical responsivities: Φ_B was taken as 0.744 and 0.484 eV for the Au and Al detectors respectively, and γ_c was taken as 4.3% and 2.5 %, respectively (all are close to the measured values). Average errors of 33.9% and 8.8 % are obtained for the Au on n-Si and Al on n-Si detectors, respectively. The agreement is better at the shorter wavelengths (λ_0 ~ 1310 nm) than at the longer ones (λ_0 ~ 1550 nm).

Table 1. Experimental and theoretical responsivities in mA/W of Au on n-Si and Al on n-Si SPP detectors at a bias voltage of V = -100 mV.

λ_0 (nm)	Au/n-Si			Al/n-Si		
	Exp.	Theo.	% Error	Exp.	Theo.	% Error
1280	0.3848	0.341	11.4	1.0401	1.1014	-5.9
1310	0.3021	0.2937	2.8	0.9725	1.0564	-8.6
1340	0.2338	0.2493	6.6	0.9611	1.0083	-4.9
1525	0.028	0.05	78.6	0.8235	0.7047	14.4
1550	0.0204	0.0341	67.2	0.8397	0.6656	20.7
1620	0.0087	0.0055	36.8	0.896	0.5639	37.1

5. Summary and concluding remarks

In summary, SPP Schottky contact detectors were fabricated on n-Si, characterised, and compared to theoretical predictions. An asymmetric metal stripe waveguide was designed to operate in a strongly confined SPP mode localised at the metal - Si interface (the as_b^0 mode). The mode propagates with a high attenuation of 1.362 and 1.204 dB/μm for Au and Al on n-Si, respectively, so the detectors are very short in length, 80 and 35 μm, respectively, for complete absorption of the coupled optical power. Respective dark currents of 10 nA and 6 μA were measured, which can be reduced by isolating the device probe pads from the Schottky contact plane.

Responsivities of 0.38 and 1.04 mA/W were measured for Au and Al on n-Si respectively, at λ_0 = 1280 nm. These values are lower than theoretically possible, partly because the SPP mode was excited low coupling efficiency. The fabricated detectors have been successfully demonstrated across a significant portion of the infrared spectrum. The detectors can be integrated with other structures used in plasmonics or silicon-based photonics, and hold promise for short-reach optical interconnects and power monitoring applications.

Acknowledgements

The authors thank Rob Vandusen and Carol Adams for numerous comments and insight provided during fabrication. The input and help of Ewa Lisicka-Skrzek during the measurements is also gratefully acknowledged.

4.2 Detailed fabrication procedure of asymmetrically clad SPP waveguides

The photodetectors were fabricated using UV lift-off lithography technology [1], with the process outline for membrane waveguide fabrication [2] slightly modified to fabricate the structures. The fabrication steps are outlined in Table 4-1, while the process details are described more thoroughly as follows. Heavily doped silicon wafers with a lightly doped layer present on the top were first put through an RCA cleaning process [1] to remove any residue particles and oxide layers. The wafers were then placed in a high vacuum electron beam metal evaporation chamber, where a 0.7 μm layer of aluminum was deposited on the backside of the wafers. A 10 mins rinse with light agitation in deionised (DI) water was then applied to remove any potential residues deposited on the wafer's frontside. To ensure an ohmic contact is formed between the aluminum and the heavily doped silicon interface, the wafers were then placed in a high temperature anneal oven (400 °C in H_2 for 10 mins). They were then blown dry using a nitrogen gun and placed in a vacuum oven (200 °C for 30 mins) to remove any water from the surface. Successive layers of hexamethyl disiloxare (HMDS), lift-off resist [3], and positive photoresist [4], were then deposited through spin coating (1000 rpm for 10 s, followed by 4000 rpm for 30 s) and soft baking (110 °C for 60 s) each layer, respectively. The wafers were then aligned with a chrome mask and exposed with UV light in a Karl-Suss MA6 mask aligner, then placed in a developer solution [5] for 45 s to remove the photoresist in the areas to be patterned with metal, followed by 15 s and 60 s rinses in separate DI water beakers. After blow drying the water off the wafers, they were then placed in a O_2 plasma etcher for 45 s at 100 W power and 0.3 Torr O_2 pressure; this descum process removed the photoresist and HMDS in the areas that were previously developed. Afterwards,

Step	Details
RCA clean	As outlined in [1]
Backside metal evaporation	Deposition of 0.7 μm of Al on wafer backside through e-beam evaporation under high vacuum.
Rinse	10 min static rinse in DI water; followed by N_2 blow dry
Anneal	10 min anneal in H_2 gas at 400 °C
Pre spin-coating heat treatment	200 °C for 30 min
HMDS spin-coating	1000 rpm for 10 s, followed by 4000 rpm for 30 s
Soft bake	110 °C for 60 s
Lift-off resist [3] spin-coating	1000 rpm for 10 s, followed by 4000 rpm for 30 s
Soft bake	110 °C for 60 s
Photo-resist [4] spin-coating	1000 rpm for 10 s, followed by 4000 rpm for 30 s
Alignment	Alignment of wafer under chrome mask using a Karl-Suss MA6 mask aligner
Exposure	7 s exposure to UV light through mask
Development	45 s static dip in developer solution [5]; 15 and 60 s static dips in separate DI water bath; N_2 blow dry
Descum	100 W power and 0.3 Torr O_2 pressure in plasma etcher
BHF dip	45 s static dip in BHF solution; 2 min dip in DI water; N_2 blow dry; immediate placement in high vacuum metal evaporation chamber
Metal Evaporation	Deposition of 100 nm of metal on wafer front side through e-beam evaporation under high vacuum.
Lift-off	2 successive baths in lift-off solution [6] held at 80 °C, for 20 min, with 10 s ultrasonic treatment for each
Clean	10 min dip in acetone; 10 min dip in isopropyl alcohol; 10 min dip in DI water; N_2 blow dry

Table 4-1: Schottky SPP detector fabrication steps.

the wafers were placed in a buffered HF (BHF) acid solution to remove any native oxide layer present at the silicon interface, then rinse for 2 min in DI water and blown dry. Immediately afterwards, the wafers were placed in the e-beam evaporation chamber under high vacuum where the desired thickness and type of metal was evaporated onto the wafers for the Schottky metal contacts on the top of the wafers. The pre-evaporation BHF treatment allowed intimate Schottky contact between the silicon and metal by minimizing the presence of naturally growing insulating SiO_2 layer. Finally the wafers were placed in two successive baths of lift-off removal solution [6] for 20 min each followed by a 10 s ultrasonic treatment

after each bath. This removed the lift-off resist on undeveloped areas of the wafer, leaving only the metal layer in the area defined by the lithography mask. To remove any unwanted particles or residue, the wafers were placed in acetone, isopropyl alcohol, and DI water for 10 min in each bath.

The end result of the fabrication process were wafers with top metal Schottky contact metal of ~100 nm thickness and pattern defined by the lithography mask, with an aluminum ohmic contact at the bottom of the wafer. Figure 4-1 shows a microscope image of a small section of the wafer. The cleave mark is used as a reference point to delineate the area occupied by each die, and thus serve as a reference point for cleaving the wafer. Therefore, a perfect cleave will result in several waveguides of different lengths starting at both dies at either side of the cleave facet. Figure 4-2(a) and 4-2(b) show a scanning electron microscope (SEM) images of a Al and Au waveguides taken along the cleaved interface. The image reveals the very smooth interface resulting from the cleave, which is desired for efficient coupling of light from the end facet into the photodetector. Figure 4-3(a) and 4-3(b) show microscope images of the waveguide and electrical contact pad for Al and Au waveguides respectively. Figure 4-4(a) and 4-4(b) show atomic force microscopy (AFM) images of the Al and Au waveguides respectively. The AFM scans provide a good evaluation of the width and thickness of the metal waveguides, as well as

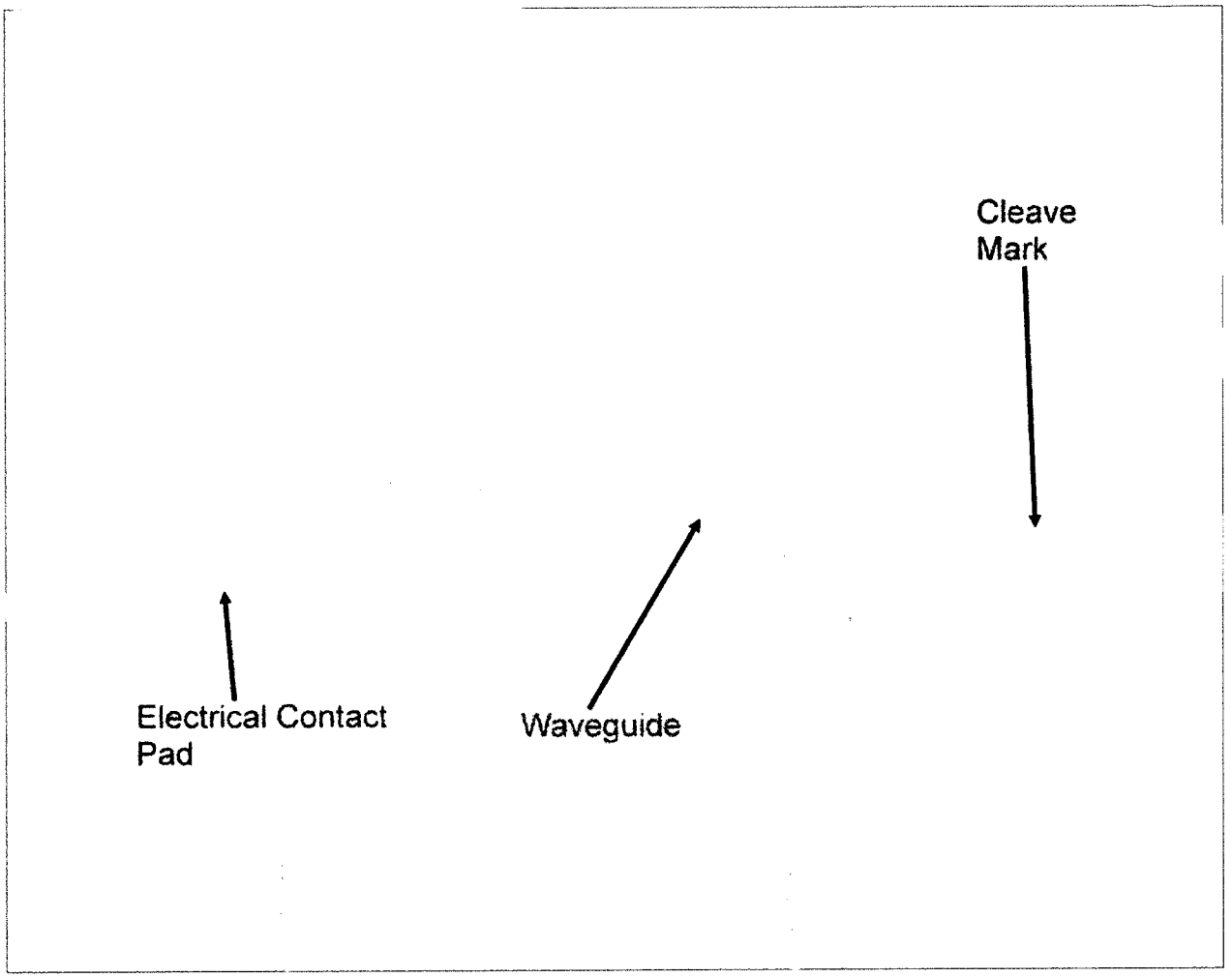

Figure 4-1: Microscope image of a section of Si wafer patterned with Al features.

the roughness of the deposited metal film. The target metal width of 2.5 μm was accurately achieved and reveals the successful implementation of the lithography process. The metal thickness is 141 and 135 nm for Au and Al, respectively, which is somewhat off the 100 nm target, but doesn't effect the photodetector performance much since numerical analysis of the fundamental SPP mode reveal its properties don't change much for metal stripe thicknesses larger than 80 nm. The surface roughness analysis of the metal films reveals that the Au film is rough, with an rms roughness of 12.2 nm, and the thickness reaching 200 nm in some

points. The Al film is much smoother, with an rms roughness of 1.5 nm. Electron beam evaporation of Au typically results in a grainy and rough film, but the lack of good calibration and optimization of the evaporator's control parameters has resulted in a very rough Au surface; again, this will not have any noticeable effect on the performance of the photodetector since the fundamental SPP mode is mainly confined to the bottom metal-silicon interface.

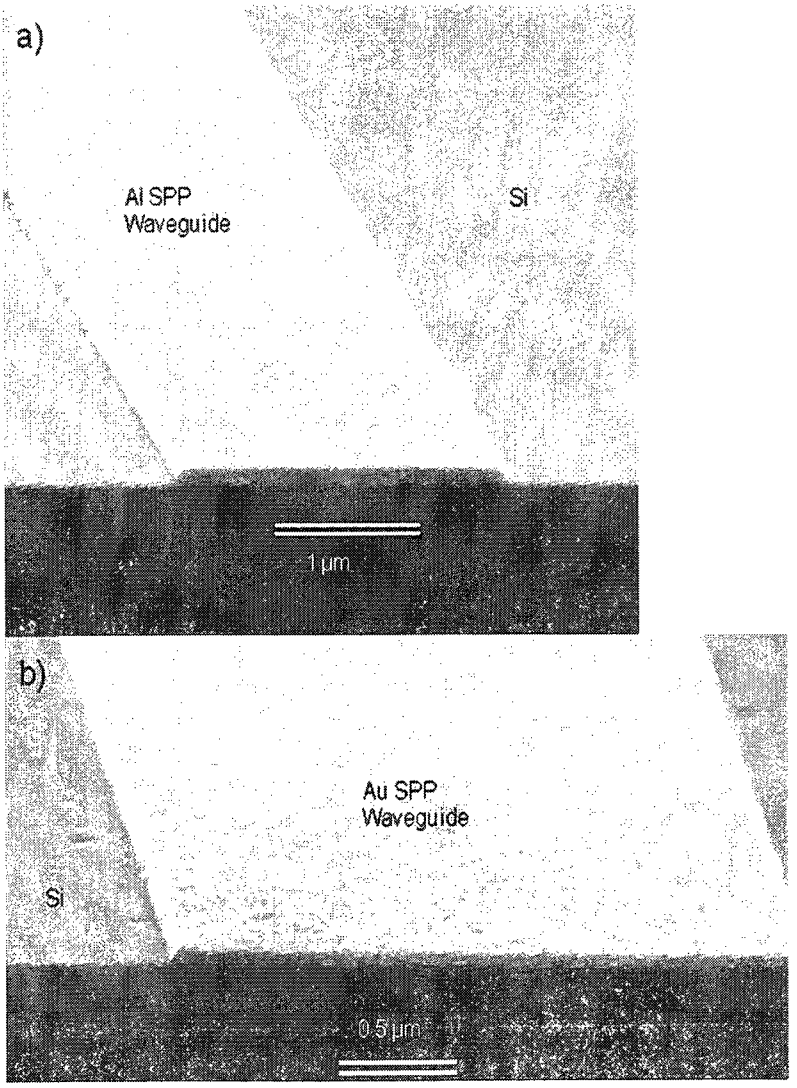

Figure 4-2: SEM image of Al (a) and Au (b) waveguides.

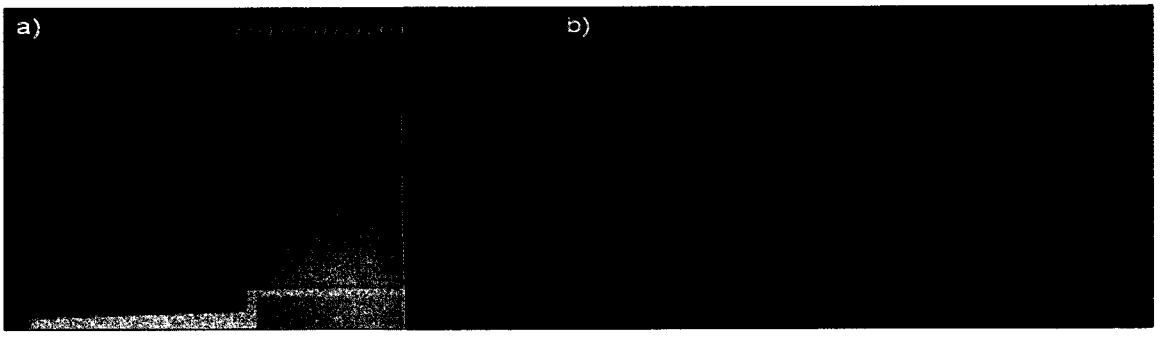

Figure 4-3: Microscope image of Al (a) and Au (b) waveguides.

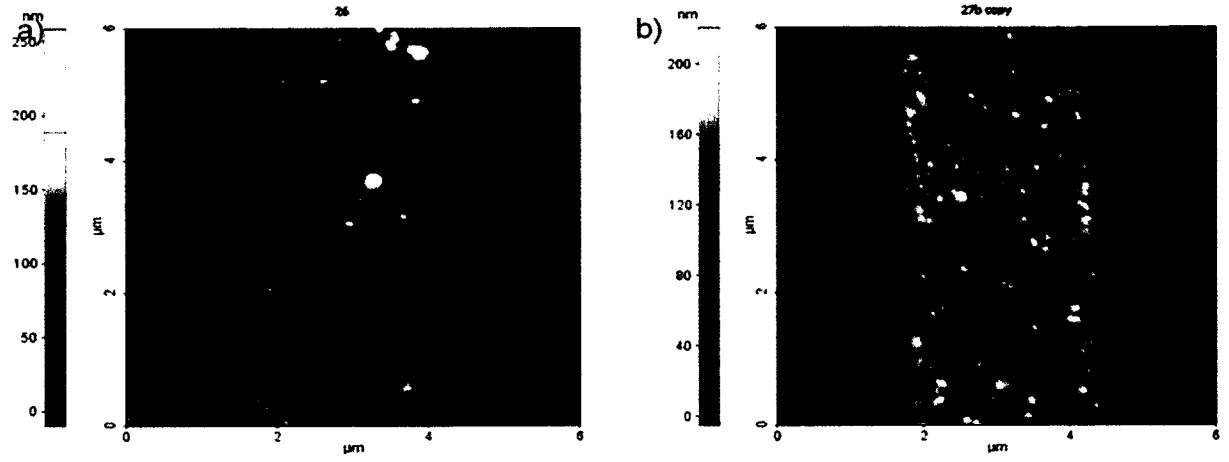

Figure 4-4: AFM scans of Al (a) and Au (b) waveguides.

4.3 Additional figures for experimental measurements

The results and discussion of the measurements made on the fabricated SPP detectors are discussed in the paper included in this chapter. However, not all the figures describing the measurements are included in that paper. Included in this appendix section are Figures 4-5 and 4-6, which show current versus incident optical power measurements of the Au/n-Si and Al/n-Si devices respectively (having metal stripe thickness ~ 135 nm and width of 2.5 μm), at reverse biases of 0.1, 0.15, and 0.2 V, and wavelengths of 1280, 1310, 1340, 1525, 1550, and 1620 nm. As shown in the figures, the responsivity (i.e. the slope of the current versus power line) of the device increases at shorter wavelengths and larger reverse bias; the former due to the increase internal quantum efficiency of a charge carrier excited by a higher energy photon, and the latter due to the slight lowering of the Schottky barrier height due to the image force lowering effect [1]. Figure 4-7 shows the responsivity of the detector as a function of wavelength, as well as the theoretical curves. The discrepancy between experimental and theoretical data at some wavelengths can be noticed. Additionally, the current versus forward bias voltage analysis techniques used to derive the Schottky barrier height also gave estimates of the device resistance. These were found to be 2.980 and 1.786 kΩ for Au/n-Si and Al/n-Si respectively.

Figure 4-8 shows the current versus voltage measurements of an Au/p-Si device (stripe thickness ~ 135 nm and width of 2.5 μm). As expected, the diode barely shows any rectifying behavior at all, due to the low barrier height for this metal semiconductor combination. Implementation of the barrier height evaluation techniques described in the paper in this chapter reveal the barrier height to be 0.3557 and 0.3480 eV with the Werner

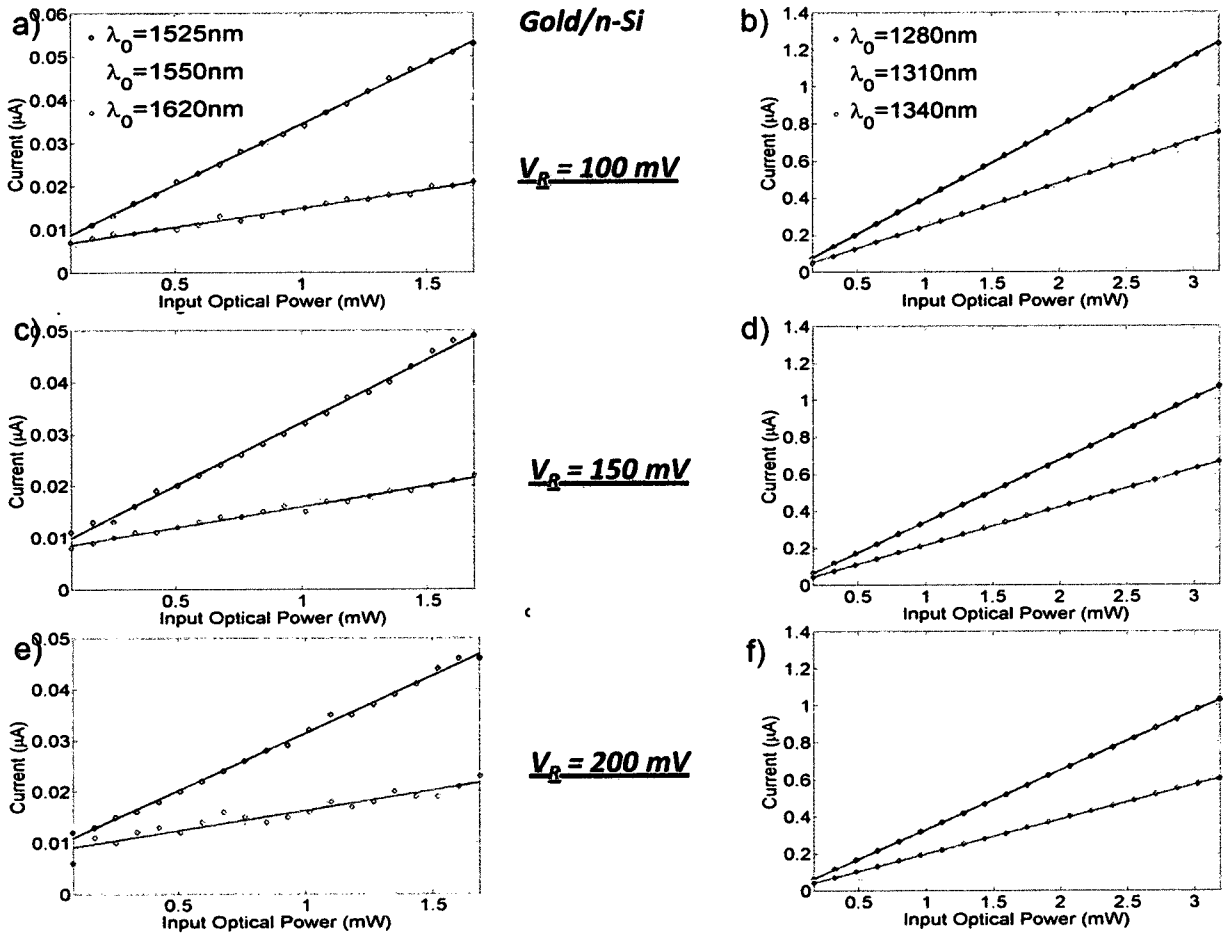

Figure 4-5: Current versus power measurements of Au/n-Si Schottky photodetector for (a) V_R = 0.1 V and λ_0 = 1525 – 1620 nm; (b) V_R = 0.1 V and λ_0 = 1280 – 1340 nm; (c) V_R = 0.15 V and λ_0 = 1525 – 1620 nm; (d) V_R = 0.15 V and λ_0 = 1280 – 1340 nm; (e) V_R = 0.2 V and λ_0 = 1525 – 1620 nm; (f) V_R = 0.2 V and λ_0 = 1280 – 1340 nm.

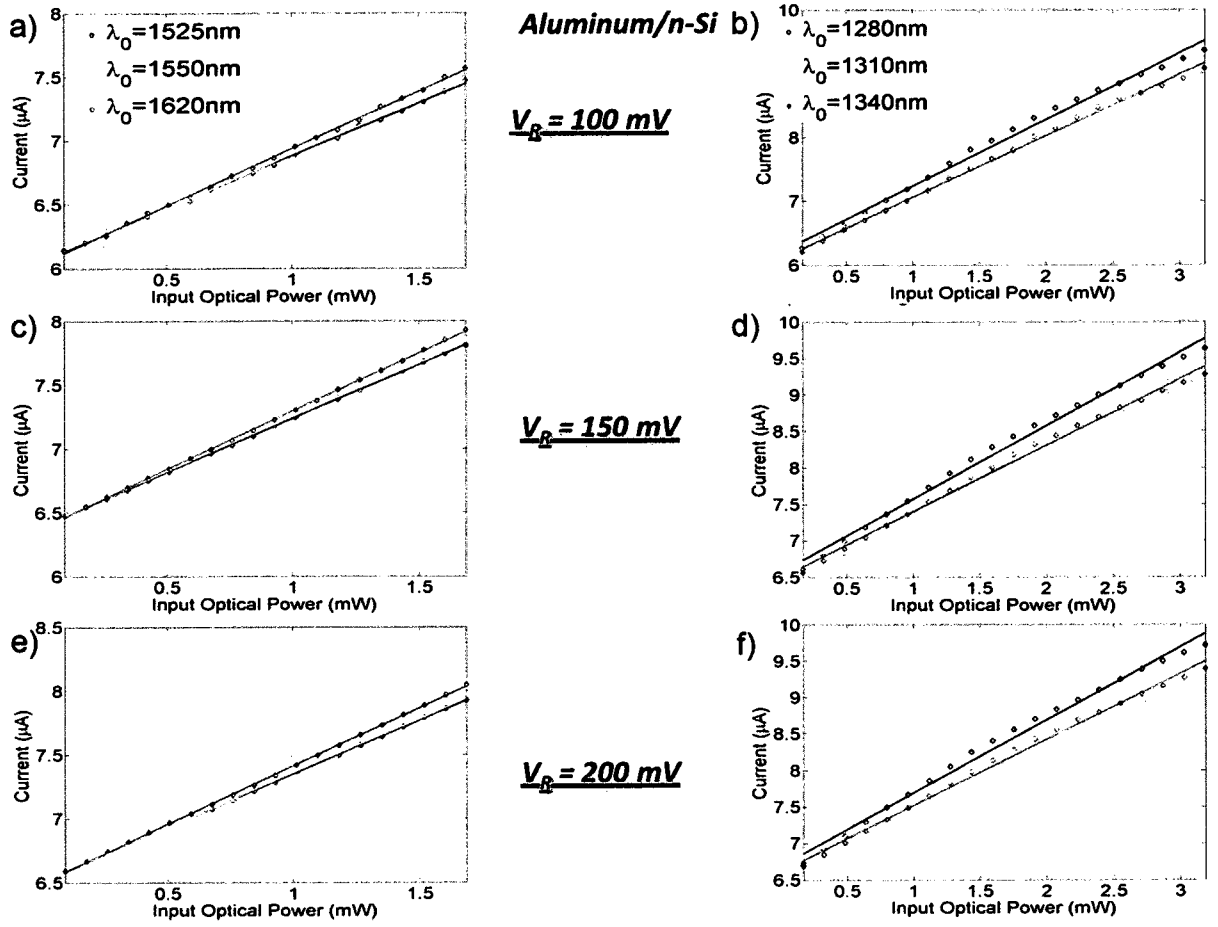

Figure 4-6: Current versus power measurements of Al/n-Si Schottky photodetector for (a) V_R = 0.1 V and λ_0 = 1525 – 1620 nm; (b) V_R = 0.1 V and λ_0 = 1280 – 1340 nm; (c) V_R = 0.15 V and λ_0 = 1525 – 1620 nm; (d) V_R = 0.15 V and λ_0 = 1280 – 1340 nm; (e) V_R = 0.2 V and λ_0 = 1525 – 1620 nm; (f) V_R = 0.2 V and λ_0 = 1280 – 1340 nm.

and Lien et al. methods respectively; the series resistance was estimated at 102 Ω for Au/p-Si. Figure 4-9 shows the diode's total current (photocurrent + dark current) as a function of wavelength, with the theoretical fit to the data (barrier height of 0.34685 eV assumed for this plot). The fit between experimental and theoretical data is very bad in this case, with the theoretical data not following the same trend as experimental data. Nonetheless, a coupling efficiency of 1.92% was estimated based on the best possible fit shown in the figure.

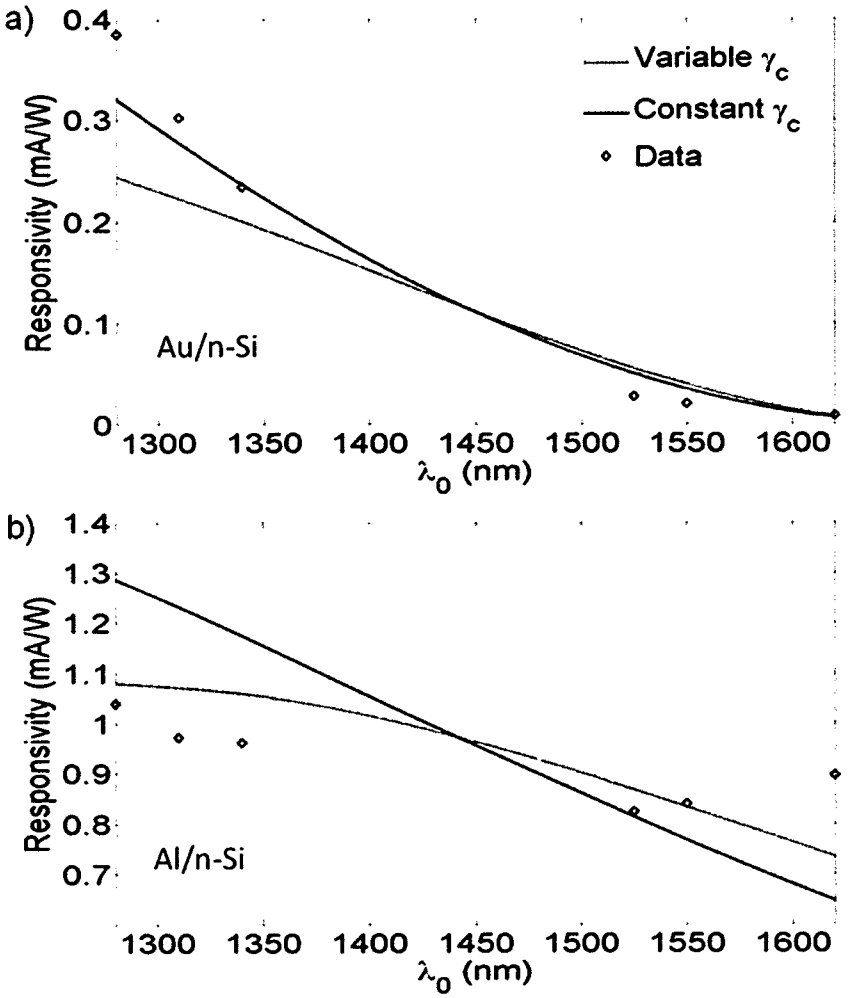

Figure 4-7: Responsivity versus wavelength measurements of Schottky photodetector with (a) Au/n-Si; (b) Al/n-Si.

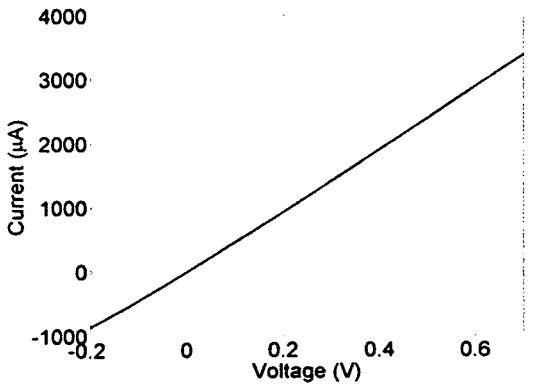

Figure 4-8: Current versus voltage measurements of Au/p-Si Schottky diode.

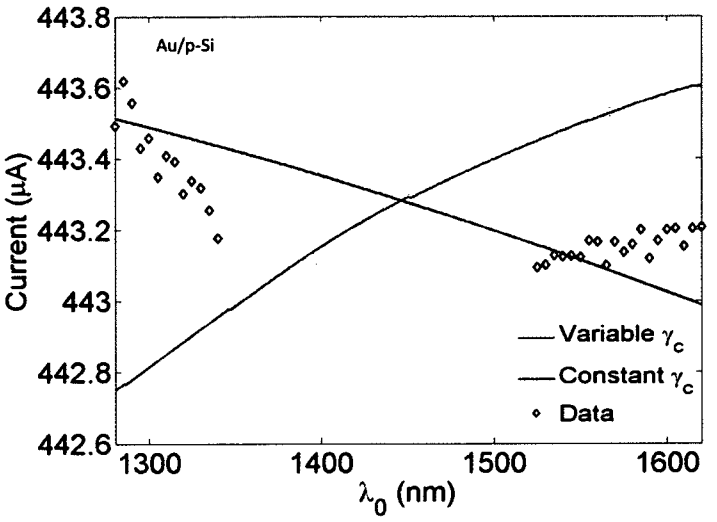

Figure 4-9: Current versus wavelength measurements of Au/p-Si Schottky photodetector.

Current versus incident optical power measurements of the Au/p-Si detector, in Figure 4-10, show the device's responsivity at multiple wavelengths and reverse bias voltages. Comparison between experimental and theoretical data for a 0.1 V reverse bias is shown in Table 4-1. The device does not perform very well, and matches poorly to theory, this is partly due to the very low barrier height of the device, which makes it very susceptible to noise degradation.

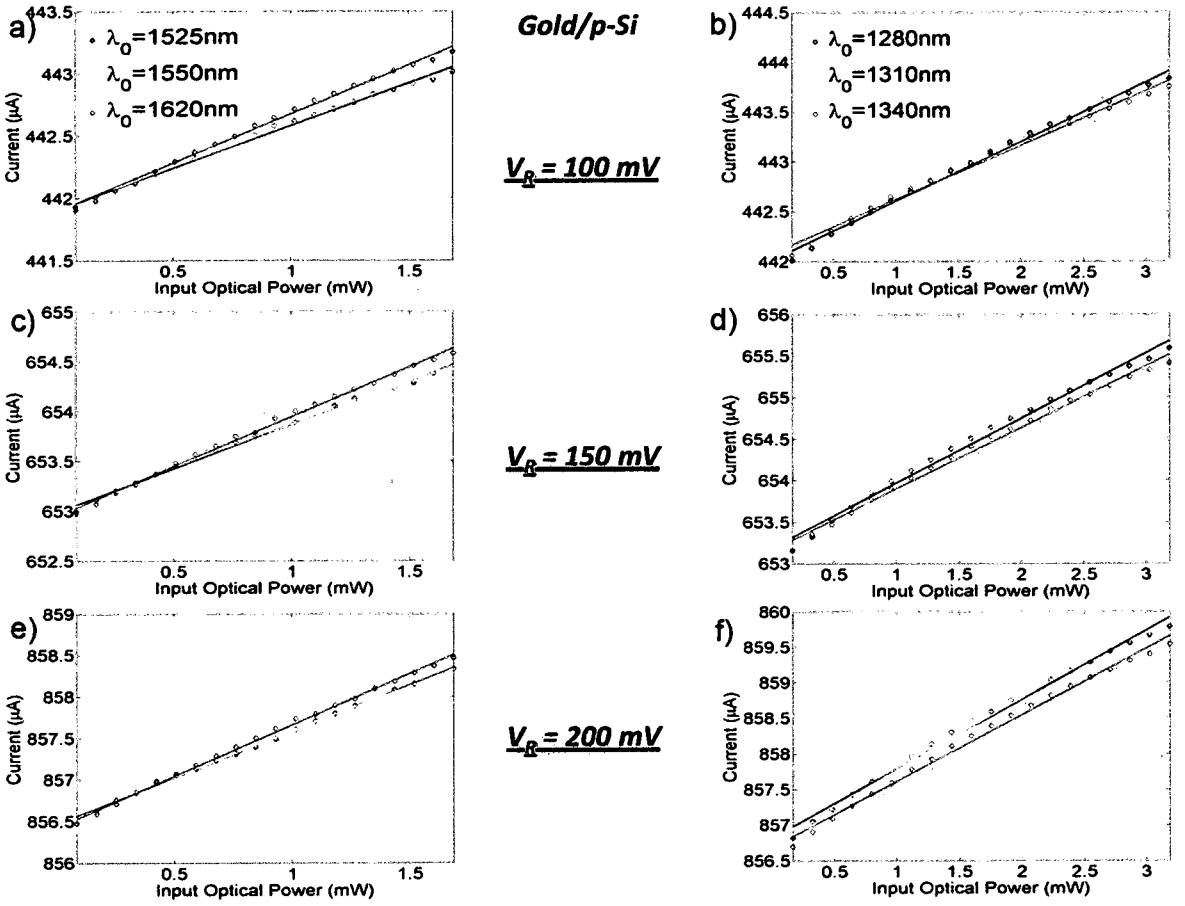

Figure 4-10: Current versus power measurements of Au/p-Si Schottky photodetector for (a) $V_R = 0.1$ V and $\lambda_0 = 1525 - 1620$ nm; (b) $V_R = 0.1$ V and $\lambda_0 = 1280 - 1340$ nm; (c) $V_R = 0.15$ V and $\lambda_0 = 1525 - 1620$ nm; (d) $V_R = 0.15$ V and $\lambda_0 = 1280 - 1340$ nm; (e) $V_R = 0.2$ V and $\lambda_0 = 1525 - 1620$ nm; (f) $V_R = 0.2$ V and $\lambda_0 = 1280 - 1340$ nm.

	Responsivity of Au/p-Si photodetector (mA/W)	
λ_0 (nm)	**Experimental Data**	**Theoretical Data**
1280	0.5955	1.6002
1310	0.6217	1.5814
1340	0.5448	1.5616
1525	0.6825	1.4215
1550	0.6855	1.4002
1620	0.7864	1.3371

Table 4-1: Responsivity of Au/p-Si photodetector (mA/W) at 0.1 V reverse bias.

4.4 References

[1] M. J. Madou, *Fundamentals of Microfabrication: The Science of Miniaturization* (Taylor and Francis, 2002).

[2] P. Berini, N. Lahoud, and R. Charbonneau, "Fabrication of surface Plasmon waveguides and integrated components on ultra-thin free-standing membranes," *Journal of Vacuum Science and Technology A – Vacuum, Surfaces, and Films*, vol. 26, pp. 1383-1391, 2008.

[3] MicroChem, Lift Off Resist (LOR 1A) (www.microchem.com).

[4] Shipley, Positive Photoresist (S1805) (www.rohmhaas.com).

[5] Shipley, Photoresist Developer Solution (MF-321) (www.rohmhaas.com).

[6] Microposit 1165 lift-off solution.

Chapter 5

Conclusion

5.1 Thesis contributions

Bound SPP modes supported by thin Au and Al stripes of finite width residing on silicon, and covered by air, were studied and described. The first three lowest order bound modes supported by the waveguides were studied across a large thickness and width range, at multiple wavelengths. The evolution of real part of effective index and mode power attenuation with metal stripe width and thickness was described and interpreted. Theoretical and experimental investigations of end fire coupling into the SPP waveguide with a PM tapered fiber were made for all the design space studied. Waveguide designs were proposed to only excite the fundamental mode with optimal coupling efficiency. Alternative designs primarly exciting the second order horizontally symmetric mode were also made, albeit the lower coupling efficiency results in poorer performance. The best designs for device responsivity, dark current, and minimum detectable power, were proposed, along with theoretical predictions for each design.

Several combinations of the proposed designs were fabricated using a lithography process in a clean room laboratory. Several of the fabricated photodetectors were then cleaved and prepared for experimental measurements. A complex experimental setup was devised and implemented to evaluate the performance of the fabricated photodetectors in the infrared

1280-1620 nm wavelength range. Experimental responsivities of 1.0401 and 0.3848 mA/W for Al/n-Si and Au/n-Si detectors respectively, were reported.

The proposed surface plasmon detector integrated into an asymmetric metal stripe was demonstrated to operate successfully, and strong evidence of surface plasmon excitation was shown. Additional fabricated structures provide a wealth of devices for further experimentation in the future. The device has promise for low cost application in optical interconnects, integrated optics, and silicon photonic circuits.

5.2 Suggestions for future work

Further experimental measurements are needed to fully characterize the detector and the excited SPP mode propagation characteristics. A more complex experimental setup where the SPP mode is excited with higher coupling efficiency could allow to better compare the measurements to the theoretical model. The theory of multiple hot carrier reflections for a thin metal film can also be verified by making measurements on devices with lower thickness. Integration of the device in a low cost optical interconnect application would further help to evaluate the device's suitability and advantages for such applications. In addition, the device's time response could be measured to further evaluate its suitability in a short-range high-speed communication link.

Experimental measurements on the photodetector employing the long-ranging SPP mode could allow better performance and potentially verify the theoretical model for multiple carrier reflections for a thin metal film. The performance of this detector could potentially be enhanced by adiabatically increasing the metal stripe's width, to increase attenuation of the long-range SPP mode and therefore also reduce the size of the device.

Appendix A

Characterization of Long-ranging Surface-plasmon Polariton (LRSPP) Waveguides

As an initial exercise to better understand the behavior of SPP modes and to gain expertise on optical measurements of micron scale devices, a SPP waveguide supporting the LRSPP mode was experimentally tested and characterized. Samples from a wafer internally identified as X0146053 were used. The devices tested on these samples consisted of a lower cladding of sputtered SiO_2, an adhesion promoting 1 nm thick layer of Mo, an 8 μm wide and 18 nm thick Au stripe, and a sputtered SiO_2 upper cladding. Straight waveguides running from one facet of the die to the other were tested. The measurements consisted of aligning a TM polarized polarization maintaining (Panda) single mode fiber at one facet of the die (through end-fire coupling) and using a lens and an infra-red camera to view the mode output at the other facet of the die. Figure A-1 shows the mode output captured by the IR camera. The highly focused round spot is the output of LRSPP waveguide, while surrounding scattered light consists of light from the fiber that wasn't coupled into the SPP waveguide as well as light scattered by irregularities in the metal stripe and the cladding area. It is also noticed that the scattered light is confined mainly to a finite cross sectional area; this is because the air/SiO_2/Si sandwich acts a rib waveguide and the output consist of the superposition

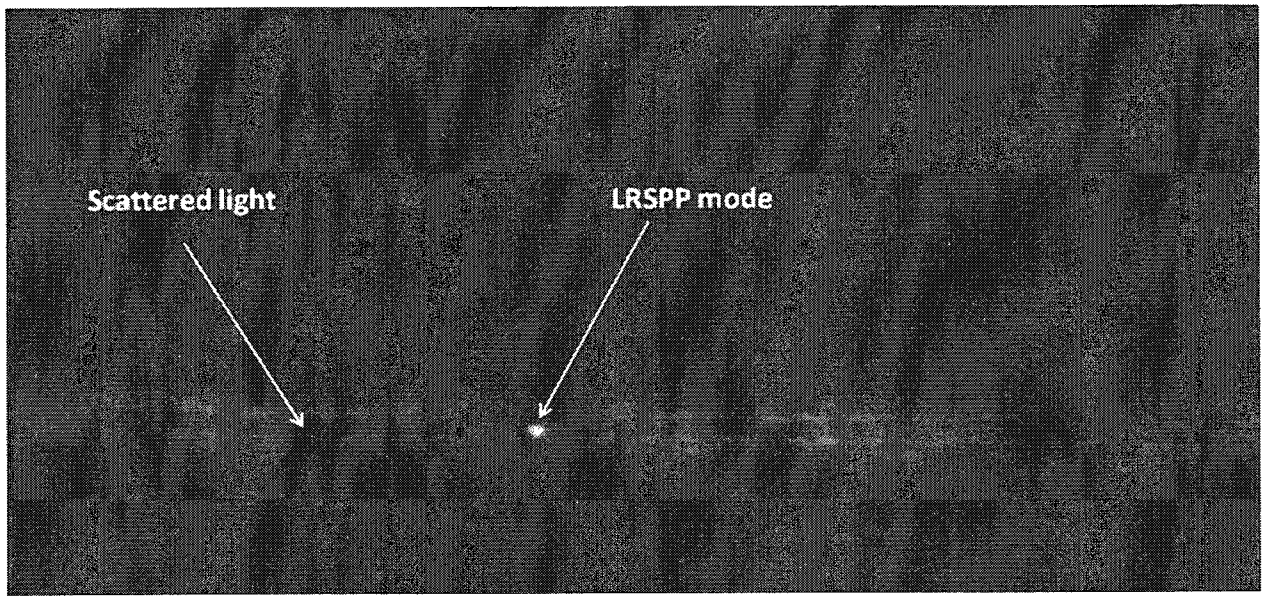

Figure A-1: Mode output of a LRSPP waveguide captured by an IR camera.

of the box modes supported by the geometry. The thickness over which the scattered light is visible is therefore a good estimate of the thickness of the SiO_2 cladding.

With the best possible alignment achieved through the visible increase in mode intensity and reduction in scattered light intensity (less scattered light means more light coupled into LRSPP mode), the lens at the output of the waveguide was replaced by another single mode fiber which was connected to an optical power meter. This fiber was aligned by maximizing the power coupled (power level read at power meter) into it. Finally, the alignment of both fibers was adjusted to maximize the amount of power transmitted through the waveguide from one fiber to another. The difference between the incident power at the input of the waveguide and the output power of the waveguide consists of the sum of the total coupling loss and the propagation loss. This difference was measured at a free-space optical wavelength of 1310 nm for several waveguides of different length and is summarized in Table A-1. The measurements for each

Die Length (mm)	Output Power (dBm)	Input Power (dBm)	Total Loss (dB)	Wavelength (nm)
2.34	-10.9	3.2	-14.1	1310
2.34	-11.5	3.2	-14.7	1310
2.34	-11	3.2	-14.2	1310
4.58	-17.5	3.2	-20.7	1310
4.58	-18.2	3.2	-21.4	1310
5.5	-20.5	3.2	-23.7	1310
5.5	-22.1	3.2	-25.3	1310
5.5	-20.4	3.2	-23.6	1310
7.06	-30.2	3.2	-33.4	1310
7.06	-30.9	3.2	-34.1	1310

Table A-1: Total loss measurements of LRSPP waveguides of different lengths 8 μm wide and 18 nm thick Au stripe cladded by SiO_2.

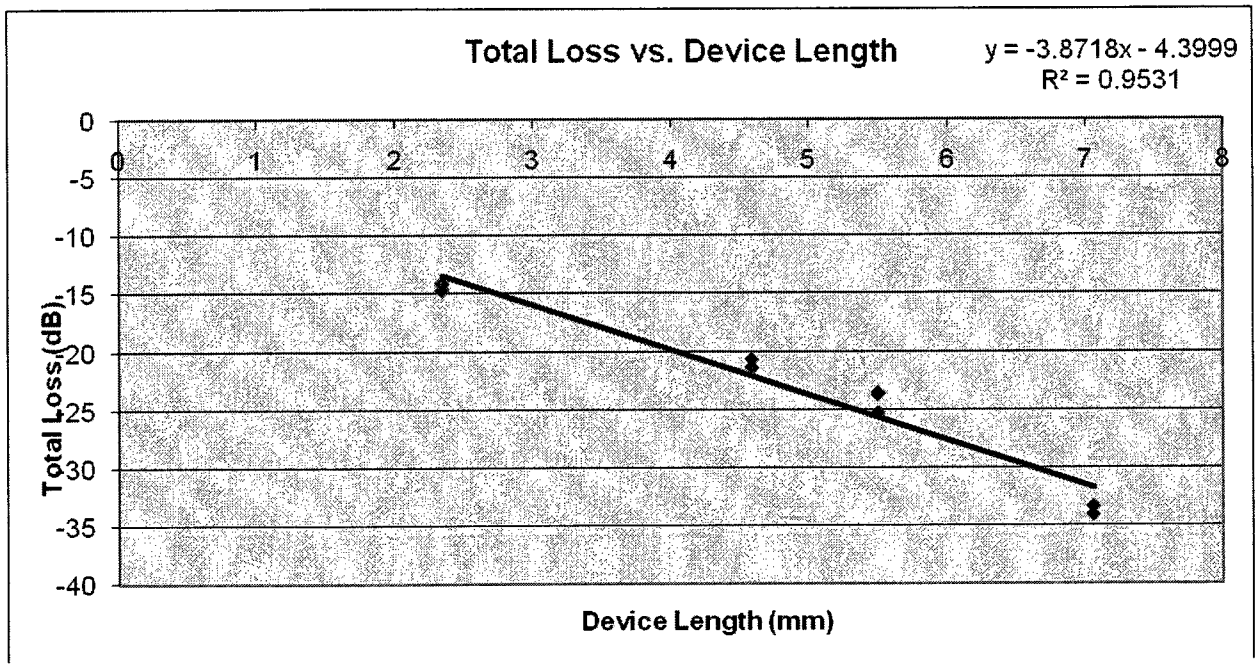

Figure A-2: Total loss versus device length of 8 μm wide and 18 nm thick Au stripe cladded by SiO_2.

waveguide were repeated multiple times in order to take into account any error due to uncertainty in the experimental setup. The total loss versus device length data is then plotted in Figure A-2 and shown with a fitted straight line. The slope of the fitted curve gives the

mode's attenuation loss, and the extrapolation of the curve to a length of 0 mm gives the total coupling loss. The R^2 correlation coefficient of 0.95 gives a good indication of the linearity of the data and therefore of the quality and consistency of the experimental measurements. A measured LRSPP mode attenuation loss of 3.8718 dB/mm at a wavelength of 1310 nm is comparable to the 2.35 dB/mm at 1525 nm reported by Charbonneau et al. [1]. The higher degree of mode confinement and the higher imaginary permittivity of Au result in a higher expected attenuation loss at this wavelength. The coupling loss of 4.40 dB is rather large, but it should be noted that the several days after the measurements were taken, it was found that the wrong technique was being used to align the polarization of the PM fiber; in fact the fiber was being polarized at an angle of emitting half TE and half TM power. Therefore, since the TE power does not couple into the SPP mode, a 3 dB reduction of all the total loss measurements is applicable since only half of the power coupled to the waveguide was TM polarized. The attenuation loss measurement remains unaffected since the slope of the line doesn't change, but the coupling loss becomes 1.4 dB, which is well within the expected value range considering Charbonneau et al. reported 0.4 dB at 1525 nm. The shorter wavelength of 1310 nm results in an increase of SPP mode confinement and thus a higher expected coupling loss. In addition, index-matching fluid was not used between the input fiber and the LRSPP waveguide, which accounts for additional loss from reflections of the input light at the air/waveguide interface.

In summary, these measurements helped to better understand the SPP and its behavior in a waveguide. It was found that extreme care must be taken to achieve good coupling conditions, with the coupling loss being very sensitive to the alignment of the fiber along its thickness. The angular alignment between the fiber and waveguide is also very important in

order for the phase of the input beam to be well matched to that of the SPP mode. An understanding of possible challenges of coupling into SPP mode of the asymmetrically cladded metal stripe was gained.

Reference

[1] R. Charbonneau, C. Scales, I. Breukelaar, S. Fafard, N. Lahoud, G. Mattiussi, and P. Berini, "Passive Integrated Optics Elements Based on Long-Range Surface Plasmon Polaritons," *Jour. Lightwave Tech.*, vol. 24, pp. 477-494, 2006.

Appendix B

Fabricated Designs of Asymmetrically Cladded SPP Schottky Detectors

The section provides a description of the fabricated Schottky photodetectors designs. The list of devices is summarize in Table B-1, where each wafer in terms of metal stripe and thickness. A single wafer contains many different widths between 1 and 7 μm, with steps of 0.5 μm between each. This list provides a summary of all fabricated devices and is planned for use for further experimental measurements.

Wafer Name	Substrate	Metal
Al-26-n	nSi *	100 nm Al
Al-27-n	nSi *	100 nm Au
Al-4-p	pSi **	100 nm Au
Al-5-p	pSi **	100 nm Al
Al-22-p	pSi **	100 nm Pt / 3.5 nm Cr / 1.5 nm SiO2
Al-17-n	nSi ***	100 nm Au
Al-14-n	nSi ***	80 nm Pt
Al-9-p	pSi **	71.7 nm Pt
Al-2	pSi **	100 nm Au
Al-3	pSi **	100 nm Au
Al-6	pSi **	100 nm Al
Al-15	nSi ***	80 nm Pt
Al-20-p	pSi **	100 nm Al
Al-13-n	nSi ***	80 nm Pt
Al-23-p	pSi **	100 nm Pt / 3.5 nm Cr / 1.5 nm SiO2
Al-30-p	pSi **	10 nm Au
Al-20-n	nSi ***	100 nm Al
Al-31-p	pSi **	32 nm Au
Al-21-n	nSi ***	100 nm Au
Al-10-p	pSi **	71.7 nm Pt
Al-8-p	pSi **	100 nm Au

Table B-1: List of Schottky detector devices fabricated in clean room environment on silicon wafers.